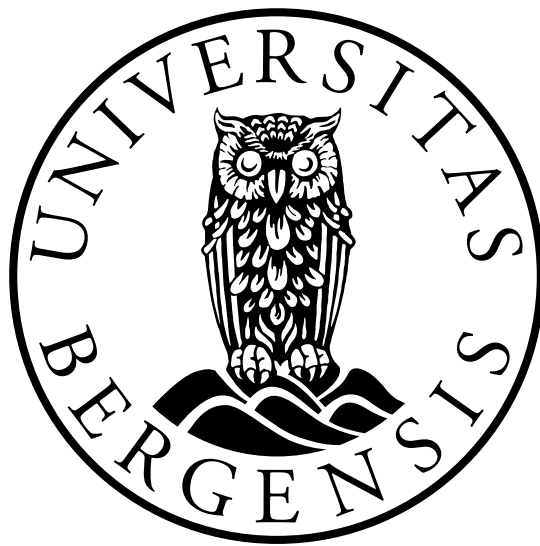# Investigating Wave Energy Potential of a Spherical Object using Numerical and Experimental Methods

Erling Calvert Dolve

Master's thesis in Ocean Technology

University of Bergen

Department of Physics and Technology

November 2023

Acknowledgements

While this thesis is the results of my multiple years of studies, it would not be possible without the support of several people.

First of all, I want to thank my supervisors Associate Professor Saeed Bikass, Associate Professor Mariusz Domagala, Associate Professor Hassan Momeni and Professor Bjørn Tore Hjertaker. Without your guidance, suggestions, inputs and help, I would have been lost on numerous occasions. Your enthusiasm and knowledge have inspired me.

I want to thank the laboratory engineers at MarinLab for guiding me through the experimental part of the thesis. An extra thanks to Engineer Torstein Frantzen and Associate Professor Gloria Maria Stenfelt, who helped me with mounting solutions, controlling the equipment and for giving input on tweaks to improve the accuracy of the measurements. Thank you to Engineer Harald Moen as well for helping me manufacture parts from my drawings. Also, a big thanks is in order for the rest of the engineering department connected to MarinLab.

Lastly I would like to thank my fellow students from the University of Bergen, my friends and family and to my partner Carina. Thank you for sharing your knowledge, good times and tough times. I would not have changed anything about our time as students together.

Abstract

Write your text here...

Contents

1 Introduction

The world is undergoing massive changes due to climate change. With an ever increasing amount of CO2 being released into the atmosphere, the changes are rapidly accelerating. One of the biggest contributors to climate change is the energy sector, emitting more than 36 Gt of CO2 in 2021 [1]. The worlds population is growing, leading to an increased demand for energy. To decrease the amount of carbon dioxide in the atmosphere, while increasing the energy production, sustainable new technologies are needed. Today, the three major sources of renewable energy are hydro power, solar energy and wind energy. Hydro power is the biggest contributor, but the growth rate is the lowest compared to other energy sources. Solar energy on the other hand, is rapidly expanding as the technology is developing and the energy conversion efficiency is rising. Wind energy is also increasing, with more installations and better turbines contributing [2].

Wave energy is another source of renewable energy, though it is nowhere as commercialized at the aforementioned. Wave energy could be a massive, mostly untapped resource with an estimated global potential of 2 TW [3]. Nearer to shore, the potential is estimated to be closer to 1,3 TW globally, which is equivalent to a technically exploitable resource of 100-800 TWh/year [4].

Using waves to harness renewable energy has its advantages over other sources of renewable energy. Sea waves offer the highest energy density among renewable energy sources [5]. Also, according to Thorpe, wave power is less environmentally degrading than other forms of energy sources, especially in relation to emissions. Wave energy converters produce no solid or fluid emissions, so during operations, wave energy converters (WECs) are non-polluting. On the other hand, Thorpe points out that the limited experience with WECs can only give incomplete pictures of the environmental effects, and some effect might be location specific [6]. A third benefit to harvesting wave energy is that unlike wind- and solar power installations, who are only capable of producing 20-30% of the time, wave energy could produce up to 90% of the time [7], as solar power is dependent on a clear sky, and wind power is dependent on wind. Sea waves on the other hand, is ever present, and therefore, wind power could contribute to more reliability in power supply.

As stated, the field of wave energy is under development. Whereas harvesting energy from ocean waves was previously thought to be unrealistic, several prototypes and some

installations are currently available.

While ocean waves carry more potential energy, the rough conditions of the open seas shorten the lifespan of the installations, and makes commissioning and maintenance difficult and expensive. To make wave energy technology economically attractive, smaller and more resilient converters should be introduced and tested, as was done during early development of commercial wind energy technology. Seas with lower energy, i.e. the Mediterranean are ideal for this purpose. Advantages to installing converters in the nearshore include protection of ports and coastlines and mitigation of erosion. Disadvantages include negative effects to the aquatic ecosystems from vibrations and low-frequency long-duration noise, but further research is required on this topic. Despite these potential issues, wave energy can increase renewable energy production, create jobs and advance existing technology [8].

The efficiency of such generators needs to be on a sufficient level if harvesting energy from ocean waves is to be viable. Therefore, this thesis will investigate the percentage of available energy in regular waves that can be absorbed from a spherical object. This will be done using both CFD simulations in ANSYS fluent, and with experimental model testing at MarinLab, the marine testing facility at HVL (Western Norway University of Applied Sciences). The parameters to be investigated are the available energy in the waves, the wave loads onto the object, the corresponding energy this load represents and the percentage of the available energy absorbed by the object. The thesis aims to contribute to building on current research on optimization of wave energy converters, and to be used as fundamental research for more advanced investigations onto the topic, including generator technology, prototype development, and ultimately to contribute towards renewable energy production from a stable source, which could add stability to the future renewable energy mix.

2 Theoretical background

This section will cover the theoretical background on computational fluid dynamics, including turbulence models, the volume of fluid method and mesh investigation parameters. Further, the relevant hydrodynamic parameters used in this theses are derived and presented.

2.1 Computational Fluid Dynamics

Computational Fluid Dynamics (CFD) is a fluid dynamics simulation tool used in engineering which allows, among others, for simulating interactions between fluids and objects. It is a powerful tool if used correctly, and allows for predicting parameters like forces, velocity and pressure, among others, between fluids and the object. This can be used for design optimization, without having to make new experimental models for each refinement. However, as simulations are built on theoretical formulas, like the Navier-Stokes equations, and physical principles, who have their restrictions, further verification using e.g. model testing is required. In this thesis, both 2D and 3D simulations will be used.

While 2D simulations are less time and computational power consuming, they have some limitations. There are some events that cannot be fully represented in a 2 dimensional space, and hence, the results are not as reliable and accurate as those from a corresponding 3D simulation.

3D simulations on the other hand is more sophisticated and can give good predictions. This requires more computational power and time, but takes into account 3D effects for all degrees of freedom.

2.1.1 Navier-Stokes equations

The Navier-Stokes equations are a set of partial differential equations, which are an application of Newtons second law of motion for fluid flows. For incompressible fluids, the equations can be written as described in Equations 1 - 3.

$$\rho g_x - \frac{\delta p}{\delta x} + \mu\Big(\frac{\delta^2 u}{\delta x^2} + \frac{\delta^2 u}{\delta y^2} + \frac{\delta^2 u}{\delta z^2}\Big) = \rho\Big(\frac{\delta u}{\delta t} + u\frac{\delta u}{\delta x} + v\frac{\delta u}{\delta y} + w\frac{\delta u}{\delta z}\Big) \tag{1}$$

$$\rho g_y - \frac{\delta p}{\delta y} + \mu\Big(\frac{\delta^2 v}{\delta x^2} + \frac{\delta^2 v}{\delta y^2} + \frac{\delta^2 v}{\delta z^2}\Big) = \rho\Big(\frac{\delta v}{\delta t} + u\frac{\delta v}{\delta x} + v\frac{\delta v}{\delta y} + w\frac{\delta v}{\delta z}\Big) \tag{2}$$

$$\rho g_z - \frac{\delta p}{\delta z} + \mu\left(\frac{\delta^2 w}{\delta x^2} + \frac{\delta^2 w}{\delta y^2} + \frac{\delta^2 w}{\delta z^2}\right) = \rho\left(\frac{\delta w}{\delta t} + u\frac{\delta w}{\delta x} + v\frac{\delta w}{\delta y} + w\frac{\delta w}{\delta z}\right) \tag{3}$$

Here, u, v and w are the velocity components in cartesian x- y- and z-directions respectively. ρ is the density of the fluid, μ is the viscosity of the fluid, p is the pressure and g is the acceleration due to gravity. These equations are the basis for CFD calculations. The CFD software applies the equations for the input values. Therefore, the limitations of these equations are the limitations for CFD.

2.1.2 Turbulence models

k-ϵ

The k-ϵ model is one of the most widely known and used two-equation turbulence models. Like the k-ω model, it uses two extra transport equations to represent the turbulent properties of the flow . Here the k-equation is the turbulent kinetic energy, while ϵ is the turbulent dissipation, which describes the scale of the turbulence [9].

The k-ϵ model has been shown to be useful for free-shear layer flows with small pressure gradients (i.e in a open, wide fluid domain). For wall bounded flows, the model gives a good agreement with experimental results for zero or low mean pressure gradient, but is less accurate for large pressure gradients. The models predictions does not take into account free-stream values of the turbulence. The model also require fine grid spacing/meshing near solid walls [9].

Wilcox' k-ω

Wilcox' k-ω turbulence model is a commonly used two equation model. This means that the model includes two extra transport equations to represent the turbulent properties of the flow. This allows the model to account for history effects like convection and diffusion of turbulent energy.

The first variable is the amount of turbulent kinetic energy, denoted with a k, and the second variable ω is the specific dissipation, the variable that determines the scale of the turbulence.

The k-ω model of Wilcox has proven to be superior to the k-ϵ model in viscous near-wall sublayers. In free-shear layer and adverse-pressure-gradient boundary layer flows, the result of the k-ω are sensitive to small free-stream values of ω [9].

SST k-ω

The SST K-ω is a turbulence model which is widely used. The Shear Stress Transport (SST) model combines the use of the k-ω model, which excels in boundary layers close to the wall boundary conditions, with the k-ϵ models properties in free stream flows, where the k-ω model is known for being too sensitive to the inlet free stream turbulence properties. The drawback of the SST k-ω model is that it produces too large turbulence levels in regions with large normal strain. These regions include stagnation regions (i.e if the diameter of a pipe section decreases), and regions with strong acceleration. However, in this thesis, the spherical object will be placed in a wide fluid domain, and hence, should not be affected by the aforementioned problems with the turbulence model [10].

2.1.3   Volume of fluid method

Marker-and-Cell method

The Makrer-And-Cell (MAC) method was the first computational method to handle incompressible, viscous fluids which moves non-lineary, developed by Harlow and Welch in 1966. In the MAC method, the fluid flow may have a free surface on which waves can form and break, or be fully enclosed within walls. When using the MAC method, the motion of the fluid is calculated by the complete Navier-Stokes equations, with all non-linear terms, with pressure and velocity as the dependent variables [11]. The drawbacks with this method in the modern era includes discrete changes in grid element properties, when a particle moves between grid elements.

Volume of Fluid Method

The Volume of Fluid (VOF) method is method of discretization, based on the Marker-and-Cell (MAC) method. The VOF method considers the amount of fluid that passes the boundaries between cells during a time step δt. Globally, the total volum fluxuating is therefore expressed by equation 4.

$$\frac{\delta F}{\delta t} + \vec{u} \cdot \nabla F = 0 \tag{4}$$

Here, F is the fluid volume fraction, u is the velocity and t is time. To prevent instabilities or inaccuracies, the VOF method uses an approximation of the free surface, rather than using an exact fluid level [12]. The VOF method is widely used for cases with a two-phase fluid flow, as the case is in this thesis.

2.1.4   Mesh

In CFD, a fluid domain is discretized into a grid of smaller elements, which merge into a mesh. Within this mesh, the behavior of the fluid is simulated. It is imperative that the mesh resolution is sufficiently fine such that the properties of the fluid particles changes gradually throughout the domain, while keeping the resolution as coarse as possible to cut down on computational time.

Whereas the resolution is an important factor to the quality of the mesh, other factors have their influence as well. Some of the most important ones are skewness, the aspect ratio and the orthogonal quality of the mesh [13]. Furthermore, the shape of the elements and the connection between these control volumes are very important. A quadrilateral (in 2D) or a hexahedral (in 3D) mesh gives a better structure, which in turn makes the calculation increments defined by the control volumes even and smoother. Examples of different element types are presented in Figure 1.
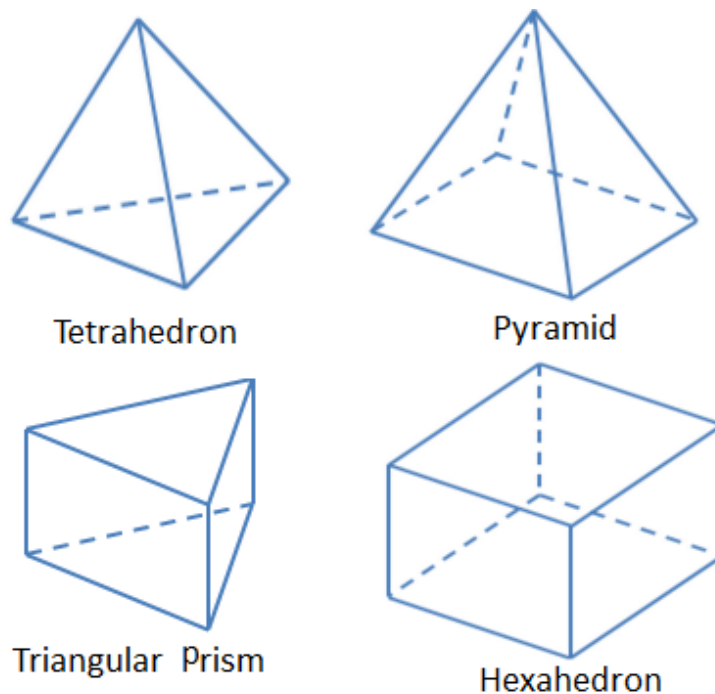

Figure 1: Examples of element types ([14])

However, for complex geometries, it can be difficult to create a regular and structured mesh. For example, if one has a circular geometry connected to a quadratic profile, it is hard to keep a hexahedral mesh, especially close to the connection between the two profiles. To combat this, one have two options. Either create a poor and unstructured mesh, consisting of a

6

grid of triangular elements, or make a hybrid mesh. A hybrid mesh is when the regularity of the mesh is kept as well as possible, while allowing some triangular elements with lower structure or some hexahedral elements with higher skewness in transitional areas to connect the geometries in question. A further study into skewness, aspect ratio, orthogonal quality, smoothness and the y+ value, including limits, are described below[13].

Skewness

Skewness is a measure used to quantify how much a cell deviates from orthogonality with respect to to its faces. It is defined as the difference between the shape of the cell and the shape of an equilateral (i.e all sides are of the same length) cell of an equivalent volume. Highly skewed cells could decrease the accuracy and stability of the solution. In general, the maximum skewness of the mesh should be below 0.95, with an average value below 0.33 [13].

Aspect ratio

The aspect ratio is a measure of the stretching of a cell. It is defined as the ratio of the maximum value to the minimum value of either the distance between the centre of the cell and the centre of the face and the distance between the cell centre and the nodes. The aspect ratio should be kept as low as possible, and not above 35:1 [13].
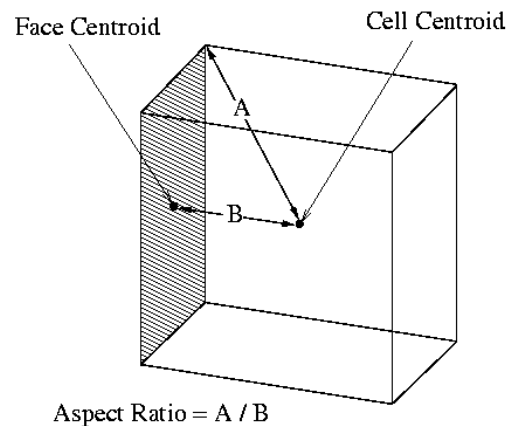

Figure 2: Aspect ratio ([13])

Orthogonal quality

The orthogonal quality is computed by creating a vector from the centroid of the cell to each of the faces, from the centroid of the cell to the centroid of the adjacent cells, and the face area vector. TYhe orthogonal quality is a parameter between 0 and 1, where 0 indicates low quality cells and 1 indicates high quality cells [13].

Smoothness

For the smoothness of the mesh is to be good, the change in the fluid parameters, like the velocity, the direction vector, the density among others, should change gradually between the control volumes. If the gradient between adjacent cells is too high, computational errors can occur. To avoid this, the control volumes should not change rapidly [13].

y+

The y+ value is a dimensionless distance from the wall of the first mesh node, and determines whether the influences in the wall adjacent cells are laminar or turbulent. This is used to describe whether the mesh is fine or coarse. y+ values are divided into 3 subcategories; viscous sublayer with y+ < 5, where the velocity profile is assumed to be laminar and dominate the wall shear, $5 <$ y+ < 30, where the velocity profile is assumed to dominate both viscous and turbulent shear, and $30 <$ y+ < 300, where turbulent shear dominates. For wall functions, a y+ value of ≈ 30 is desirable, whereas a y+ value of ≈ 1 is the best for near wall modeling [15].

2.1.5   Implicit and Explicit methods

The implicit and explicit method are numerical analysis methods used to solve the aforementioned differential equations. The explicit method calculates the system status at a future time step, while the implicit method takes the current time step as well as the future time step. As the explicit method does not take into account the current time step, the solution is less stable. This means that unless the time steps are significantly small, explicit solutions are at risk of diverging. These differences are explained mathematically in Equation 5 for the explicit method and Equation 6 for the implicit method.

$$y_{n+1} = y_n + hF(y_n, t_n) \tag{5}$$

$$y_{n+1} = y_n + hF(y_{n+1}, t_{n+1}) \tag{6}$$

These equations shows that the implicit method has the n+1 terms of the right side of the equation, as well as the y_n. This creates a smoother transition between time steps, which is more stable and opens up for larger time step sizes. On the other hand, this is a more complex solution method, which requires more computational power [16].

2.1.6   Transient and steady state problems

In Fluent, a flow can be described as steady-state or transient. A steady-state flow is considered a flow where the input parameters does not change with time. A transient flow on the other hand, allows for a varying input. As the problem proposed in this thesis has a change in mass flow and direction vector as the incoming waves develop, the problem is considered transient.

2.1.7   Pressure-velocity coupling algorithms

Fluent offers five algorithms to solve the coupling between velocity and pressure. The three used during the model preparation are listed in this subsection.

Semi-Implicit Method for Pressure-Linked Equations (SIMPLE)

The SIMPLE method is the default solver scheme in fluent. This algorithm is considered robust, fast and rarely creates divergence in the fluid domain [13].

Pressure-Implicit with Splitting of Operators (PISO

The Pressure-Implicit with Splitting of Operators method, commonly known as the PISO method is a solver method which is useful for unsteady flow problems or for domains with higher than average skewness. The PISO algorithm is based on a higher degree of the approximation of the relation between pressure and velocity. The PISO algorithm applies corrections between neighboring cells to offer a smoother and more accurate solution. At the same time, this connection between cells makes the algorithm vulnerable to large changes in the domain, and hence, it is dependent on smaller changes between time steps, i.e. on small time step sizes to avoid divergence [13].

Coupled

The coupled algorithm gives a robust and efficient solution for steady-state problems. For transient cases, the robustness of the coupled method gives faster convergence and does not easily diverge if the mesh is poor of the time steps are larger [13].

2.2 Hydrodynamics

2.2.1 Water level calculation

To calculate certain wave parameters, hydrodynamic properties must be taken into equation. First, the water depth is defined in Equations 7 - 9, for shallow, intermediate and deep water respectively.

$$d/\lambda \leq 0,05 \Rightarrow Shallow \tag{7}$$

$$0,05 < d/\lambda < 0,5 \Rightarrow Intermediate \tag{8}$$

$$d/\lambda \geq 0,5 \Rightarrow Deep \tag{9}$$

Here, d is the water depth and λ is the wave length.

2.2.2 Calculating the wave length

Calculating the wave length depends on whether the waves are in shallow, intermediate or deep water. For deep water the wave length can be calculated using Equation 10.

$$\lambda_d = \frac{gT^2}{2\pi} \tag{10}$$

Here, λ_d is the deep water wave length, g is the acceleration due to gravity and T is the wave period. For intermediate water depth, the approach is different. First, one calculates the deep water wave length. Then, based on this result, one iterates using Equation 11 until the wave length stabilises.

$$\lambda = \frac{gT^2}{2\pi} tanh\left(\frac{2\pi d}{\lambda}\right) \tag{11}$$

Here, λ is the wave length, g is the acceleration due to gravity, T is the wave period and d is the water depth. For shallow water, the wave length can be calculated using Equation 12.

$$\lambda_s = \sqrt{gd}T \tag{12}$$

Here, g is the acceleration due to gravity, d is the water depth and T is the wave period.

2.2.3 Calculating the wave speed

The equations used for calculating the wave speed depend on whether the waves occur in deep, intermediate or shallow waters. For deep water the wave speed can be calculated using Equation 13.

$$c_d = 1,56T \tag{13}$$

Here one only needs the wave period T. For intermediate depths, the wave speed is calculated using Equation 14.

$$c = \frac{gT}{2\pi}tanh\left(\frac{2\pi d}{\lambda}\right) \tag{14}$$

Here, g is the acceleration due to gravity, T is the wave period, d is the water depth and λ is the wave length. For shallow waters, the wave speed only depend on the acceleration due to gravity and the water depth, as shown in Equation 15.

$$c_s = \sqrt{gd} \tag{15}$$

If the wavelength is known, then the speed can be calculated using the relation given in Equation 16.

$$v = f\lambda \tag{16}$$

2.2.4 Archimedes' principle

Archimedes' principle is used to determine the buoyancy of an object. This is important to calculate such that the model can be sufficiently ballasted to ensure equilibrium in the desired position. The buoyancy is calculated using Equation 17.

$$F_b = \rho gV \tag{17}$$

2.2.5 Drag and lift forces

In hydrodynamics, lift and drag forces are calculated by using Equation 18 and Equation 19 respectively [17].

$$F_D = \frac{1}{2}\rho C_D AU^2 \tag{18}$$

$$F_L = \frac{1}{2}\rho C_L A V^2 \tag{19}$$

Here, C_D and C_L are the drag and lift coefficients, A is the area projected area normal to the velocities U and V and ρ is the density of the water.

2.2.6 Potential energy in waves

Beneath waves in deep waters, the water particles rotate in circular paths with an angular velocity ω and a radius of $\zeta_a e^{kx}$, where ζ_a is the wave amplitude [m], k is the wave number $[m^{-1}]$, and x is the position [m]. The kinetic energy of a mass particle is described in equation 20, assuming one length unit in the y-direction.

$$dE_k = \frac{1}{2}\rho dx dz V^2 \tag{20}$$

$$= \frac{1}{2}\rho dx dz \left[\left(\frac{\delta\phi}{dx}\right)^2 + \left(\frac{\delta\phi}{dz}\right)^2\right]$$

$$= \frac{1}{2}\rho\omega^2\zeta_A^2 e^{2kz} dx dz$$

The total kinetic energy over a wavelength in deep water is therefore described in equation 21.

$$E_K = \int_{-\infty}^{0} dz \int_{0}^{\lambda} \frac{1}{2}\rho\omega^2\zeta_A^2 e^{2kz} dx \tag{21}$$

$$= \frac{1}{2}\rho\omega^2\lambda\zeta_A^2\frac{1}{2k}$$

Since $\omega^2 =$ kg for deep waters, equation 21 can be rewritten into equation 22.

$$E_K = \frac{1}{4}\rho g\zeta_A^2\lambda \tag{22}$$

This relation is also valid for intermediate water depths.

The mass particle also has potential energy, as it is lifted from its initial still water position. At the surface, the fluid element dx has the potential energy described by equation 23.

$$dE_P = \rho g(dx\zeta)\frac{1}{2}\zeta \tag{23}$$

Over a wavelength, the potential energy is expressed with equation 24, based on equation 23.

12

$$E_P = \int_0^\lambda \frac{1}{2} \rho g \zeta^2 dx \tag{24}$$

$$= \frac{1}{4} \rho g \zeta_A^2 \lambda$$

This is valid for deep and intermediate water depths. The total energy per surface unit for any water depth is therefore described by Equation 25 [17].

$$E = E_K + E_P = \frac{1}{2} \rho g \zeta_A^2 \tag{25}$$

On a more general level, the wave power can be calculated using Equation 26.

$$P = F \cdot v \tag{26}$$

Here, F is the force and v is the velocity. By integrating this term over the wave period, the energy can be calculated with Equation 27.

$$E = \int_0^T P \, dt = \int_0^T F \cdot v \, dt \tag{27}$$

2.2.7   ANSYS wave definition

When defining a wave in ANSYS, it calculates the input using the governing equation shown in Equation 28

$$\zeta = \zeta_A cos(k_x x + k_y y - \omega_e t + \epsilon) \tag{28}$$

Here, ζ_A is the wave amplitude, ϵ is the phase difference, k_x and k_y are the wave numbers in their respective directions. The wave number is defined in Equation 29 and ω_e is the effective wave frequency, defined in Equation 30.

$$k = \frac{2\pi}{\lambda} \tag{29}$$

$$\omega_e = \omega + kU \tag{30}$$

Here, λ is the wave length and U is the uniform incident wave velocity. The effective frequency is a Doppler shifted wave frequency, where the observer is is travelling with the base flow U, unlike for the absolute frequency, where the observer is static in the coordinate system. Here, the absolute frequency ω is defined in Equation 31.

$$\omega = \sqrt{gk \cdot tanh(kh)} \tag{31}$$

The velocity components can then be derived for shallow/intermediate waves, by using Equation 32.

$$\begin{pmatrix} u \\ v \end{pmatrix} = \frac{gkA}{\omega} \frac{cosh[k(z+h)]}{cosh(kh)} \begin{pmatrix} cos\theta \\ sin\theta \end{pmatrix} cos(k_x x + k_y y - \omega_e t + \epsilon) \tag{32}$$

As the inlet is defined in the x-direction, only the definition of u will be used. Also, the inlet uses the maximum value of u, and therefore, the cosine link and the hyperbolic cosine fraction is assumed to be equal to 1. At the inlet boundary condition, ANSYS requires a velocity input, wave height and wave length. To get the proper wave, the effective wave frequency will have to match the desired frequency output.

3 Preparing CFD model

To prepare the model, a 2D adaption was used to keep simulation time low while testing the input parameters. While a 2D model will make test simulations go significantly faster, it is not a good adaption for numerical calculations for this case, as a sphere in a 2 dimensional space is a cylinder. Nevertheless, to check that the input parameters creates the desired output wave, to test the performance of implicit versus explicit method and the performance of the pressure-velocity coupling algorithms, this this adaption is adequate.

This section will cover the procedure of creating a suitable fluid domain for testing, discretizing the domain into a fine grid of cells, setting up the boundary conditions and solution models, before running the analysis in ANSYS Fluent.

3.1 Fluid domain

The fluid domain is defined as a rectangular domain with the dimensions shown in Table 1.

Table 1: Domain parameters for the 2D fluid domain

Length (x)	15 m
Height (z)	4.5 m
Sphere diameter	200 mm
Still water level	2.5 m

These dimensions are coherent with the wave tank at the experimental testing facility, although the domain length is reduced. This is done to reduce the computational power and time needed, while leaving enough room for the waves to build up before reaching the object, and enough room after the object for the waves to not be reflected back at the end of the domain. The sphere is placed at x = 10 m, and is defined by removing a cylindrical hole from the fluid domain. The edge of the cutout is defined as a wall with the no slip property. The fluid domain is presented in Figure 3.
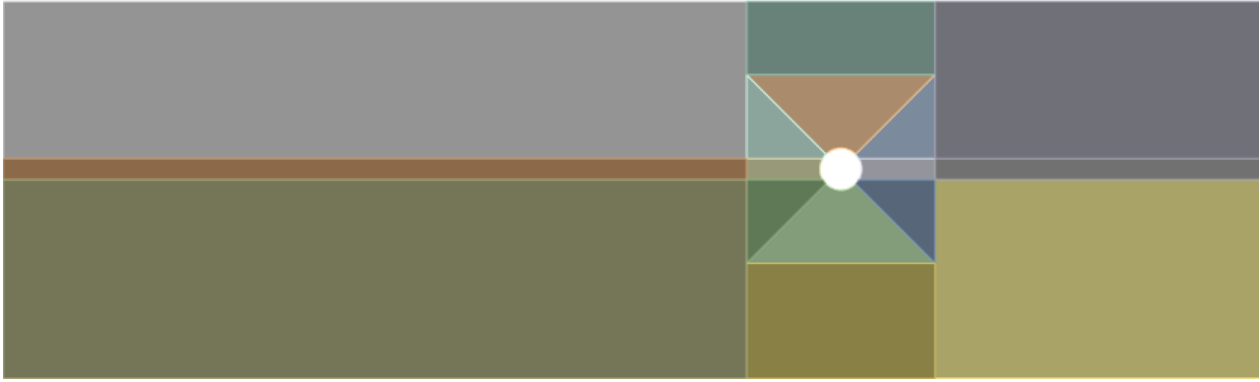
Figure 3: 2D Fluid domain

As this figure shows, the fluid domain is sliced into different sectors. These will be used to refine the mesh in the areas requiring higher accuracy.

3.2 Mesh

To create a good mesh, the mesh type is set to quadrilateral, and the domain is discretized into elements of 200 mm. This gives the mesh details given in Table 2.

Table 2: Mesh details for the 2D mesh

Element size	200 mm
Number of nodes	10557
Number of elements	10279

Edge sizing is used in the sliced sectors of the fluid domain to refine the mesh in the wave channel and close to the object. Figure 4 shows the sectors which are given this treatment.
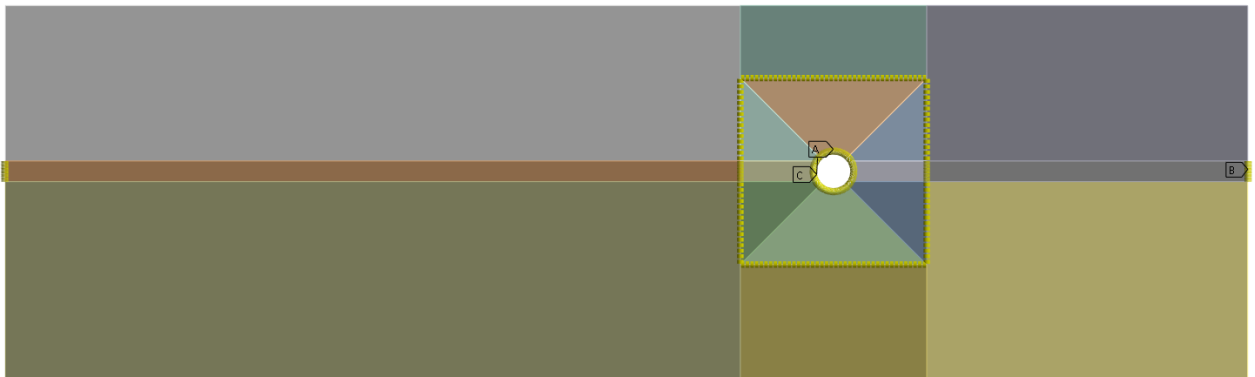
Figure 4: Edge sizing used for meshing

16

Here, edge sizing A divides the top and bottom of the sphere, as well as the horizontal slices above and below the sphere into 40 divisions. Edge sizing B divides the horizontal channel through the sphere, as well as the side walls of the sphere into 30 divisions. Edge sizing C divides the vertical slices around the sphere, except from the channel controlled by edge sizing B. Edge slicing C also controls the point where the diagonal lines meet the sphere. Edge slicing C divides these features into 15 divisions. Figure 5 shows the full fluid domain after meshing.
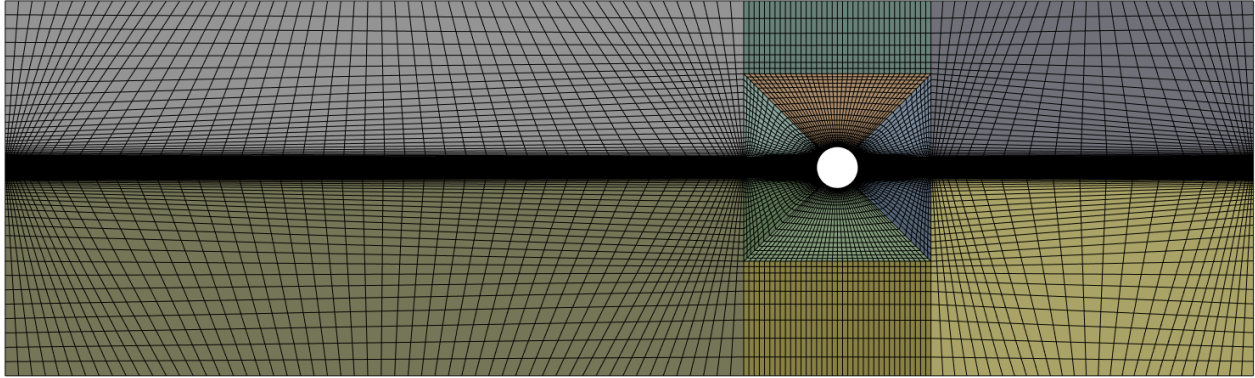
Figure 5: Mesh after the edge sizing

The mesh quality is determined by looking at the aspect ratio, skewness and orthogonal quality. These parameters are explained thoroughly in the theory section, and are given in ANSYS meshing. The minimum, maximum, average and standard deviation is given in Table 3

Table 3: Aspect ratio data for the 2D mesh

Aspect ratio	
Min	1.0009
Max	59.388
Average	15.32
Standard deviation	23.329

As stated in the theory section, the aspect ratio should be below 35. Here, the average is below said value, but the maximum is above. Figure 6 shows where the cells with the maximum aspect ratio are located.

17

Figure 6: High aspect ratio cells for the 2D mesh

As the figure shows, the cells with a exceeding aspect ratio is located in the wave channel, which is not ideal, but the aspect ratio goes down below the maximum recommended value around the point of contact. Thus, it is accepted.

The average skewness of the cells is recommended to be below 0.33, with a recommended maximum below 0.95. The skewness of the 2D mesh is given in Table 4.

Table 4: Skewness data for the 2D mesh

Skewness	
Min	$1.3057 \cdot 10^{-10}$
Max	0.5
Average	0.10872
Standard deviation	0.12045

Here, the average skewness is well below the recommended 0.33, and the maximum is not close to the recommended maximum of 0.95.

The orthogonal quality must be checked as well. As the name suggests, an orthogonal quality of 1 means that the side of the cells are orthogonal with respect to each other. The desired outcome is having the most cells at or close to 1. The orthogonal quality data of the 2D mesh is denoted in Table 5.

Table 5: Orthogonal quality data for the 2D mesh

Orthogonal quality	
Minimum	0.71521
Maximum	1
Average	0.96884
Standard deviation	$5.3711 \cdot 10^{-2}$

As the table shows, the average orthogonal quality is high, over 96 %, with a minimum of 0.72. It is expected that some cells have a lower orthogonal quality due to the mesh definitions. As Figure 5 shows, there are diagonal cells before and after the sphere's location, which will naturally be of a lower orthogonal quality, but as they are located away from the waves and point of contact with the object, it is not considered a problem.

3.3 Solver setup

The domain consist of a primary phase of air and a secondary phase of water, with a density set to 1.225 kg/m^3 and 997 kg/m^3 respectively. At the inlet, the open channel wave boundary condition is activated, and the wave pattern is created using the shallow/intermediate wave setting, solved using third order stokes wave theory, which is applicable for the wave parameters. In the multiphase tab, the wave height and wavelength is input. The wave height is defined for each test, and the relating wavelength is calculated using the iterative dispersion relation. This process is described in section 2.2.7.

The outlet boundary condition momentum is kept at the default settings (backflow turbulent intensity [%] = 5 and backflow turbulent viscocity ratio = 10). In the multiphase tab, the open channel option is activated, the free surface level is set to 2,5 m, i.e the still water level, and the bottom level is set to 0 m. The density interpolation method is kept as "from neighboring cell".

The bottom and the sphere boundary conditions are given the stationary wall and no slip wall properties. The top is given the stationary wall property as well, but instead of being set to no slip wall, the specified shear option is chosen instead. Here, the shear stress components in both x and y direction is set to 0 Pa, to prevent viscous effects and turbulence from forming along the top. The top is defined as a free slip wall instead of an open channel due to problems encountered with the pressure in the fluid domain when defining the top as an open channel.

The solution is initialized using hybrid initialization method, with the open channel initialization computed from the inlet, with a flat open channel initialization method.

For testing and preparation, the simulation is run for a varying amount of time steps, with a time step size of 0.01 to 0.05 s with a maximum of 10-20 iterations per time step, depending on the test.

4 3D simulations

While the 2D adaptation is only adequate for testing input parameters, a 3D model could accurately calculate the parameters needed for further analysis.

This section will cover the process of creating a suitable 3-dimensional fluid domain, discretizing the domain into a fine grid and analyzing the mesh, before setting up the boundary conditions and solution models. Then, the simulation will be performed in ANSYS Fluent.

4.1 Fluid domain

As a result of the model preparation tests, three different fluid domains are created to optimize the calculations. These are created to place the sphere at the position x = $\lambda/2$, to ensure enough room for a damping zone of 2λ after the sphere to avoid reflecting waves, and to have a margin between the sphere and the damping zone. To account for these parameters, the fluid domains are given a length of 3λ. As there are nine waves in total, with three different frequencies and three different wave heights, a fluid domain is created for each of the frequencies. The dispersion relation used to calculate the wavelength is only dependent on the frequency or period, and not on the height of the wave. The wavelengths and corresponding fluid domain lengths are presented in Table 6.

Table 6: Wavelengths and fluid domain lengths from their respective frequencies

Frequency [Hz]	Wavelength [m]	Fluid domain length [m]
0.3	14.0	42
0.4	9.2	27.6
0.5	6.2	18.6

Each fluid domain are sliced around the sphere and the channel for incoming waves to create zones where the mesh can be refined. The domains are also sliced in half along the x-z plane, and the sliced surface is given the symmetry attribute. The y and z dimensions are equal for all of the domains, and are defined so that the computational power required is low, while keeping them big enough to avoid wall effects interfering with the sphere. The still water level and the sphere diameter, which is the same that will be used for experimental tests are the same for each domain. These dimensions are shown in Table 7.

Table 7: Fluid domain parameters for the first 3D fluid domain

Length (x)	10 m
Width (y)	3 m
Height (z)	4.5 m
Sphere diameter	200 mm
Still water level	2.5 m
Sphere position from inlet for f = 0.3 Hz	7 m
Sphere position from inlet for f = 0.4 Hz	4.6 m
Sphere position from inlet for f = 0.5 Hz	3.1 m

For a spherical object, The biggest difference between the 2D and 3D-simulations are related to the shape. As discussed in the previous section, is is impossible to model a sphere in a 2 dimensional domain, and the resulting object is a cylinder, if extrapolated to 3 dimensions. Also, in a 2D fluid domain, all the incoming water is forced to go over the object. When the fluid domain is given the third dimension, the water can both go over the sphere and be deflected to the sides.

4.2   Mesh

When meshing the domain, the element size is set to 150 mm. The same edge sizing and slicing applied to the 2D domain, are used for the 3D domain to refine the mesh in the wave channel and closer to the point of impact. The mesh details are presented in Table 8.

Table 8: Mesh details for the 3D model

Mesh parameter	f = 0.3 fluid domain	f = 0.4 fluid domain	f = 0.5 fluid domain
Element size	150 mm	150 mm	150 mm
Number of nodes	980352	656390	502178
Number of elements	940965	628881	480128

The resulting mesh graphics from these details is presented in Figure 7, with a closer zoom around the sphere shown in Figure 8. As the same slicing, element sizes and refinements are used, only the mesh from the f = 0.3 Hz model is shown in these figures.

Figure 7: 3D mesh for the full domain
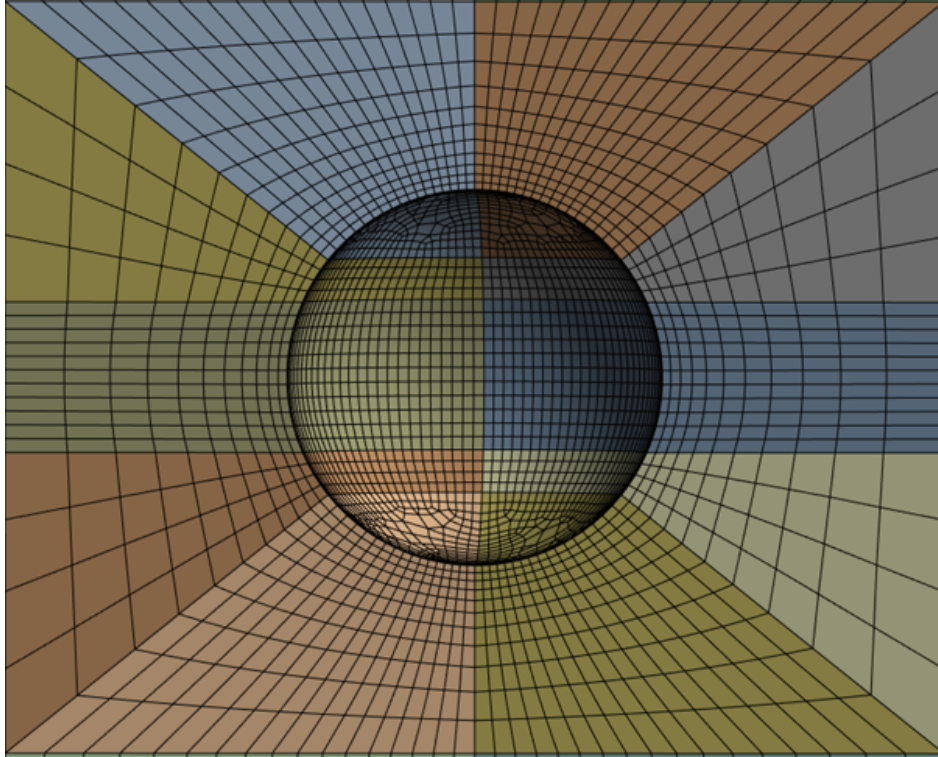
Figure 8: 3D mesh zoomed around the sphere

To analyze the quality of this mesh, the aspect ratio, skewness and orthogonal quality of the mesh is checked for each fluid domain. These parameters are described in the theory section.

4.2.1   Mesh parameters for the f = 0.3 Hz fluid domain mesh

Table 9 shows the aspect ratio for the mesh.

Table 9: Aspect ratio for the mesh

Aspect ratio	
Minimum	1.0069
Maximum	36.02
Average	8.8089
Standard deviation	5.8618

As the data shows, the average aspect ratio is well below the recommended maximum of 35, but the maximum is slightly above. The cells with the maximum aspect ratio are shown in Figure 9.
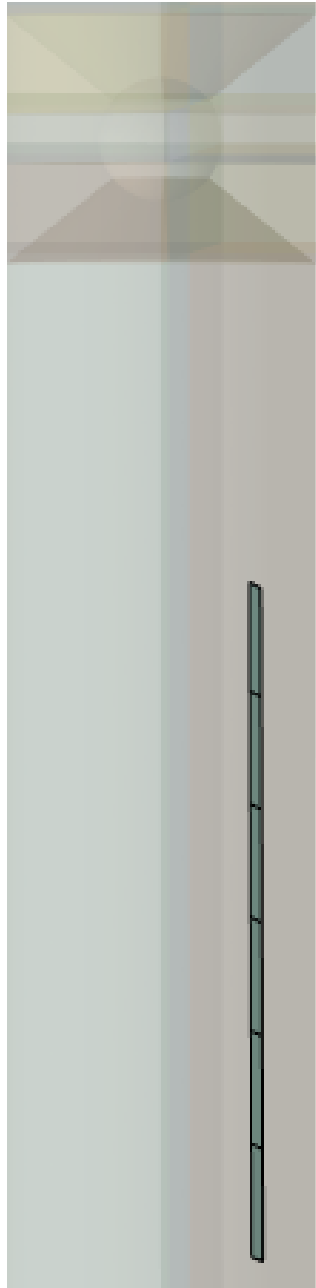
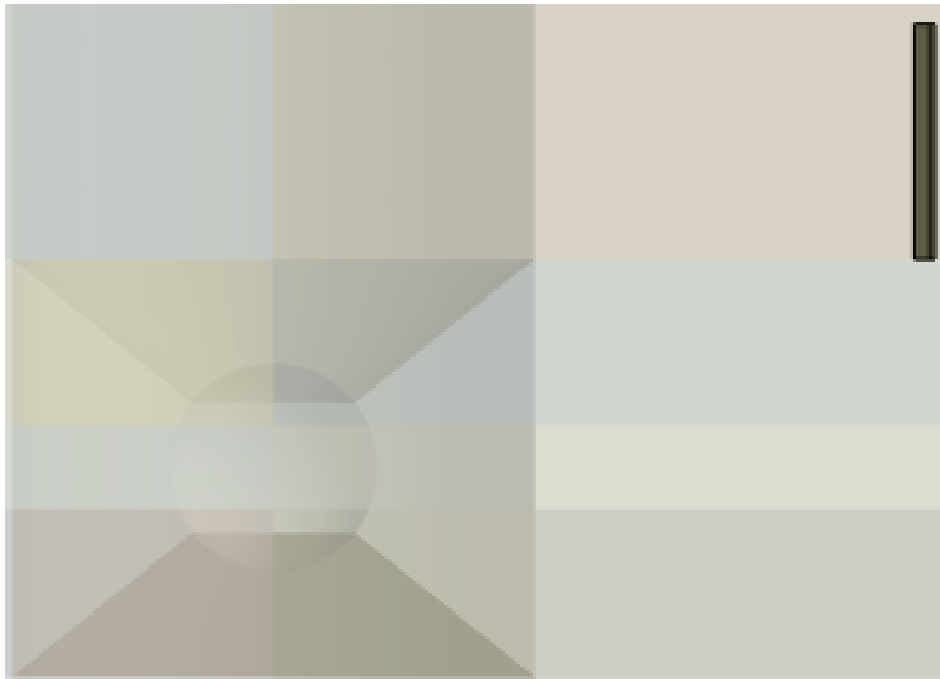

Figure 9: Cells with high aspect ratio for the mesh

As the figure shows, these cells are not located in the wave channel, and it is not close to the sphere. As the overshoot in aspect ratio was slight, and not in these more sensitive areas, it is not considered problematic.

The data showing skewness of the cells in the mesh is presented in Table 10.

Table 10: Skewness for the mesh

Skewness	
Minimum	$1.3057 \cdot 10^{-10}$
Maximum	0.90327
Average	0.14972
Standard deviation	0.20619

As the data shows, the average skewness is below the recommended maximum of 0.33, and the maximum skewness stays within the recommended maximum of 0.95.

The last parameter to be investigated is the orthogonal quality of the mesh. The data is given in Table 11.

Table 11: Orthogonal quality for the mesh

Orthogonal quality	
Minimum	0.15156
Maximum	1
Average	0.91429
Standard deviation	0.17424

As the table shows, the average orthogonal quality is almost 91 % which is good. The minimum of 0.15 is expected as the cells are going diagonally away from the sphere and wave channel, and these cells are shown to have the smallest orthogonal quality, as shown in Figure 10.

Figure 10: Minimum orthogonal quality cells

As these cells are not interfering with the sensitive areas of the domain, they are unproblematic.

4.2.2 Mesh parameters for the f = 0.4 Hz fluid domain mesh

Table 12 shows the aspect ratio for the mesh.

Table 12: Aspect ratio for the mesh

Aspect ratio	
Minimum	1.0122
Maximum	58.929
Average	8.0089
Standard deviation	5.0978

As the data shows, the average aspect ratio is well below the recommended maximum of 35, but the maximum exceeds this threshold. The cells with the maximum aspect ratio are shown in Figure 11.

Figure 11: Cells with high aspect ratio for the mesh

As the figure shows, these cells are not located in the wave channel, and it is not close to the sphere. As the cells overshooting the maximum recommended aspect ratio are few, and not in these more sensitive areas, it is not considered problematic.

The data showing skewness of the cells in the mesh is presented in Table 13.

Table 13: Skewness for the mesh

Skewness	
Minimum	$1.3057 \cdot 10^{-10}$
Maximum	0.94101
Average	0.16079
Standard deviation	0.20037

As the data shows, the average skewness is below the recommended maximum of 0.33, and the maximum skewness stays within the recommended maximum of 0.95.
The last parameter to be investigated is the orthogonal quality of the mesh. The data is given in Table 14.

Table 14: Orthogonal quality for the mesh

Orthogonal quality	
Minimum	0.15492
Maximum	1
Average	0.914
Standard deviation	0.16853

As the table shows, the average orthogonal quality is over 91 % which is good. The minimum of 0.15 is expected as the cells are going diagonally away from the sphere and wave channel, and these cells are located the same place as for the f = 0.3 Hz mesh. As these cells are not interfering with the wave channel, nor the sphere, it is not concerning.

4.2.3   Mesh parameters for the f = 0.5 Hz fluid domain mesh

Table 15 shows the aspect ratio for the mesh.

Table 15: Aspect ratio for the mesh

Aspect ratio	
Minimum	1.0223
Maximum	43.523
Average	7.9081
Standard deviation	4.9851

As the data shows, the average aspect ratio is well below the recommended maximum of 35, but the maximum exceeds this value. The cells with the maximum aspect ratio are shown in Figure 12.

Figure 12: Cells with high aspect ratio for the mesh

As the figure shows, these cells are not located in the wave channel, and it is not close to the sphere. As the cells overshooting the maximum recommended aspect ratio are few, and not in these more sensitive areas, it is not considered problematic.

The data showing the skewness of the cells in the mesh is presented in Table 16.

Table 16: Skewness for the mesh

Skewness	
Minimum	$1.3057 \cdot 10^{-10}$
Maximum	0.89491
Average	0.16515
Standard deviation	0.19179

As the data shows, the average skewness is below the recommended maximum of 0.33, and the maximum skewness is well within the recommended maximum of 0.95.

The final parameter to be investigated is the orthogonal quality of the mesh. The data is given in Table 17.

Table 17: Orthogonal quality for the mesh

Orthogonal quality	
Minimum	0.16479
Maximum	1
Average	0.91794
Standard deviation	0.15714

As the table shows, the average orthogonal quality is over 91 % which is good. The minimum of 0.15 is expected as the cells are going diagonally away from the sphere and wave channel, and unlike for the other fluid domains, these cells are only after the waves have interfered with the sphere, and not near the wave channel. Therefore, it is not considered a problem. These cells are shown in Figure 13.

Figure 13: Minimum orthogonal quality cells

4.3 Fluent setup settings

For the Fluent setup, the implicit Volume of Fluid method is used as tests using the explicit method frequently diverged, causing "floating point exception" errors, i.e. errors due to illegal operations in the governing equations, like attempting to divide by 0.

Further, as mentioned in the fluid domain section, a damping zone called a numerical beach is added to the end of the domain to dampen the waves and as such, avoid back flow from the end of the domain. As Fluent recommends, this damping zone is 2λ long, and starts from the end of the domain.

The materials in the fluid domain are defined as air with a density of 1.225 kg/m^3 as the primary phase and liquid water with a density of 998.2 kg/m^3.

For the boundary condition, in the momentum tab of the inlet, the velocity for all cardinal directions are set to zero, as this thesis does not focus on the effect of current. In the multiphase tab, the wavelengths and wave heights are entered, as well as the free surface level, more commonly known as the still water level. The rest of the parameters in these boundaries are kept at the default values. The sides and bottom of the fluid domain are given the no slip wall property, meaning that the fluids is not allowed to move freely along these boundaries. This is especially important for the bottom of the domain, as this is to serve as the seabed for the intermediate waves. The top is set as a free slip wall and not an opening, meaning that it is considered a wall, but the fluids are allowed to move freely along the boundary, with no friction. This is due to early tests showing and inexplicable pressure column going from the free surface level to the top of the domain as shown in Figure 14.
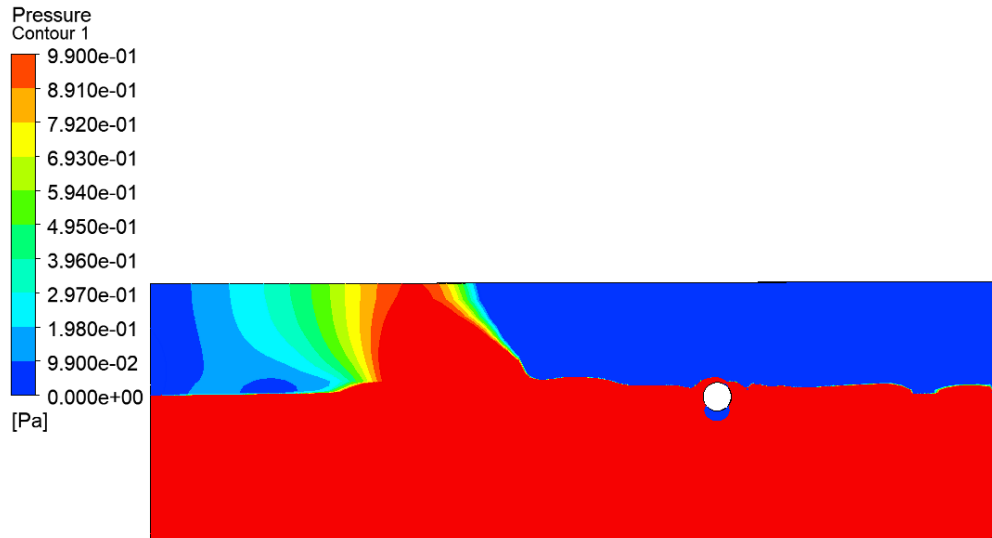
Figure 14: Contour plot showing the pressure surge

Five report files are defined for further analysis. These are the drag force data along the wave direction, lift force data in the z-direction, their respective drag and lift coefficients and

30

the water volume fraction at the sphere, i.e. the wet surface. The force reports will be used to analyse force results, while the coefficients and wet surface will be used for wave velocity analyses and subsequently for energy calculations.

The solver is set to using the PISO method described in the theory section, as early tests showed that the PISO and coupled algorithms both gave reliable force calculations, but the PISO method gave quicker simulations. The SIMPLE method was not as reliable, and for certain cases, the solution diverged.

The solution is initialized from the inlet using the flat initialization method. This means that the first state before running the waves will be still water. One could initialize using wavy initialization method to get wave data without having to wait for the waves to reach the sphere, but to avoid any possibilities of generating initial disconnected waves, the extra computational time was allocated to the flat initialization method.

The solution is set to run for a maximum of 8000 time steps of 0.01 s each, and a maximum of 20 iterations per time step. Early tests showed that the solution converged between 10 and 20 iterations, sometimes quicker, so a maximum of 20 iterations is deemed sufficient. The solution is saved every 30 time steps for f = 0.3, every 25 time steps for f = 0.4 s and every 20 time steps for f = 0.5 to ensure that the solution is sampled at least 10 times per wave.

5 Experimental method

This section will cover the experimental method. In order, the the test facility at HVL, MarinLab, the experimental setup, the equipment used, the calibration of the measurement equipment and a verification of the setup is presented in their respective sub chapters.

5.1 Experimental test facility

MarinLab is the hydrodynamic test facility located at HVL campus Bergen and was built in 2016. The facility features a 2,2 x 3 meter cross section tank with a length of 50 meters, as depicted in Figure 15.
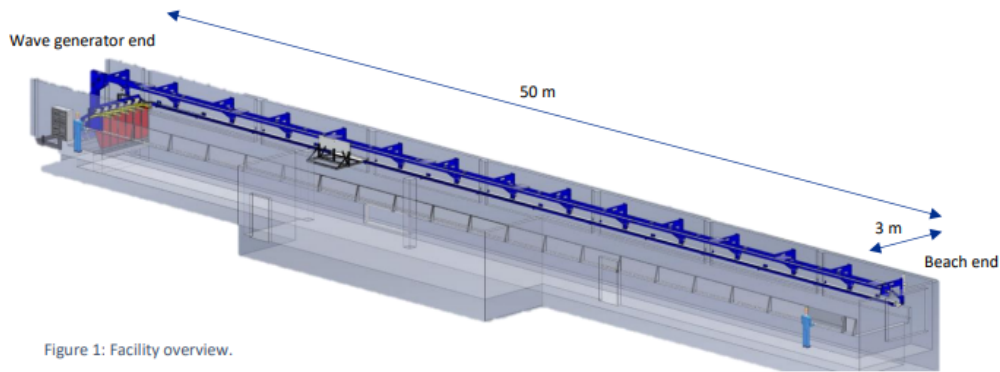
Figure 15: Overview of MarinLab ([18]).

The tank has a towing carriage from Edinburgh Designs, which has a maximum speed u_{max} = 5 m/s, and a maximum acceleration a_{max} = 1,2 m/s^2. The wave generator consist of 6 hinged wave paddles, which can generate waves with a maximum height of 0,5 m at wave periods close to 2 seconds. The paddles are force-feedback controlled which allows damping of unwanted wall reflections. The paddles can generate regular waves and irregular waves with JONSWAP, Bretschneider and Pierson-Moskowitz spectra all possible [18].

On the opposite side of the wave paddles, a passive beach is installed. This beach is made by a metal plate with holes, placed at an angle of 8° to the still water line. This allows both for a representative study of wave breaking due to depth change, and it absorbs the incoming waves to counteract reflections. In this thesis, the latter is important to prevent interference from reflecting waves.

The possible waves that can be generated by the paddles is determined by the wave breaking limit curve in Figure 16.
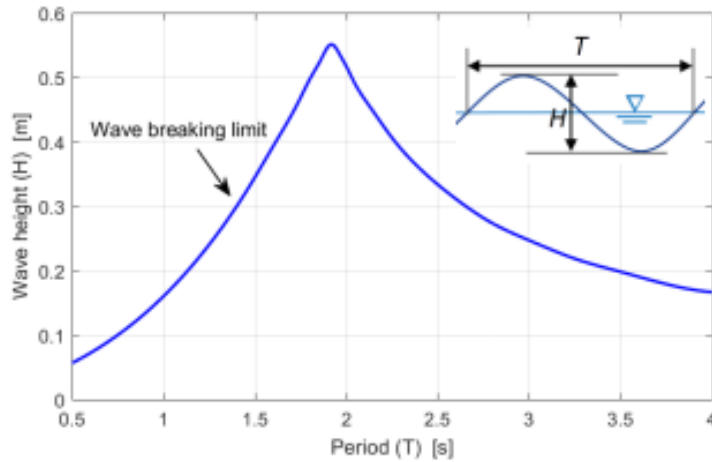
Figure 16: Wave breaking limit. ([18])

In addition, MarinLab is equipped with the following:

- Towing Carriage, $u_{max} = 5$ m/s, $a_{max} = 1{,}2$ m/s^2

- Constant-force towing line

- Qualysis motion capture system

- 8 Resistance-type wave gauges

- Load cells ranging from 5-500 N

- Nortek Acoustic-Doppler Velocimeter

- GoPro underwater cameras for video capture

5.2 Experimental setup

As stated in section 2.1, it is important to verify the numerical simulation experimentally. The test setup consist of a 40x40 mm Aluflex profile, attached to a spherical buoy. The profile is attached to the buoy using a custom made aluminum plate. The plate is drawn in the CAD software Creo Parametric, exported to a plasma burner which burns the plate from an aluminum sheet. After the aluminum shape is cut out, the edges are sanded down, and holes for M8 bolts are drilled out. The design for the plate is presented in Figure 17.
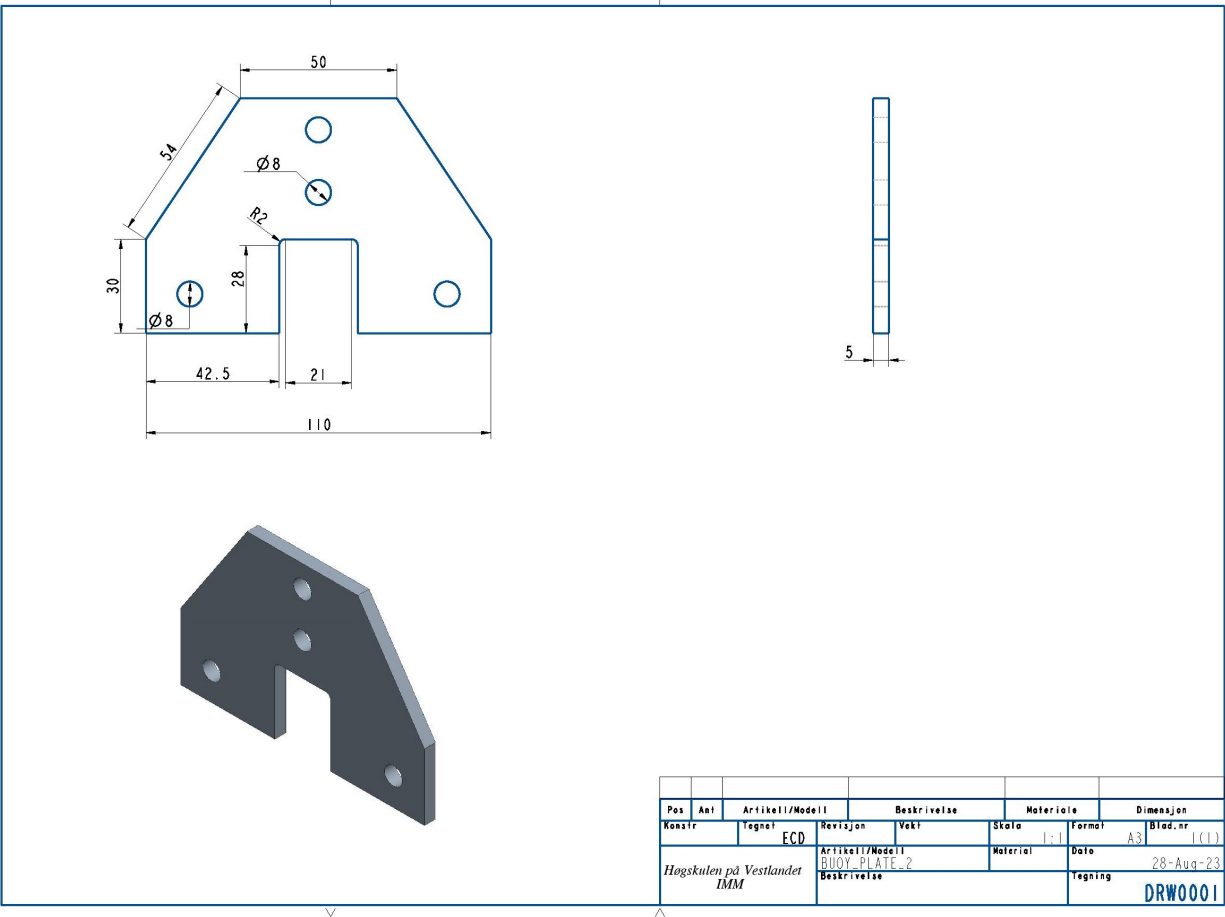
Figure 17: Custom designed plate to attach the buoy to the aluflex profile

The Aluflex profile is attached to two load cells, which are placed perpendicular to each other, to measure the loads in x- and z-directions. The load cells measure drag- and lift force, respectively.

Usually, one would ballast the test model to counteract the buoyancy of the air-filled object. In this case, there are concerns about the structural integrity of the spherical buoy, should an opening be cut out to ballast it. Therefore, a simplification is made. The sphere will be held in the correct position by the Aluflex profile, which is attached to the MarinLab carriage. This will mean that before the waves applies extra loads to the sphere, and subsequently the load cells, the load cell recording the z-direction loads will record an initial load corresponding to the buoyancy force, minus the weight of the profile itself. This will be accounted for by zeroing the load cell after mounting the experimental setup.

5.3 Equipment

For the experimental setup, a variety of equipment is used. Load cells are used to measure the loads onto the sphere, wave gauges are used to control the wave shape, DAQ units to sample the data, and various software.

Load cells are measurement devices made for measuring loads. The load cells used in this theses are S-Beam load cells and a button load cell. S-Beam load cells are named after their shape. These load cell types are made from a system of strain gauges connected to the central area in the form of a Wheatstone bridge, as shown in Figure 18 [19].
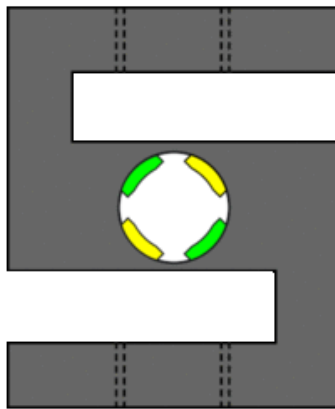
Figure 18: Figure showing an S-beam load cell ([19])

Strain gauges are sensors whose electrical resistance varies with changes in strain, which again is defined as the deformation or displacement of material as a result of applied stress, i.e the applied force to a material, divided by its cross section. By using these principles, strain gauges convert the applied force into electrical signals which can be measured. To be able to measure these small changes in electrical resistance, the strain gauge must be connected to an electrical circuit, capable of responding to the slightest of changes. Using multiple strain gauges, connected in a divided bridge circuit, these small changes can be measured in what is called a Wheatstone bridge. In a Wheatstone bridge, a voltage is applied across the circuit, and the output voltage is measured across two points in the middle of the bridge. When unloaded, the Wheatstone bridge is balanced, and no output voltage is measured. Any impact on the strain gauge will create an imbalance which will create an output voltage to be measured. As the change in voltage is small, a signal amplifier is used, which will amplify the voltage difference, but also noise. Therefore, signal filtering has to be used in tandem

35

with the amplification [20]. A drawing of a Wheatstone bridge is shown in Figure 19.
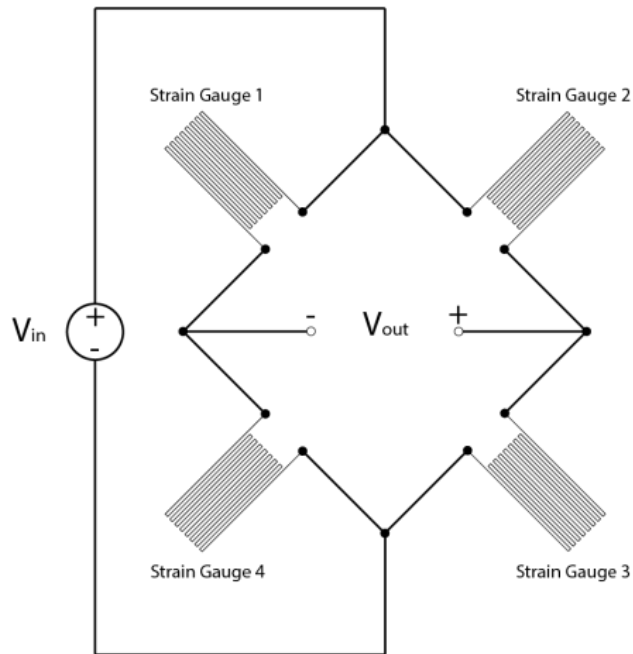
Figure 19: Wheatstone bridge ([20])

Wave gauges measure the resistance of the water between two parallel rods. The resistance is proportional to the immersion depth. Using alternating current (AC) from a low impedance current amplifier, electrolysis is avoided [21].

Different software are used for data collection, data processing, and technical designs and drawings. For data collection, LabVIEW from National Instruments is used. LabView is a systems engineering software. In the software, virtual instruments (VI's) are created to perform the data collection and presentation schemes, in the form of a block diagram. The VI reads from the selected equipment, condition the data (i.e applying filters), collect and present data. The block diagram is visualized in a front panel, as shown in Figure 20 and Figure 21.
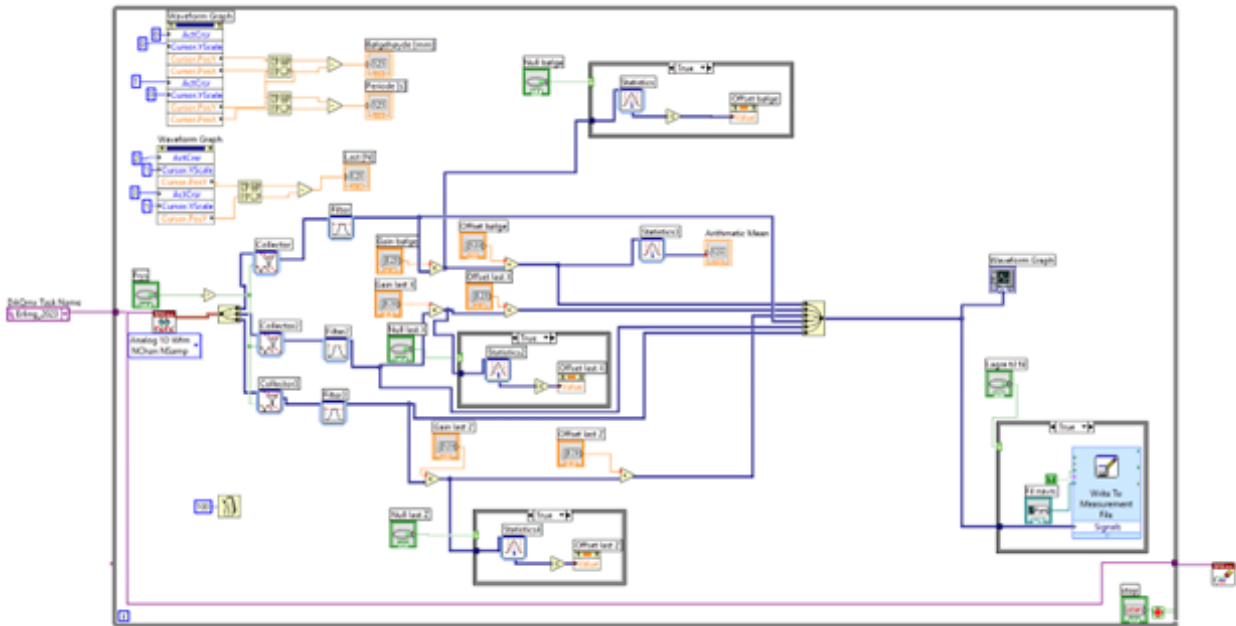
Figure 20: Block diagram to the LabVIEW VI

Figure 21: Front panel to the LabView VI

For data processing, MATLAB is used. MATLAB is a programming and numeric computing platform from MathWorks. The software is used by scientists, engineers and students for plotting and presenting data, analyze data, crate algorithms and more [22].

Creo Parametric and Creo draw was used to design and draw the plate in Figure 17. Creo is a CAD (Computer Assisted Design) software from PTC. Creo is a widely used CAD software which is easy to learn, with enough features to design complex features.

The following equipment was used for the experimental setup:

- Load cell for x-direction, Type DBBSM-003-000, max 5 kg, Serial Number 49228.

- Load cell for z-direction, Type DBBSM-003-000, max capacity 5 kg, Serial Number 49227.

- Load cell for calibrating x-direction load cell, HBM U90 max capacity 200N, Serial Number 211310690

- Custom made aluminum plate presented in Figure 17.

- Aluflex profiles with varying length and cross sections.

- Varying bolts, washers and nuts.

- DAQ unit, NI cDAQ-9174.

- Wave gauges, Edinburgh Designs WG8USB.

- Software LabVIEW from National Instruments.

- Software MATLAB from MathWorks.

- CAD software Creo Parametric and Creo Draw from PTC.

5.4   Calibration procedure

To ensure accurate and reliable measurements, the load cells need to be calibrated. According to ITTC, 10 mass increments should be used, and the full range of the load cell should be used. The load cell outputs are recorded with the applied load, and the full procedure should be done with both increasing and decreasing load increments. Lastly, the accuracy of the load cell is validated by applying miscellaneous load of a known quantity onto the load cell,

while comparing the output [23].

5.5 Calibration of x-direction load cell

When calibrating a load cell placed horizontally, the load increments have to work horizontally as well. One solution is to use a pulley system and hang mass increments vertically. The drawback to this method is that the pulley will take up some of the load due to friction. Therefore, the output from the load cell will not be completely proportional to the applied mass. This could be counteracted by installing a second calibrated and accurate load cell between the pulley and the primary load cell. Then, the applied mass can be recorded by the secondary load cell, and the output to said mass is recorded by the primary load cell. This solution also has its drawbacks, as the secondary load cell could be affected if the mass increments tugs hard on it when the masses are added. These proposed setups are illustrated in Figure 22.

(a) Without a secondary load cell   (b) With a secondary load cell
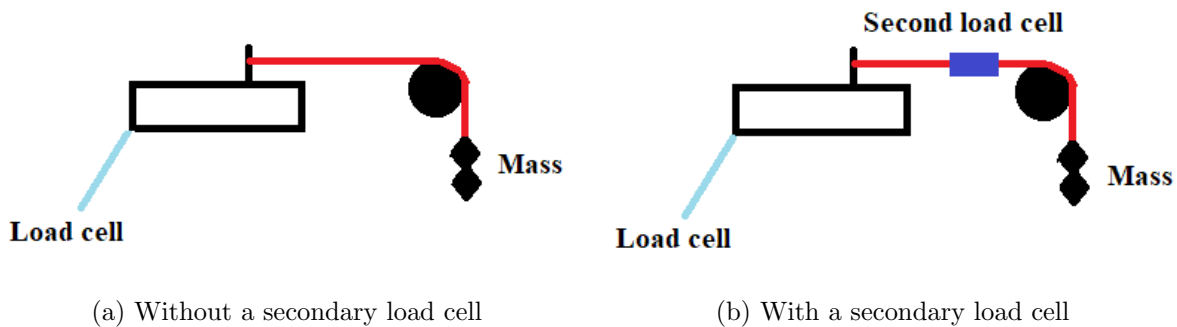
Figure 22: Illustrations of the load cell calibration setup without (a), and with (b) a secondary load cell

Due to these drawbacks, another calibration setup is proposed. A threaded screw is installed between through a bracket solid, non moving bracket with a threaded hole in the middle, and to another bracket which is allowed to slide back and forth, using locking nuts. On the movable bracket a secondary load cell is mounted, and when the threaded screw is tightened, the load cell will pull on the primary load cell, via a spring which ensures a steady increase in load. This module was recreated after Mikkel Paulsen's master thesis "Videreutvikling av eksperimentell metode for måling av hydrodynamiske krefter på en foilseksjon" [24], and is shown in Figure 23.
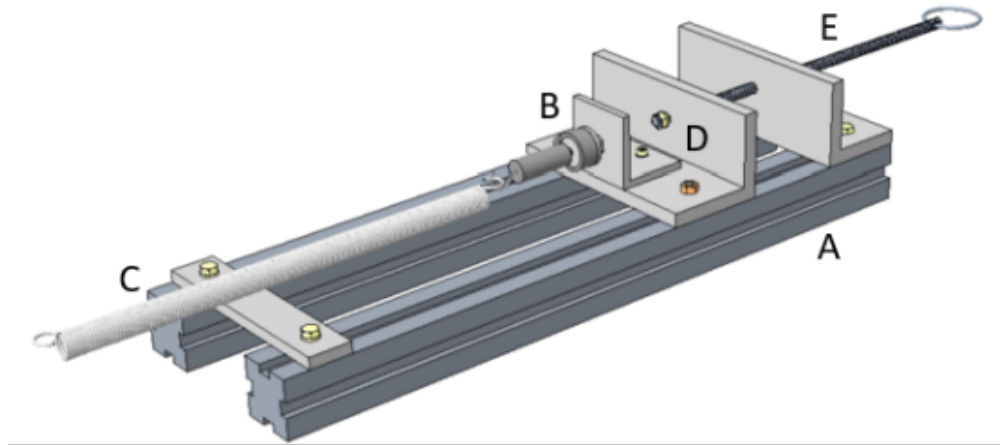
Figure 23: Calibration rig for x-direction load cell. [24]

Here, A are 20x20 mm Aluflex profiles, B shows the attached secondary load cell, C is a spring installed to reduce damage potential of the load cell should jerking movement occur, D is the plate which is allowed to slide and E is the threaded rod which is tightened or loosened to adjust input force. The secondary load cell is a HBM U90 200N load cell which is deemed very accurate after calibration. The calibration of the HBM U90 200N load cell is conducted by hanging it verically from an inflexible bar, and attaching mass increments to it. The calibration steps are shown in Table 18.

Table 18: Calibration steps for HBM U90 200N load cell

Applied load [kg]	Output [mV/V]
0	0.005
2	-0.094
4	-0.193
6	-0.291
8	-0.390
10	-0.489
12	-0.589
14	-0.687
12	-0.589
10	-0.490
8	-0.391
6	-0.292
4	-0.193
2	-0.094
0	0.005

Using a MATLAB script provided by MarinLab, the parameters of the load cell were calculated to the presented values in Table 19.

Table 19: Load cell calibration analysis

Parameter	Value
Gain	-198.295 dN/d(mV/V)
Offset	1.030 N
Maximum error to linear fit	0.020 %
Maximum Hysteresis	0.053 %

The gain value is programmed in during measurement to properly convert the measured mV/V to N, while the offset is an adjustment to the zero point. The low maximum error to linear fit shows that the linearity between applied and measured load behaves linearly, as desired. The low percentage of maximum hysteresis shows that the output when loading and unloading is very close to equal, as it should be. The error of full capacity and hysteresis plots are presented in Figure 24 and Figure 25.
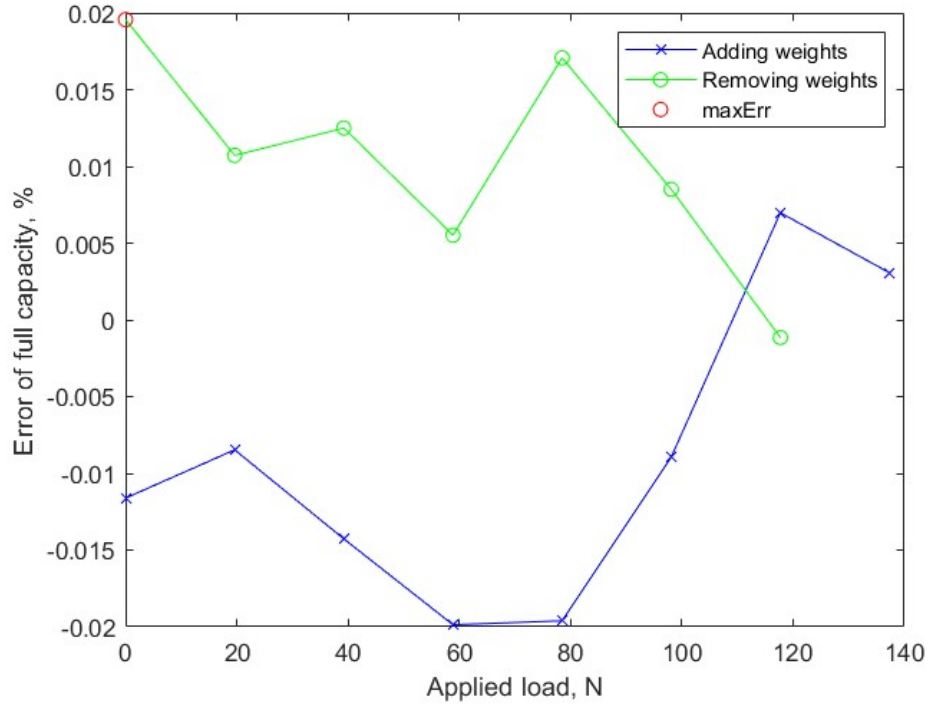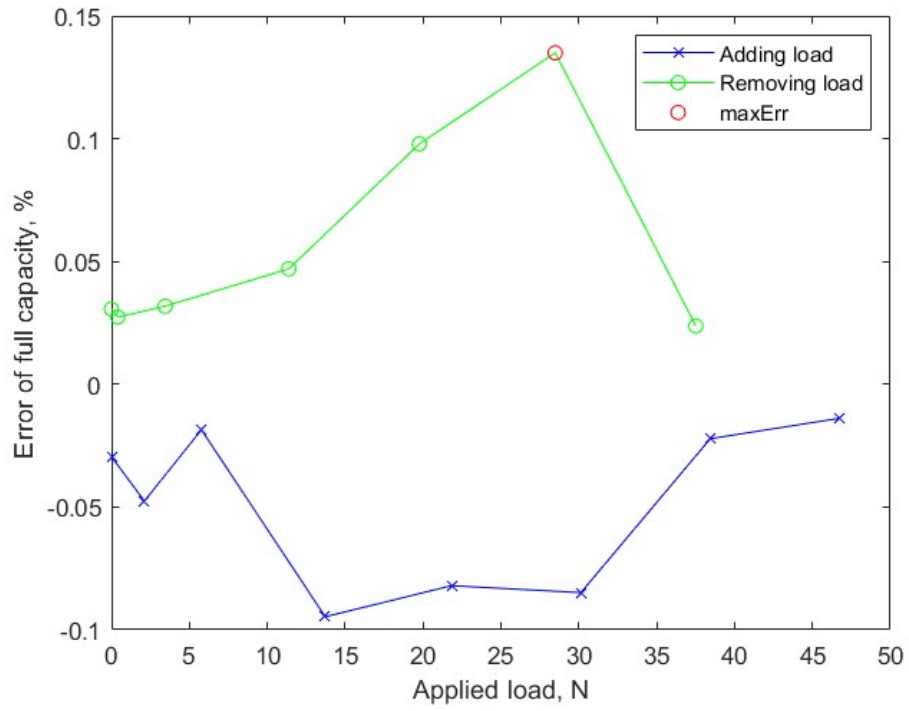
Figure 24: Maximum error of full capacity
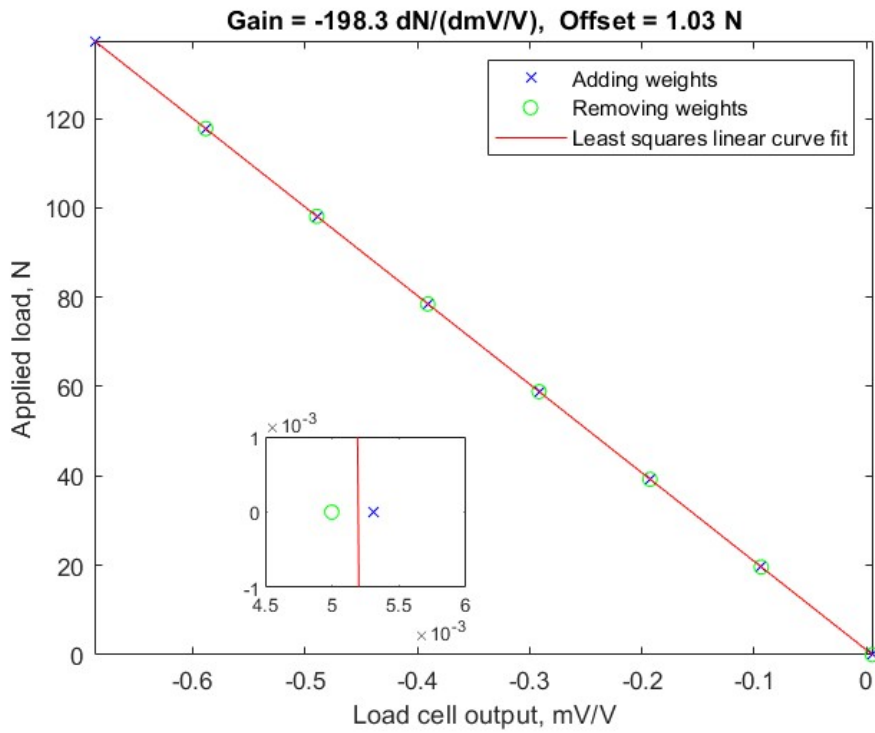
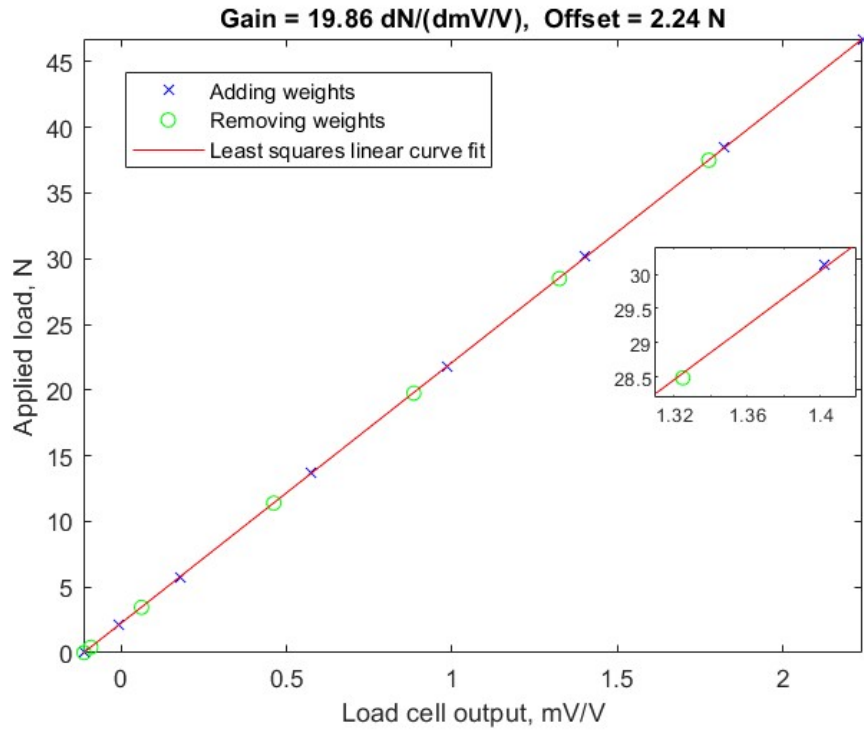Figure 25: Hysteresis

As Figure 24 shows, the maximum error to linear fit occurs at 0 N applied load after unloading, which could be due to the load cell swinging after unloading, due to noise or due to not enough time allowed for the load cell to settle before recording the output.

Figure 25 shows the hysteresis. As the plot shows, the load cell works well with respect to the least squares linear curve fit, which is what it should. Zooming in on 0 N on the hysteresis plot, where Figure 24 showed that the maximum error occurs, the hysteresis is shown better. This is shown in the inset zoom at the hysteresis plot. Note that as the data showed, the maximum hysteresis is 0.053 %, so the scale of the x-axis in this zoom is at a magnitude of 10^{-3}.

After the calibration of the secondary HBM U90 200N load cell is complete, the calibration rig is installed on the carriage. The secondary load cell is attached through a spring, to a bolt close to where the buoy is going to be, to replicate the loading point as well as possible. The installed calibration rig, connected to the primary load cell is shown in Figure 26.
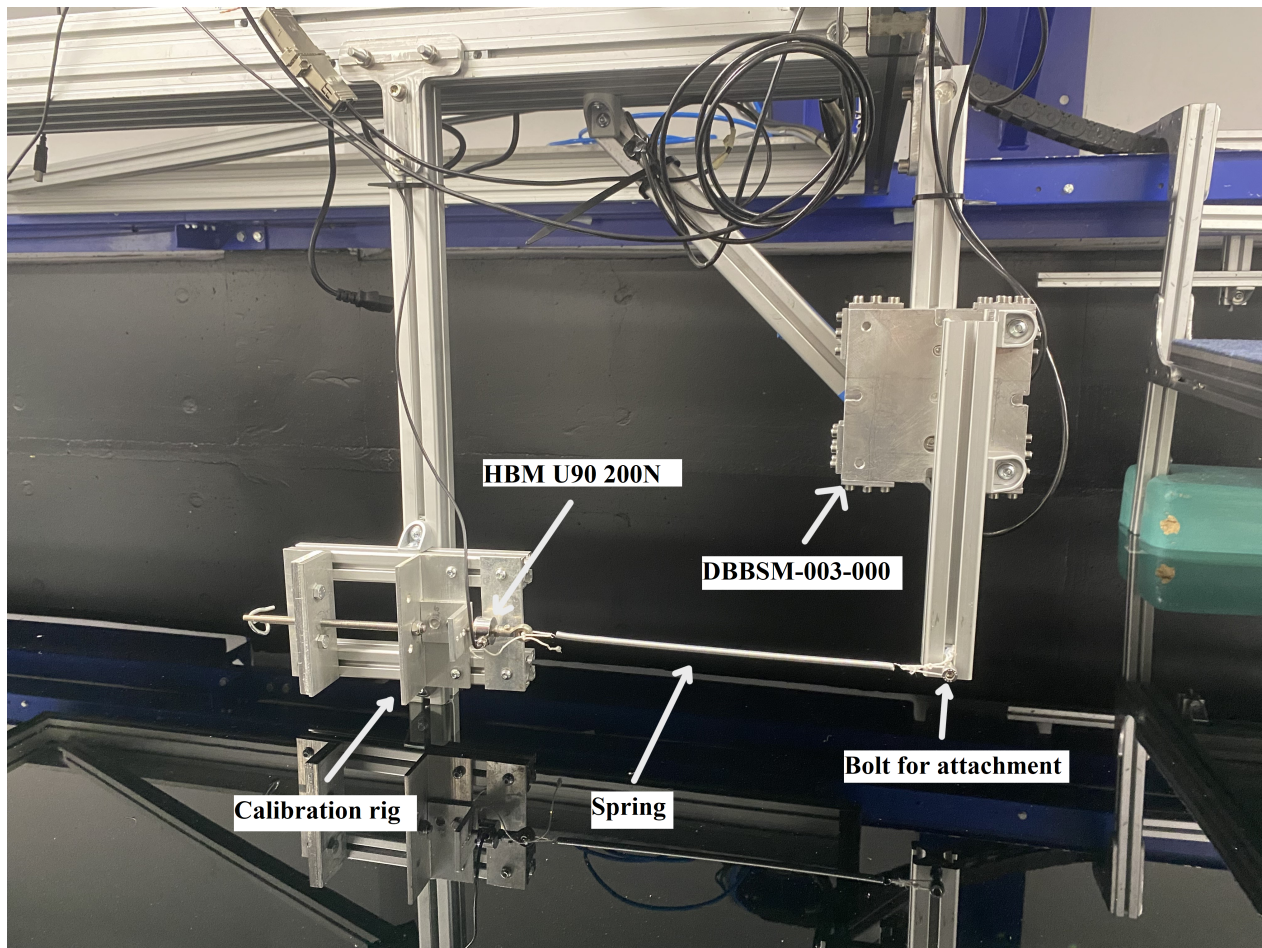
Figure 26: Image of the calibration rig connected to the x-direction load cell

By tightening the threaded rod, an evenly increasing load is applied to the primary load cell. As the applied load is measured by the HBM U90 200N load cell, the applied load is in newtons. The calibration increments are presented in Table 20.

Table 20: Calibration steps for DBBSM-003-000 load cell in x-direction

Applied load [N]	Output x-direction [mV/V]	Output z-direction [mV/V]
0	-0.113	-0.660
2.11	-0.008	-0.662
5.77	0.177	-0.657
13.7	0.576	-0.653
21.8	0.984	-0.644
30.1	1.402	-0.638
38.4	1.822	-0.630
46.7	2.240	-0.626
37.5	1.776	-0.636
28.5	1.325	-0.642
19.8	0.885	-0.649
11.4	0.462	-0.658
3.45	0.062	-0.663
0.40	-0.092	-0.664
0	-0.112	-0.661

By using MatLab, the parameters of the load cell are calculated to the values shown in Table 21.

Table 21: Load cell calibration analysis

Parameter	Value
Gain	19.864 dN/d(mV/V)
Offset	2.238 N
Maximum error to linear fit	0.135 %
Maximum Hysteresis	4.912 %

As with the HBM load cell, the gain is programmed in during measurement to properly convert the measured mV/mV to N, while the offset is an adjustment to the zero point. The maximum error to linear fit is larger for the DBBSM load cell than for the HBM load cell, as expected due to the former assumption that the HBM load cell is more accurate. Still, the error to linear fit is not too high. The hysteresis is also larger for the DBBSM load cell, which could be due to the accuracy of the load cell, mistakes during the loading and unloading process, or due to the aforementioned coupling effect. The error of full capacity

and hysteresis plots are presented in Figure 27 and Figure 28.

Figure 27: Maximum error of full capacity

Gain = 19.86 dN/(dmV/V), Offset = 2.24 N

Figure 28: Hysteresis

Figure 27 shows that the maximum error to linear fit occurs at approximately 30 N. Still, by looking at Figure 28, the measurements shows good correspondence to the least squares linear curve fit.

5.6   Calibration of z-direction load cell

For the load cell recording the z-direction, the process is simple. A bolt with a loop is fastened to the load cell, and from the loop the mass increments are attached. A few simplifications to the recommended ITTC recommendations are made due to limited equipment. The 10 mass increments was not possible to acquire, and the full range of the load cell was not possible to reach. Instead, 7 mass increments were used, covering a range deemed acceptable given the expected loads in the experiment itself. The outputs from both load cells are recorded to investigate possible cross coupling effects. The mass increments and outputs recorded in this calibration procedure, are presented in Table 22.

Table 22: Calibration steps for DBBSM-003-000 load cell in z-direction

Total mass applied [kg]	Output in x-direction [mV/V]	Output in z-direction [mV/V]
0	-0.114	-0.349
0.5	-0.112	-0.565
1	-0.109	-0.780
1.5	-0.107	-0.995
2	-0.106	-1.210
2.5	-0.104	-1.426
3.5	-0.099	-1.855
4.5	-0.095	-2.283
3.5	-0.101	-1.855
2.5	-0.104	-1.425
2	-0.105	-1.210
1.5	-0.107	-0.995
1	-0.110	-0.779
0.5	-0.112	-0.563
0	-0.114	-0.348

The data is analyzed in MATLAB, and the following parameters in Table 23 are calculated.

Table 23: Load cell calibration analysis

Parameter	Value
Gain	-22.810 dN/d(mV/V)
Offset	-7.968 N
Maximum error to linear fit	0.044 %
Maximum Hysteresis	-0.003 %

As with the other load cells, the gain is used inserted into the data acquisition software, while the offset is used to adjust the zero point. As the load cell is connected to the x-direction load cell on one side, but free on the other side, the cross coupling effect does not affect this load cell, unlike for the x-direction load cell. This is shown by the smaller maximum error to linear fit and the low hysteresis. As stated during the calibration of the x-direction load cell, the hysteresis might be smaller due to more consideration when increasing the load increments as well. The error of full capacity and hysteresis plots are presented in Figure 29 and Figure 30.
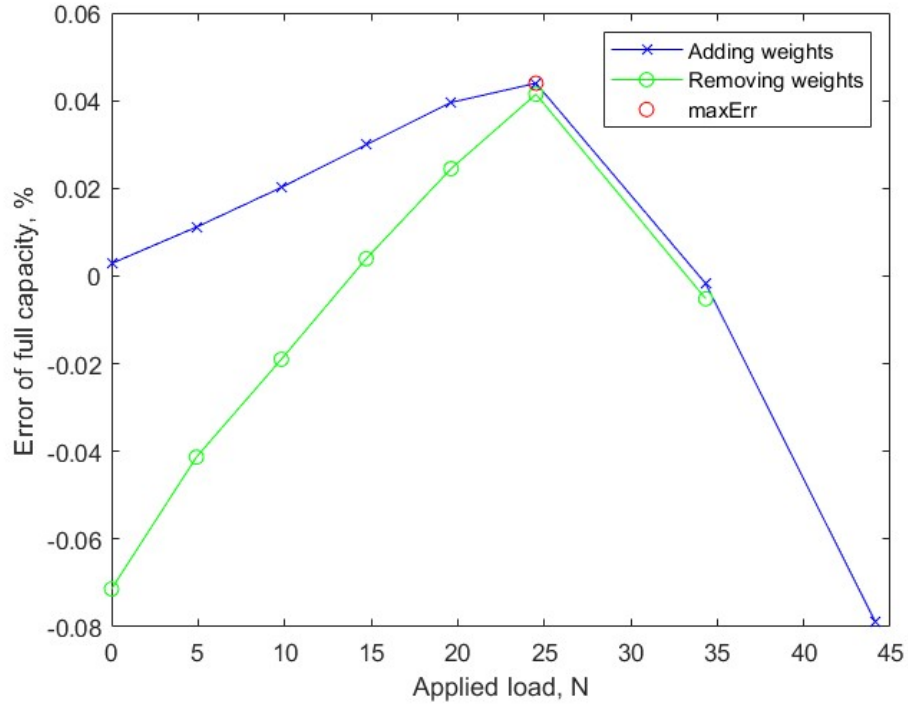
Figure 29: Maximum error of full capacity
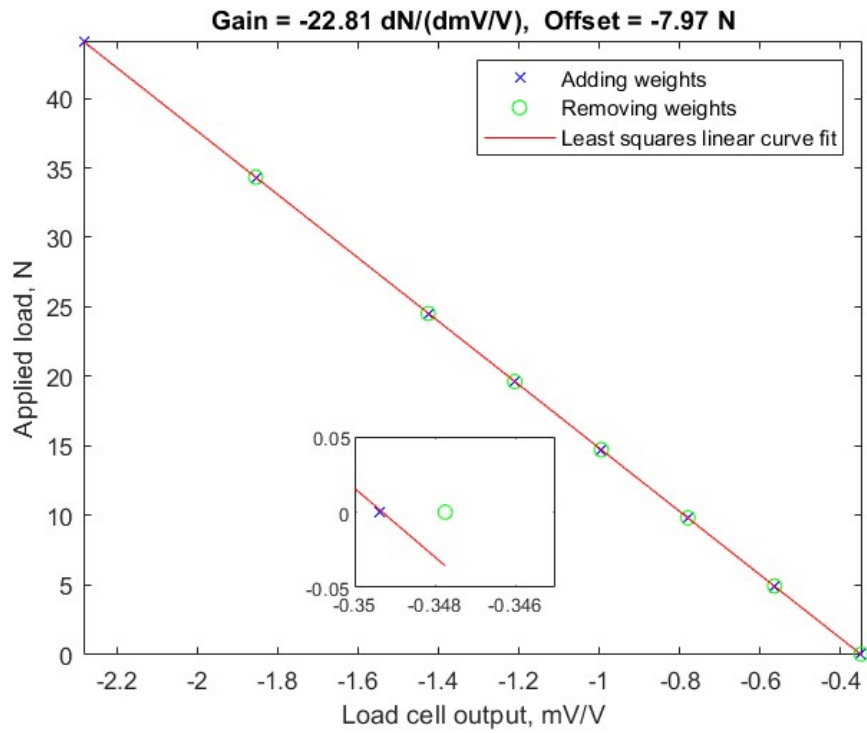
Figure 30: Hysteresis

As Table 23 suggests, the linearity is intact, and the hysteresis is low. This is reflected in Figure 29, where the maximum error is low, and the curves for loading and unloading of the cell follows each others trajectory, especially with higher loads. Figure 30 also shows that the loading and unloading process is very good with respect to the least squares linear curve fit. The hysteresis where the maximum error to linear fit are the farthest apart, at 0 N, is zoomed in and shown the figure. As the small range on the zoomed axes, as well as Table 23 suggests, the hysteresis is minimal, and the load cell is calibrated.

5.7   Checking the coupling effect

After calibration, a test is run to check the coupling effect. The same calibration rig that was used to calibrate the x-direction load cell is placed at an angle of approximately 45°. This setup is shown in Figure 31.
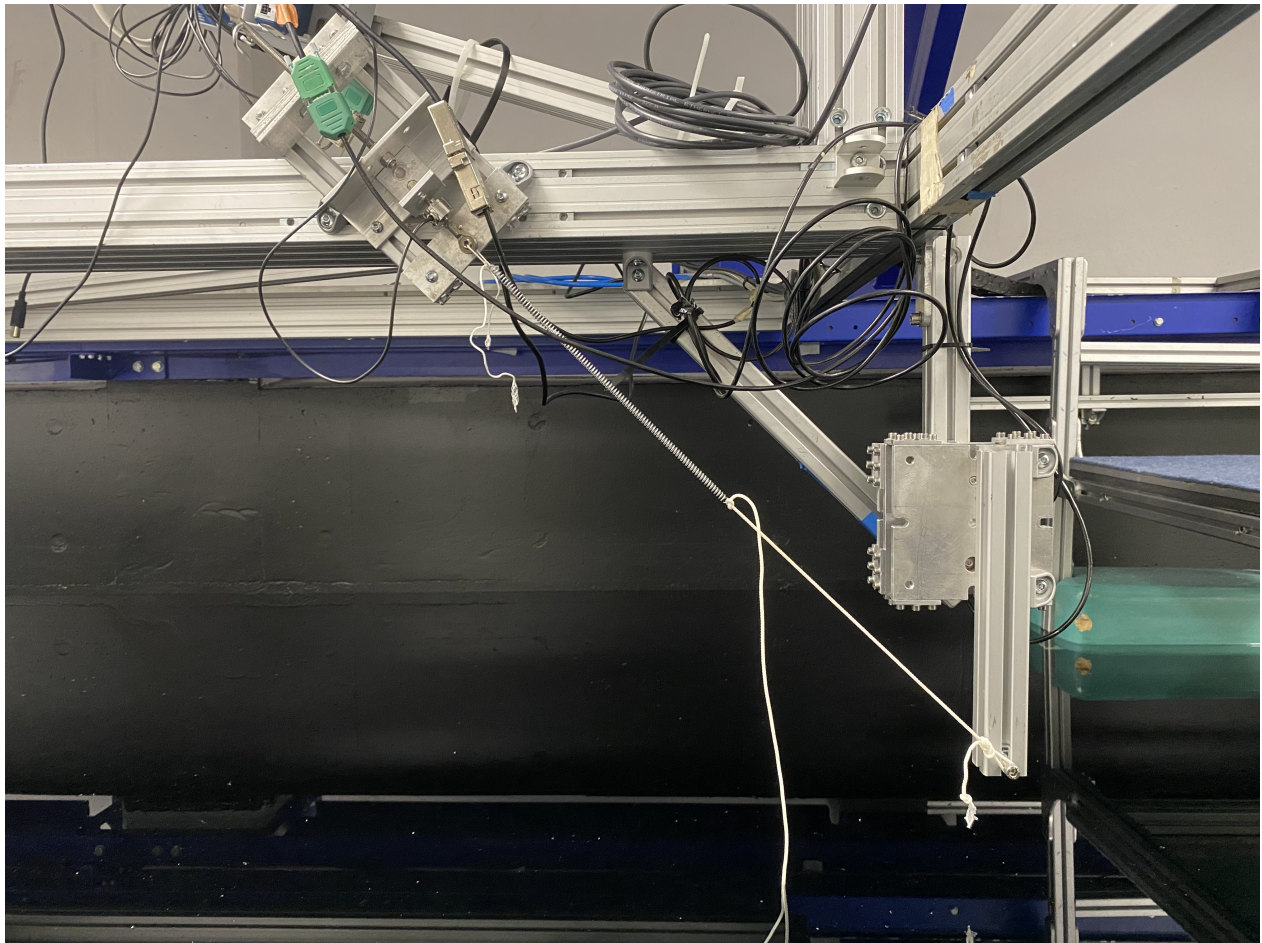
Figure 31: Image showing the verification test

In theory, when loading the load cells at an angle of 45°, $F_x = F_z = F \cdot F cos(45°) =$

$F \cdot sin(45°) = 0.5 \cdot F$. Therefore, the MatLab script should give the same gain for both load cells. The loading and unloading increments with the outputs are shown in Table 24.

Table 24: Loading and unloading at a 45°angle

Applied load [N]	Output x-direction [mV/V]	Output z-direction [mV/V]
0	-0.113	-0.660
3.516	0.013	-0.552
10.165	0.246	-0.345
17.216	0.495	-0.123
24.665	0.754	0.107
32.269	1.023	0.347
23.035	0.706	0.062
14.704	0.414	-0.197
8.400	0.188	-0.401
4.350	0.045	-0.526
0	-0.111	-0.659

Analysis of the data points leads to the results presented in Table 25.

Table 25: Load cell verification results

Parameter	x-direction load cell	z-direction load cell
Gain	28.423 dN/d(mV/V)	32.002 dN/d(mV/V)

Given that this process is a validation, rather than a calibration, the 45°angle is made by using a protractor and eye measurements, as well as the placement of the spring being done by eye measurement. This means that there are uncertainties to this setup, so it is expected that the results are not completely equal. Therefore, the difference of $\approx 4dN/d(mV/V)$ is deemed acceptable as a proof of concept, and the load cells are deemed to give reliable output when under the influence of wave loads.

5.8 Wave gauge calibration

To check whether the input data produces the desired wave, two wave gauges are installed. An attempt to record the wave data simultaneously as the loads is made by connecting a wave gauge through the same DAQ unit as the load cells. This is calibrated by checking the voltage output at the zero position (still water level), plus 10 cm and minus 10 cm from

zero. Assuming linearity, the gain is calculated by solving two equations with 2 unknowns. Unfortunately, the attempt failed, probably due to a faulty resistor or capacitor in the recorder. While the shape of the wave and the desired simultaneity is correct, the wave height is incorrect. This is likely due to unstable gain and drift. The problem could not be solved as spare parts was not available at the facility, and even if the parts were available, the fix would be too time consuming for the allocated time in the facility.

The other wave gauge is located besides the first one, and is connected directly to the same board that controls the wave generator. To calibrate this, a program at MarinLab automatically calibrates the gain, and sets the internal resistance, by prompting the user to short circuit the wave gauge. This is done by using a banana cable. After this procedure is carried out, a selection of waves were run through the wave generator, and the output was recorded. The waves with an amplitude of 0.04, 0.06 and 0.08 m respectively, with a frequency of 0.3 Hz are presented in Figure 32, Figure 33 and Figure 34.
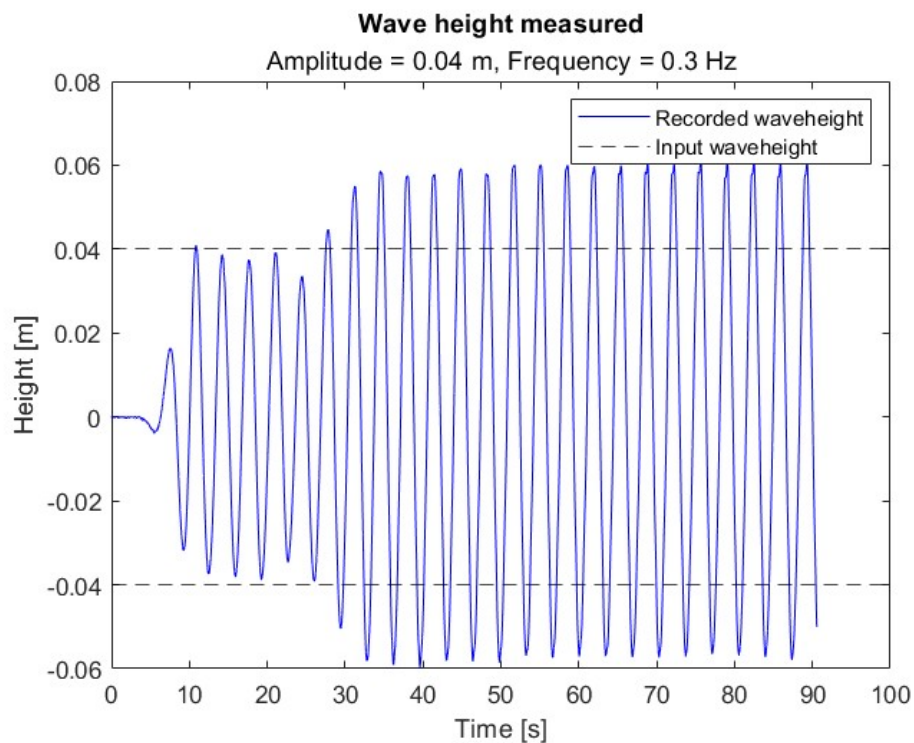
Figure 32: A = 0.04 m and f = 0.3 Hz
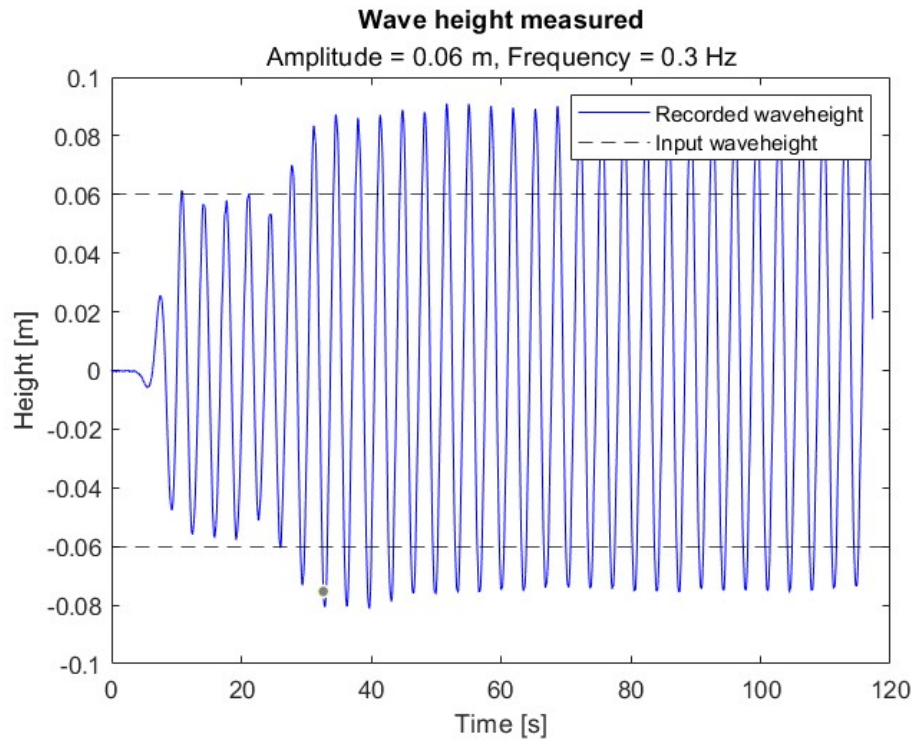
Figure 33: A = 0.06 m and f = 0.3 Hz
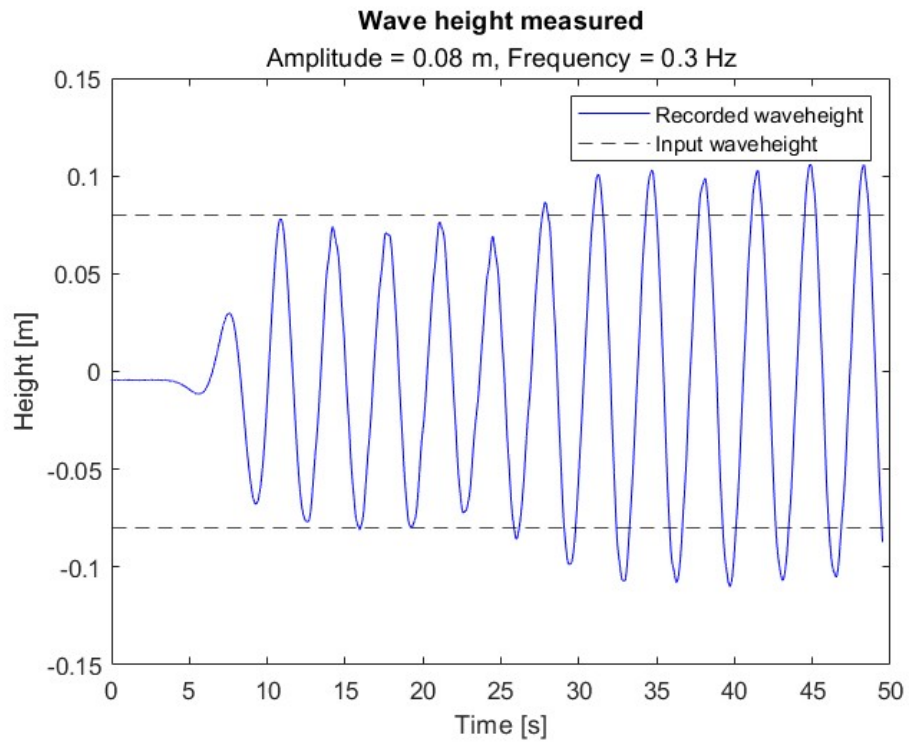
Figure 34: A = 0.08 m and f = 0.3 Hz

For the waves with a frequency of 0.3 Hz, an interesting phenomenon occurs. As the figures show, after ≈ 20 seconds, the wave amplitude increases above the input value (the dotted lines). This is due to the length of the wave corresponding to the length of the wave basin, and therefore, the porous beach at the end of the tank is not able to fully absorb the energy. This causes the waves to reflect back, and due to constructive interference, standing waves are formed. To account for this, load data captured before ≈ 20 seconds will be analysed. For the other frequencies, the standing wave events do not occur as shown in Figure 35 to Figure 40.
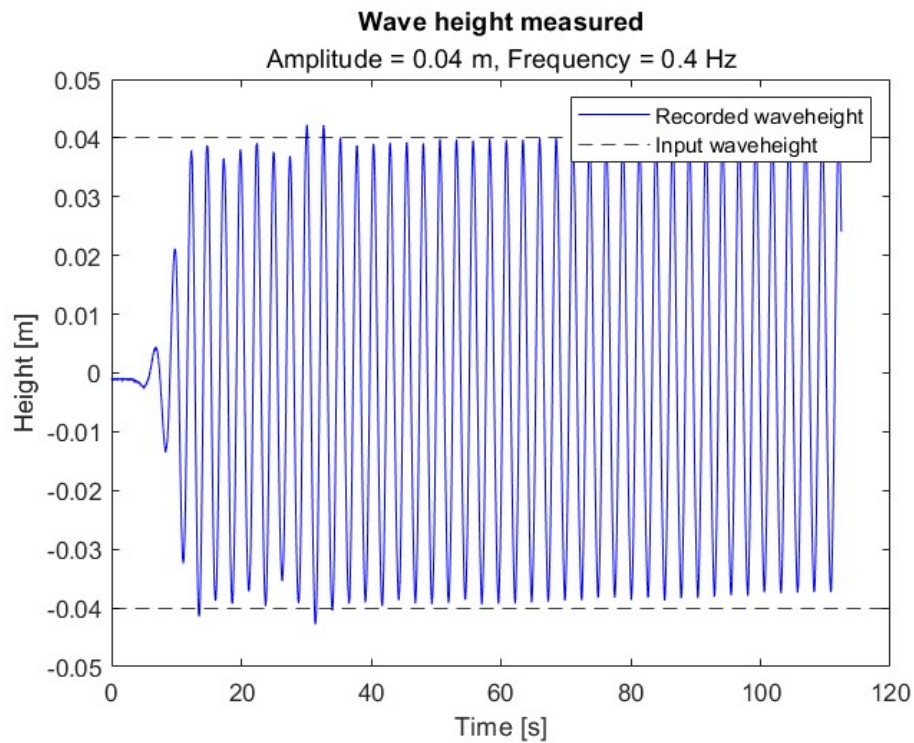
Figure 35: A = 0.04 m and f = 0.4 Hz
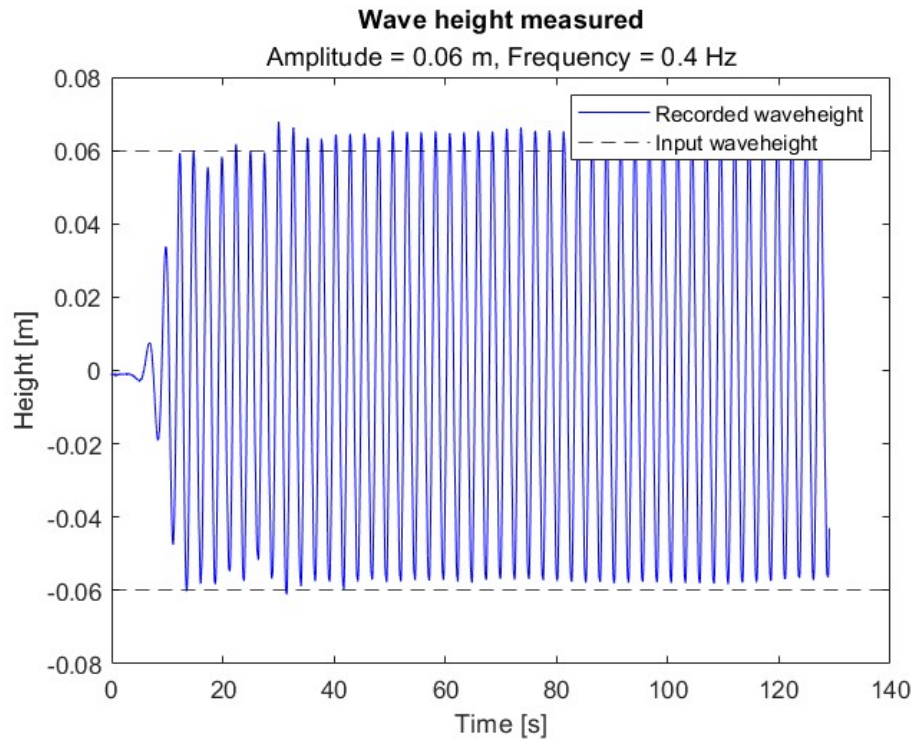
Figure 36: A = 0.06 m and f = 0.4 Hz
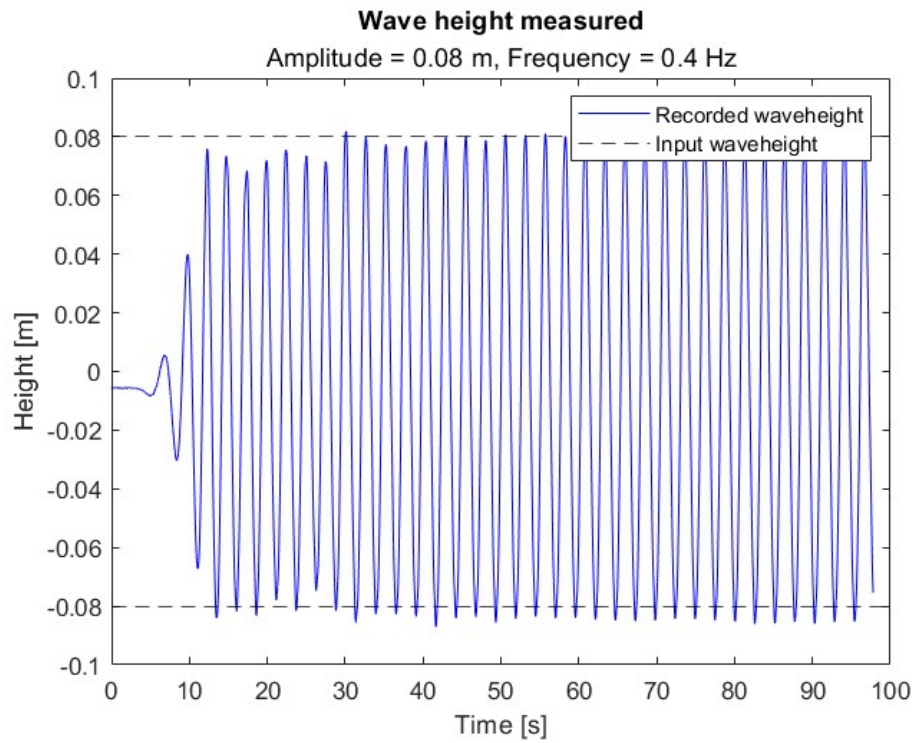
Figure 37: A = 0.08 m and f = 0.4 Hz
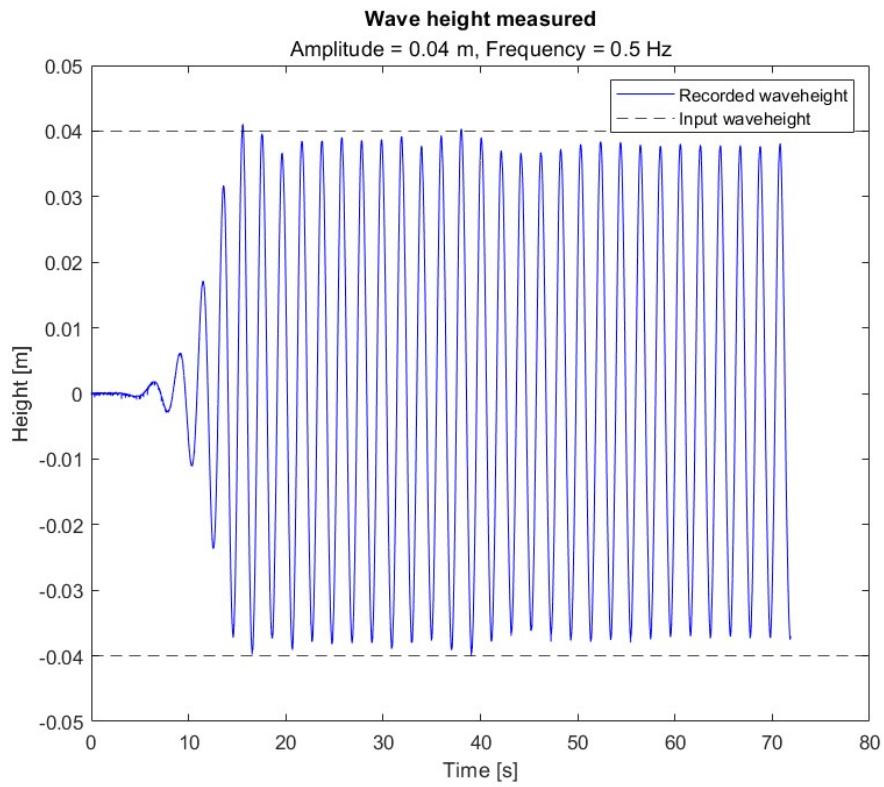
Figure 38: A = 0.04 m and f = 0.5 Hz
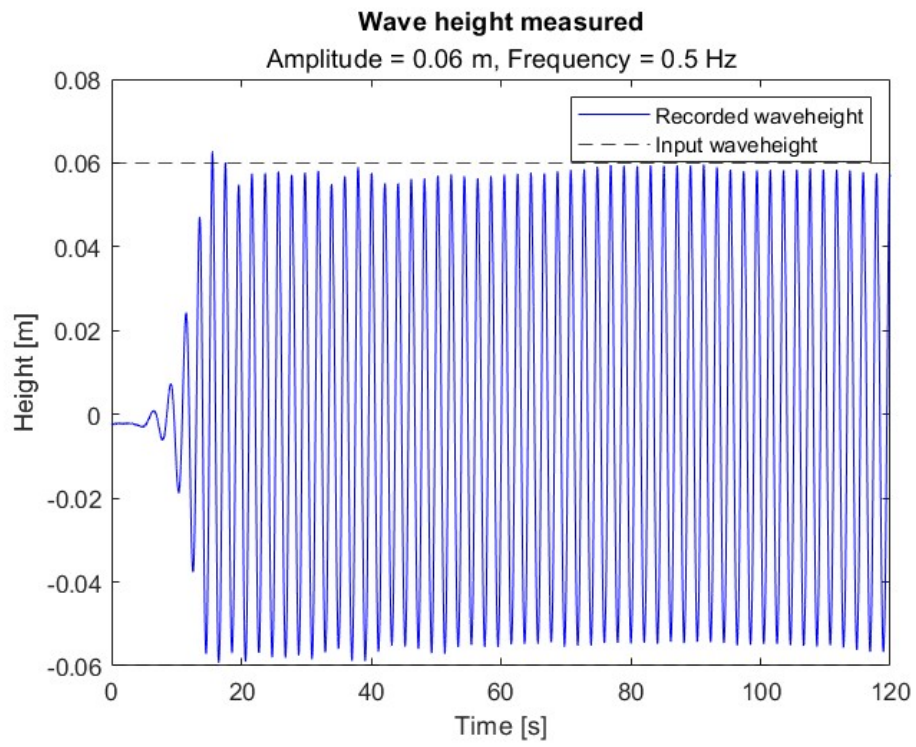
Figure 39: A = 0.06 m and f = 0.5 Hz
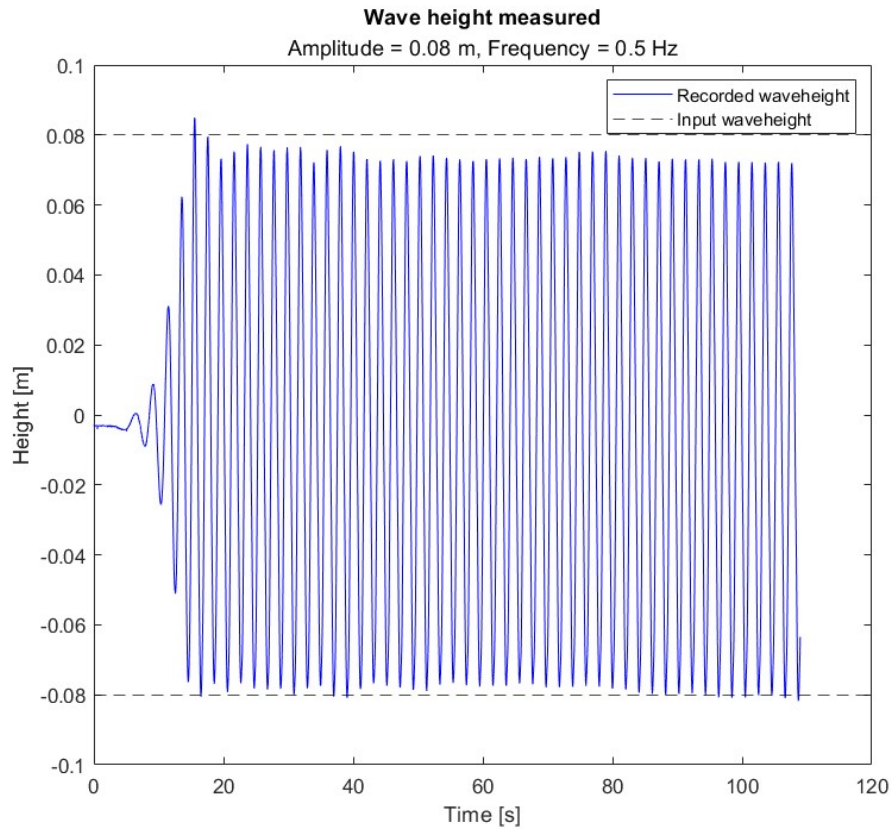
Figure 40: A = 0.08 m and f = 0.5 Hz

As the figures show, the wave height is close to the input for the non-standing waves. For the waves with a frequency of 0.4 Hz, the waves seem to be a bit larger than the input, but within a tolerable magnitude. For the waves with a frequency of 0.5 Hz, the waves seems to be a bit smaller than the input value, especially for the waves with an amplitude of 0.08 m as shown in Figure 40. This wave is pushing the limit for what is acceptable, but due to time restrictions in MarinLab, it is accepted, but data captured before $\approx$ 40 seconds are used as the waves decrease slightly after this.

5.9 Post-experiment calibration

To ensure the initial calibration of each load cell is valid, and that the gain and offset has not drifted significantly during the experiments, the load cells are re-calibrated after running the experiment. The same calibration procedure is conducted, to avoid external influence when re-calibrating. The gain, offset, maximum error to linear fit and maximum hysteresis from the initial calibration, post-calibration and their differences are presented in Table 26 for the x-direction load cell and Table 27 for the z-direction load cell.

Table 26: Comparison of calibration of the x-direction load cell before and after the experiment

X-direction	Before experiment	After experiment	Difference
Gain	19.864 dN/d(mV/V)	19.842 dN/d(mV/V)	0.022 dN/d(mV/V)
Offset	2.238 N	2.106 N	0.132 N
Maximum error to linear fit	0.135 %	0.095 %	0.04 %
Maximum hysteresis	4.912 %	7.408 %	2.496 %

Table 27: Comparison of calibration of the z-direction load cell before and after the experiment

Z-direction	Before experiment	After experiment	Difference
Gain	-22.810 dN/d(mV/V)	-22.804 dN/d(mV/V)	0.006 dN/d(mV/V)
Offset	-7.968 N	-8.085 N	- 0.117 N
Maximum error to linear fit	0.044 %	0.103 %	0.059 %
Maximum hysteresis	-0.003 %	8.816 %	8.819 %

From these tables, the load cell drift from start to the end of the experiments looks within reason. No major shift in neither gain or offset are observed. The one noticeable change is the change in maximum hysteresis in the z-direction load cell. As the load cell was calibrated by adding mass increments, it is possible that the increased hysteresis is an effect of carelessness while loading and unloading the cell. The most important factors here are still the gain and offset, to assure that the values of the recorded data has been are reliable. As the difference in these parameters are small, compared to the ranges of loads, the data is reliable.

6 Results

This section will cover the results from 2D and 3D simulations and experimental testing. For simplicity, the different waves will be named as shown in Table 28.

Table 28: Naming of wave cases

Wave height [m] \Frequency [Hz]	0.3	0.4	0.5
0.08	Case 1	Case 2	Case 3
0.12	Case 4	Case 5	Case 6
0.16	Case 7	Case 8	Case 9

6.1 3D simulation results

This subsection will cover the data processing procedure and the resulting plots from the 3D simulations.

To analyze the numerical 3D simulated data, the data has to be processed. The data is zeroed to only account for effects from the waves, the initial data from before the solution stabilizes is cut out, and the magnitude of the data points are doubled, as using symmetry means that the recorded forces are for half of the sphere. These steps are taken for all fluid domains.

For the cases where the frequency is 0.3 seconds, the data is cut after the solution stabilizes. This is shown in Figure 41 and Figure 42, for lift and drag force respectively. This process is the same for all cases, so the process is exemplified using case 1.
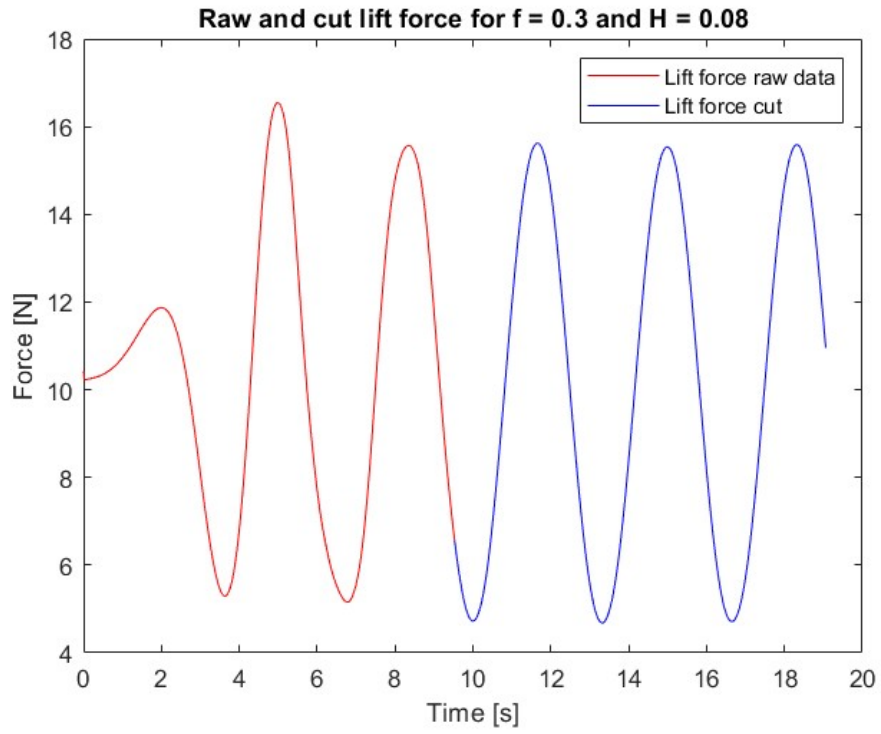
Figure 41: Raw and cut lift force data for case 1
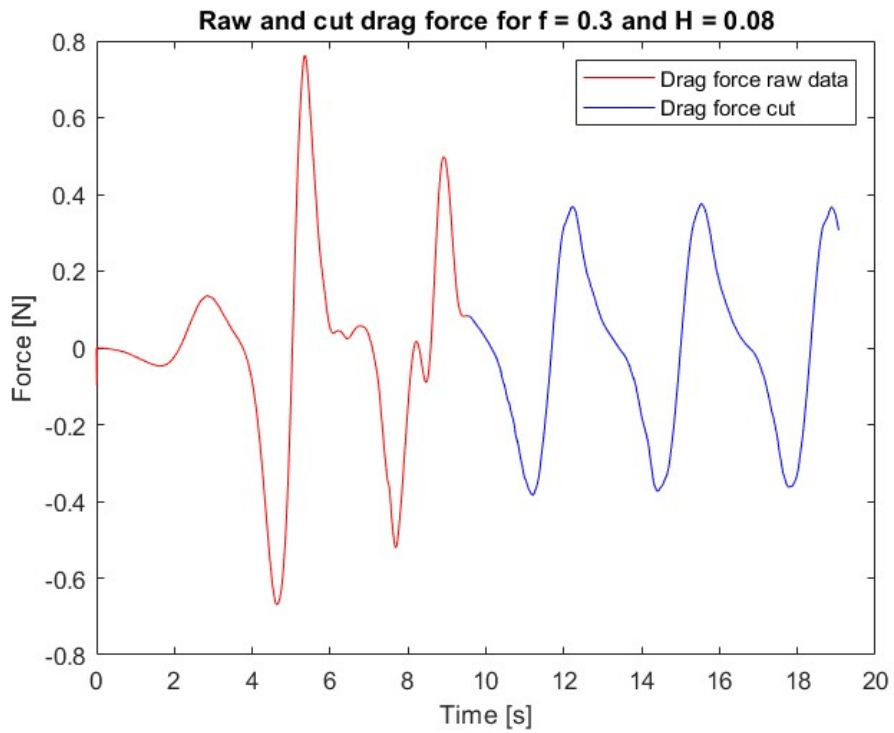
Figure 42: Raw and cut drag force data for case 1

As the figure shows, the data stabilizes a bit before the data is cut, but a safety margin is used to ensure only stable data is considered. The plot also shows that the oscillations are offset from zero. Therefore, the mean value of the cut data is calculated, and subtracted from the data points, to zero the data around y = 0, and the data points are doubled to account for symmetry. The zeroed and doubled force plots for all cases are shown in Figure 43 to Figure 51.
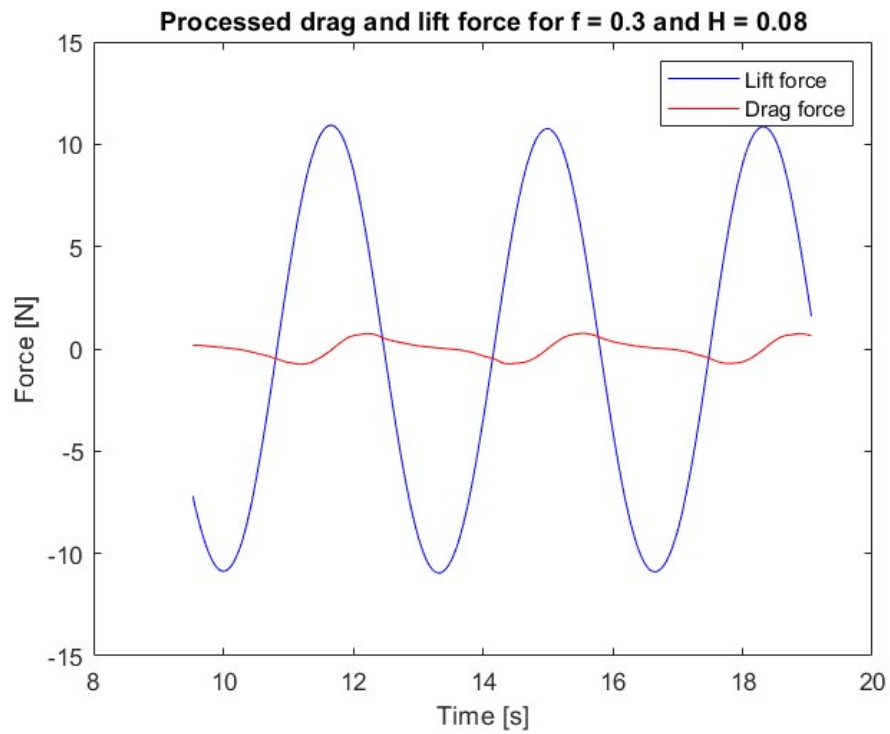
Figure 43: Drag and lift force plot for case 1 after zeroing and doubling
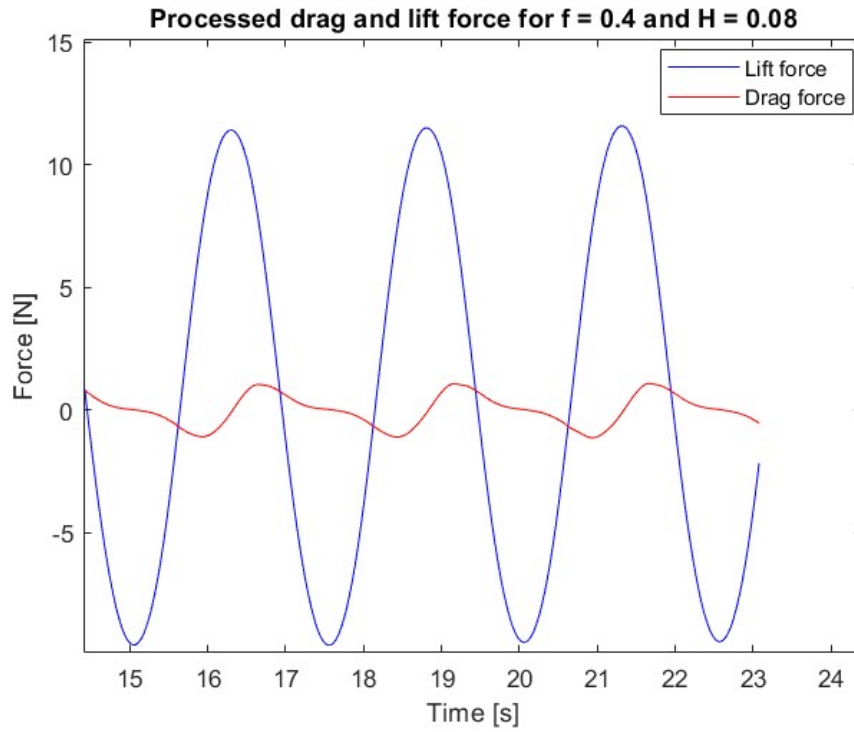
Figure 44: Drag and lift force plot for case 2 after zeroing and doubling
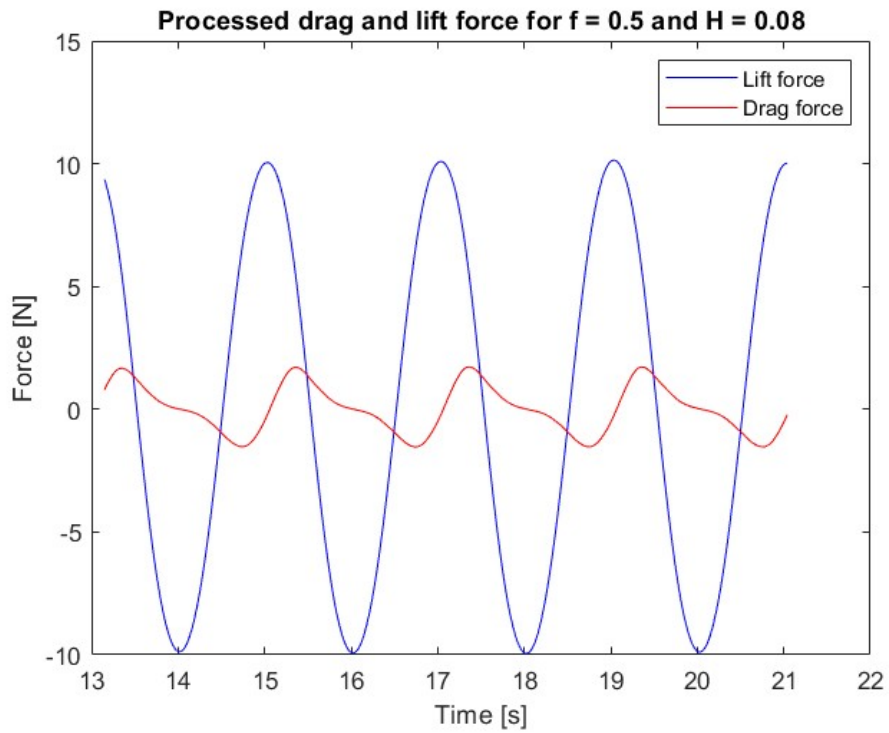
Figure 45: Drag and lift force plot for case 3 after zeroing and doubling
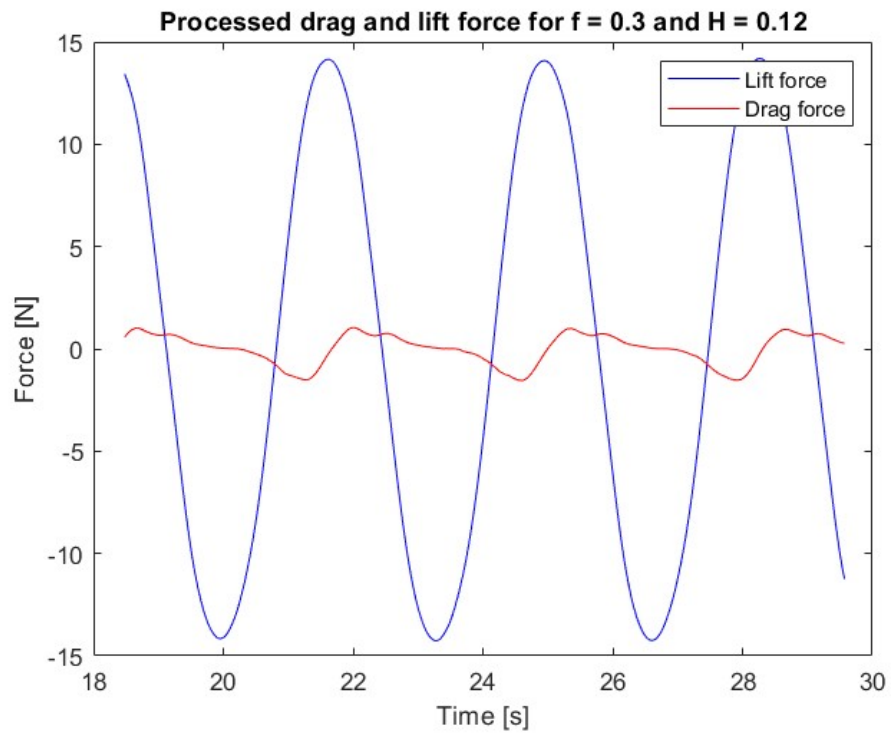
Figure 46: Drag and lift force plot for case 4 after zeroing and doubling
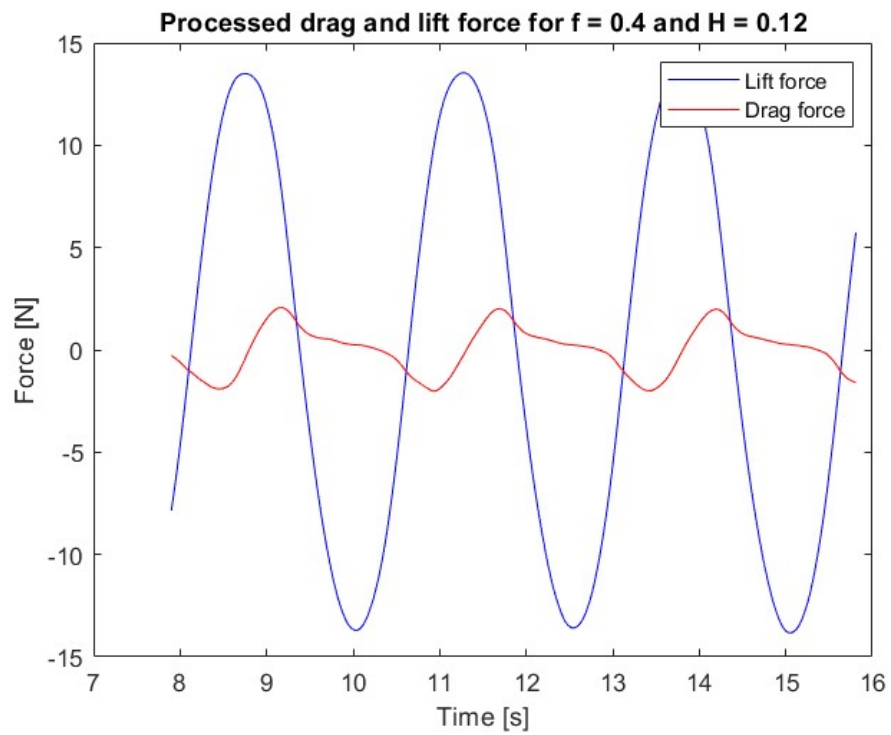
Figure 47: Drag and lift force plot for case 5 after zeroing and doubling
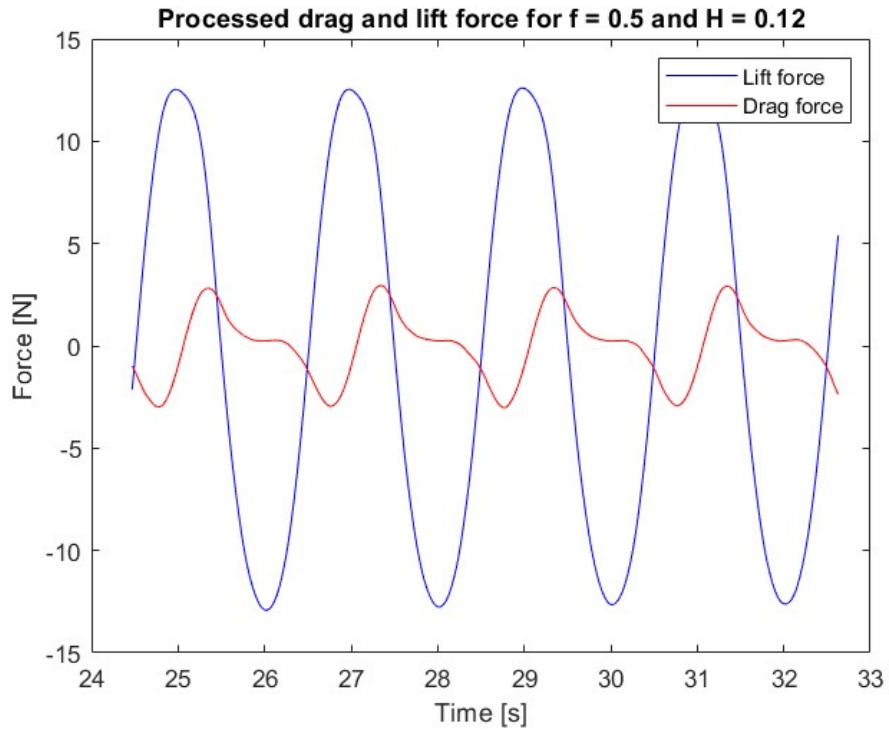
Figure 48: Drag and lift force plot for case 6 after zeroing and doubling
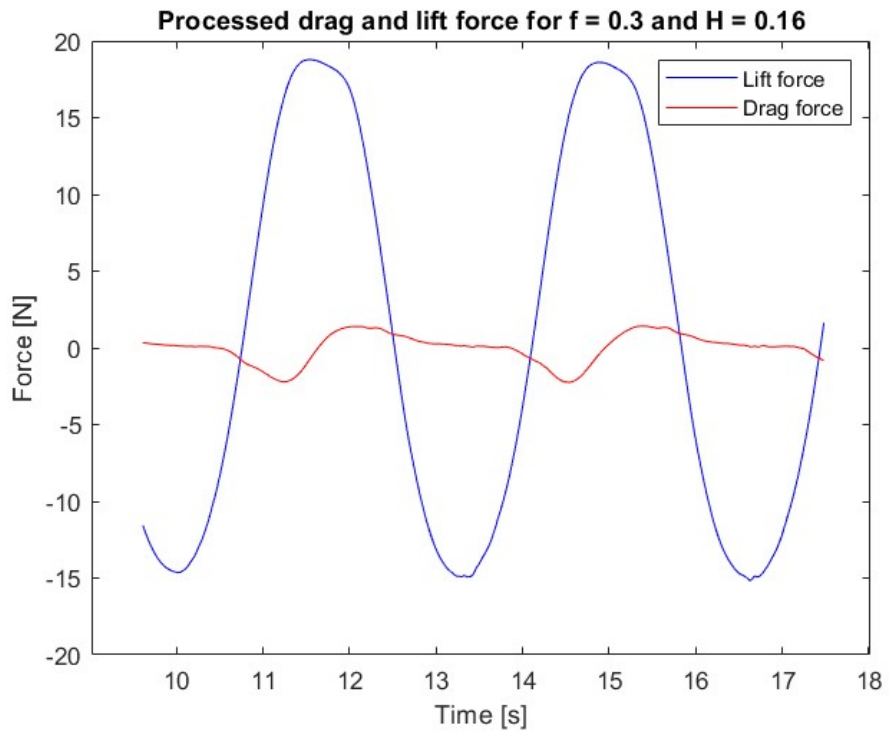
Figure 49: Drag and lift force plot for case 7 after zeroing and doubling
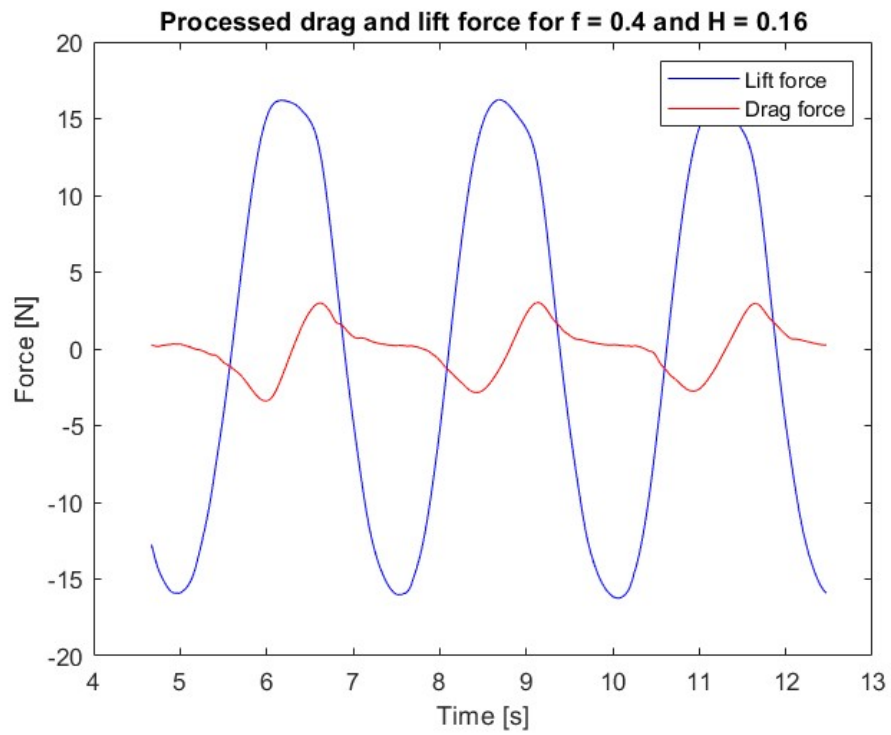
Figure 50: Drag and lift force plot for case 8 after zeroing and doubling
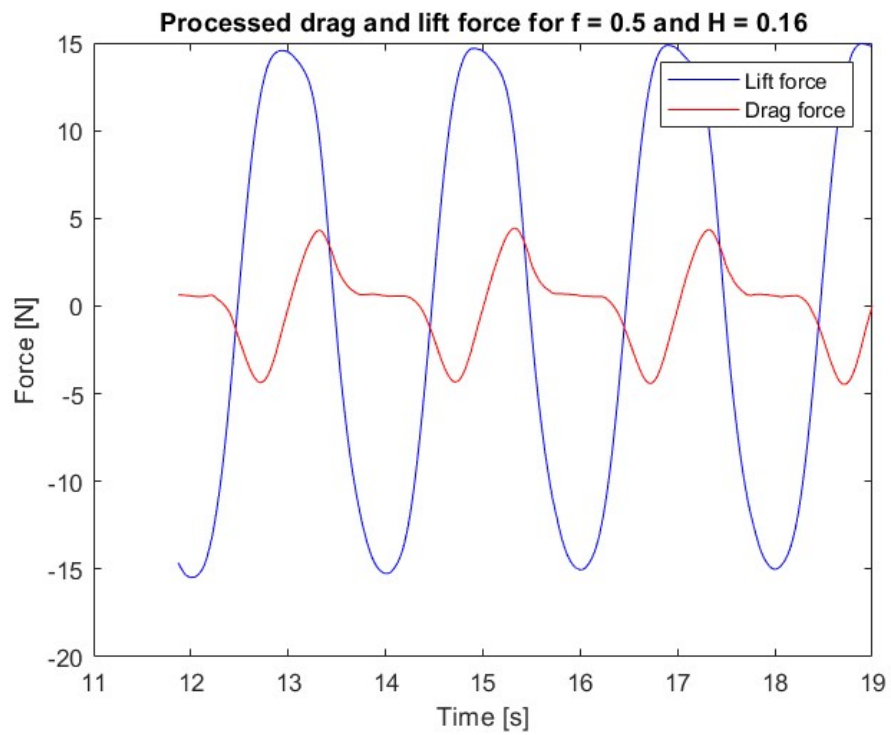
Figure 51: Drag and lift force plot for case 9 after zeroing and doubling

These figures all show the same pattern, where the lift forces oscillates harmonically between their crests and troughs, while the drag forces have a plateau where the force is zero, when the lift forces are at their lowest. This is due to the momentary halt in motion as the waves go from a descending to an ascending motion, when the vertical direction gradient is equal to 0.

6.2   Experimental testing results

For the experimental tests, the data was collected at increments of 10 seconds. As shown in section 5.8, the capture increment will have to occur before the waves become standing for waves with a frequency of 0.3 Hz. For the rest of the waves, a later increment can be used, to allow maximum time for the waves to build up. As the LabVIEW software is used to zero the data, the output can be directly plotted in MATLAB, without cutting or zeroing. The plot for cases 1-9 are shown in Figure 52 to Figure 60.
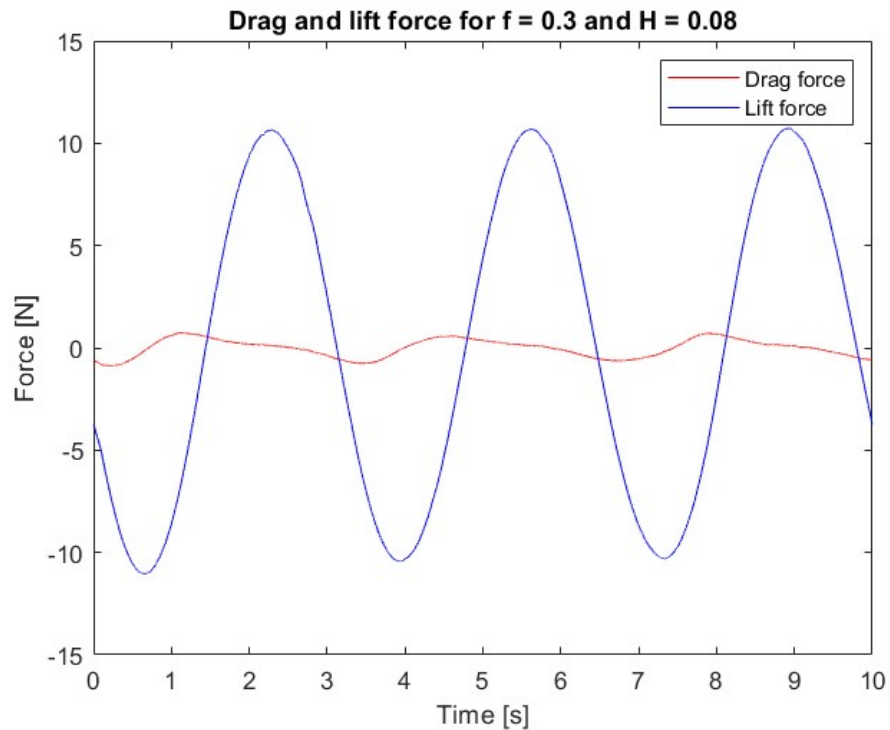
Figure 52: Experimental drag and lift force for case 1
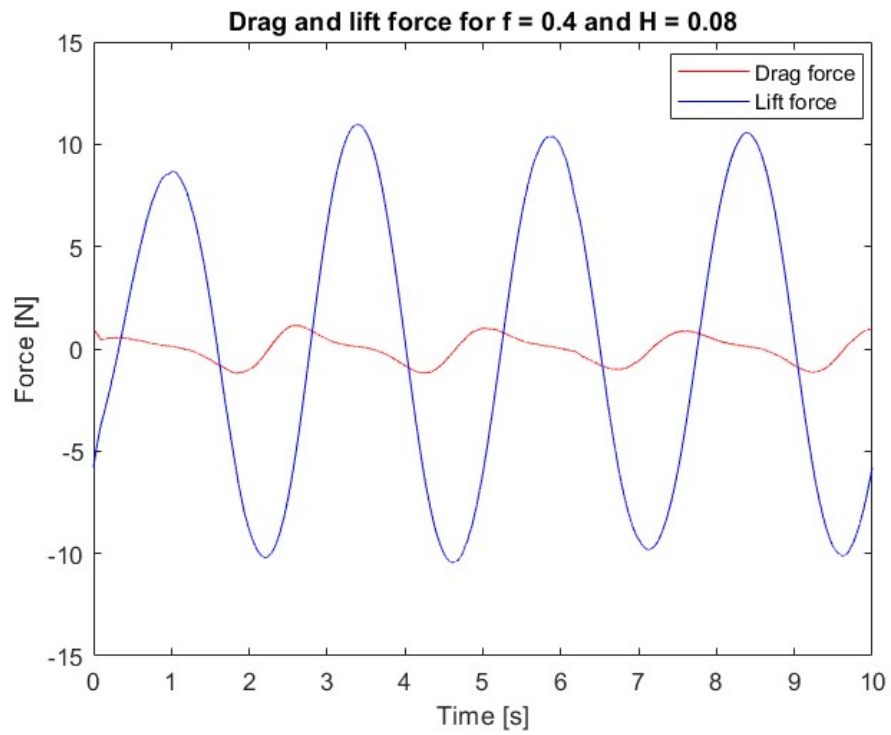
Figure 53: Experimental drag and lift force for case 2
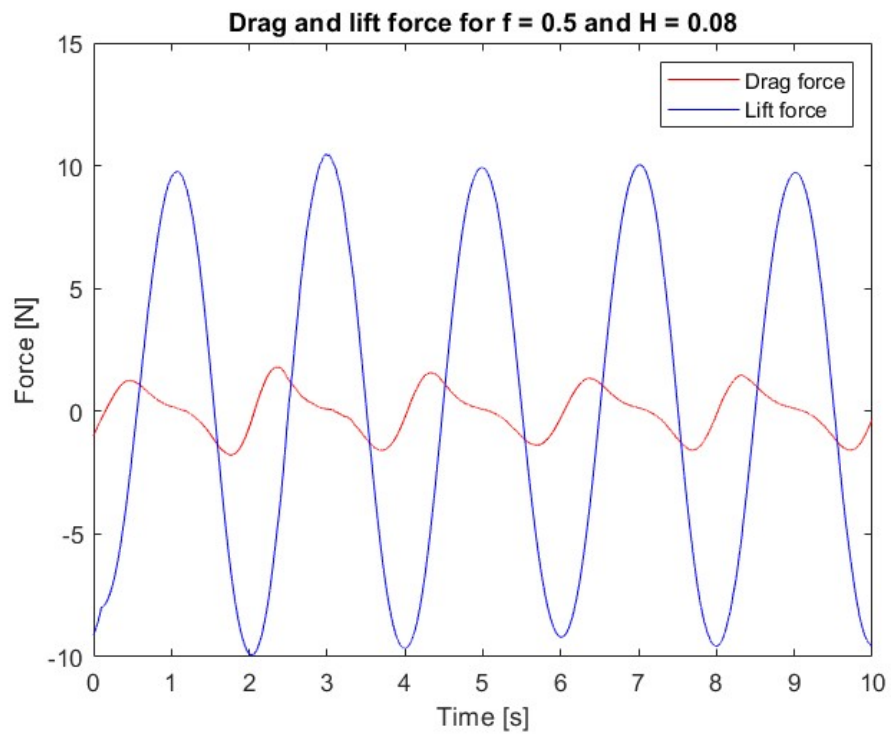
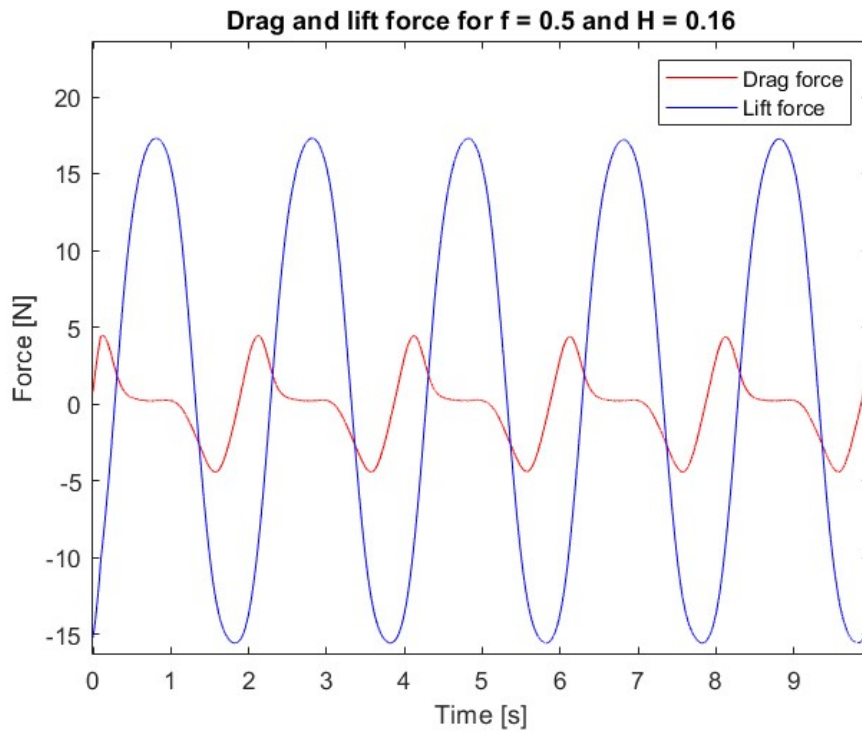Figure 54: Experimental drag and lift force for case 3
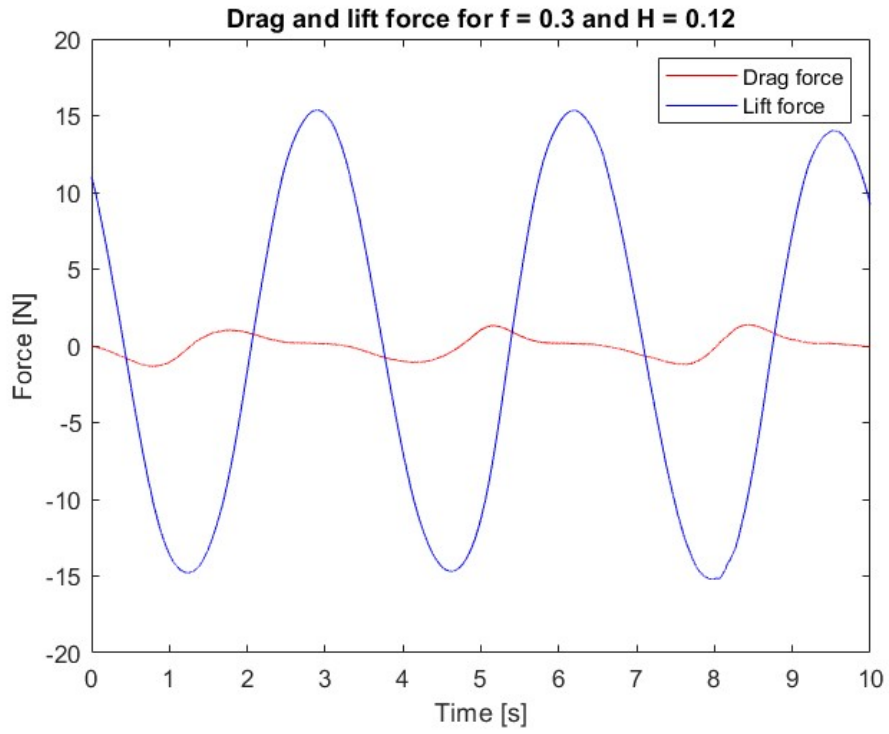
Figure 55: Experimental drag and lift force for case 4
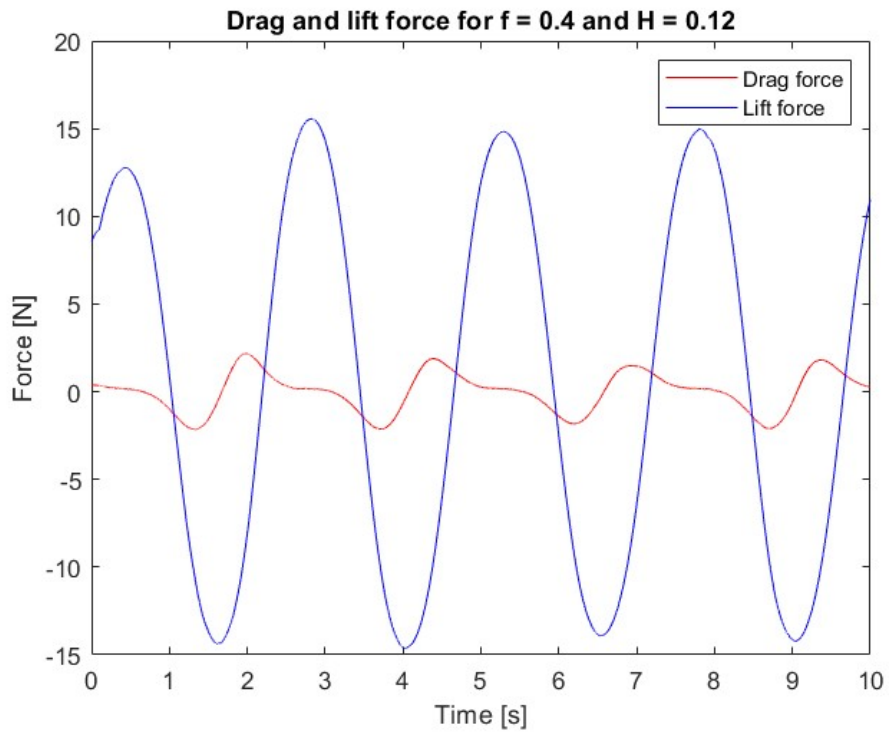
Figure 56: Experimental drag and lift force for case 5
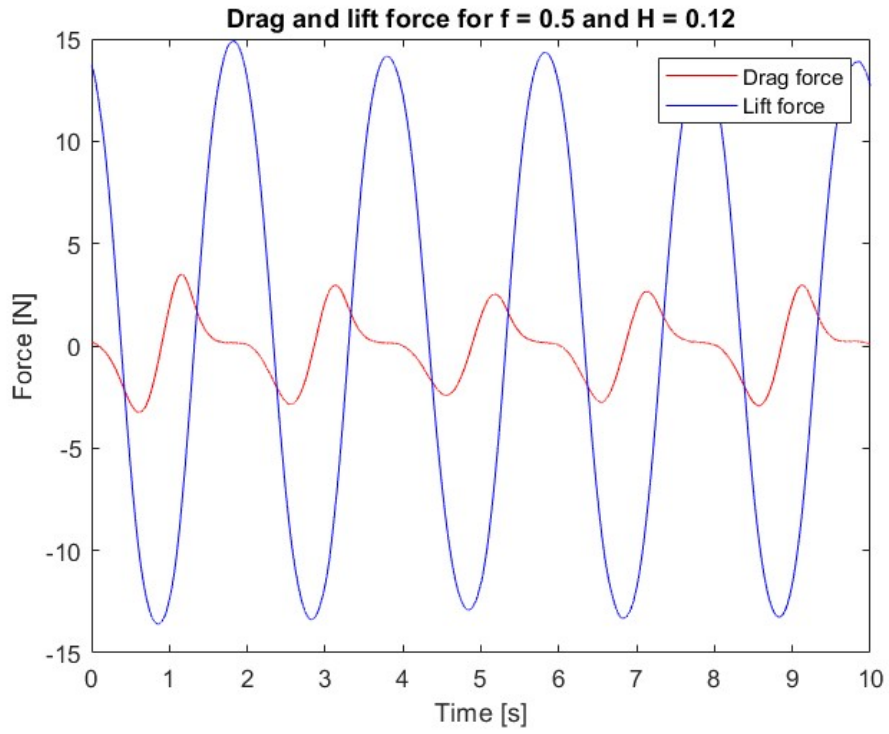
Figure 57: Experimental drag and lift force for case 6
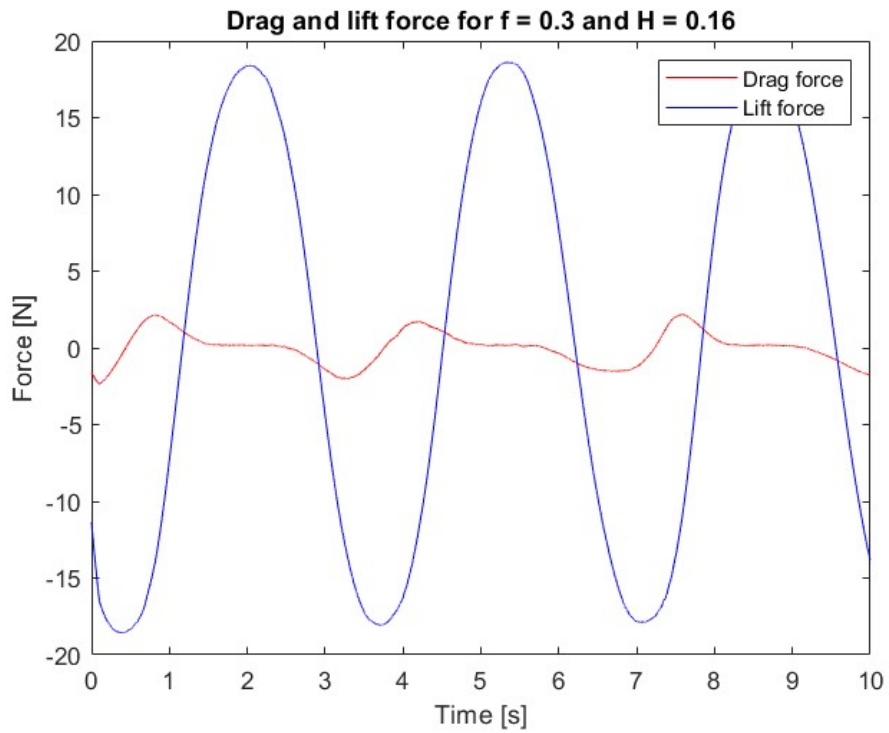
Figure 58: Experimental drag and lift force for case 7

71
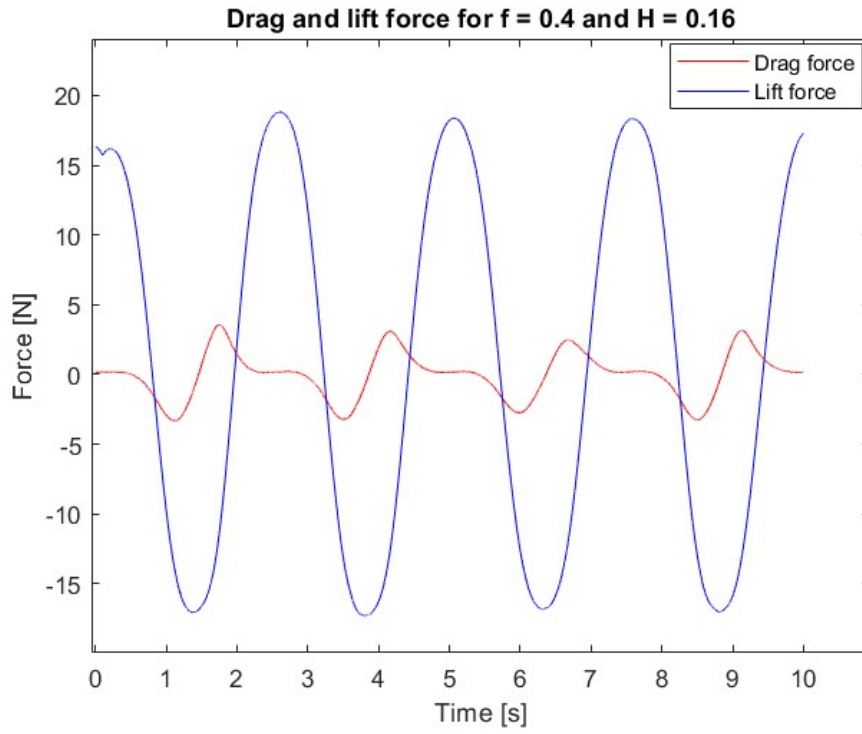
Figure 59: Experimental drag and lift force for case 8

Figure 60: Experimental drag and lift force for case 9

As the figures shows, the drag and lift forces follows the same pattern. The lift force oscillates harmonically around zero, while the drag force have a plateau when the lift force is at its maximum. This could be due to the momentary lack of motion as the waves changes from an ascending to a descending motion.

6.3 Comparing numerical and experimental data

After extracting the data from the simulations and the experimental tests, the data can be compared to analyze the accuracy of the numerical method. To better show the differences, the drag and lift force will be shown separately, and the simulated data will be shifted to the experimental data to get overlapping peaks and bottoms. The drag force comparisons are shown in Figure 61 to Figure 69.
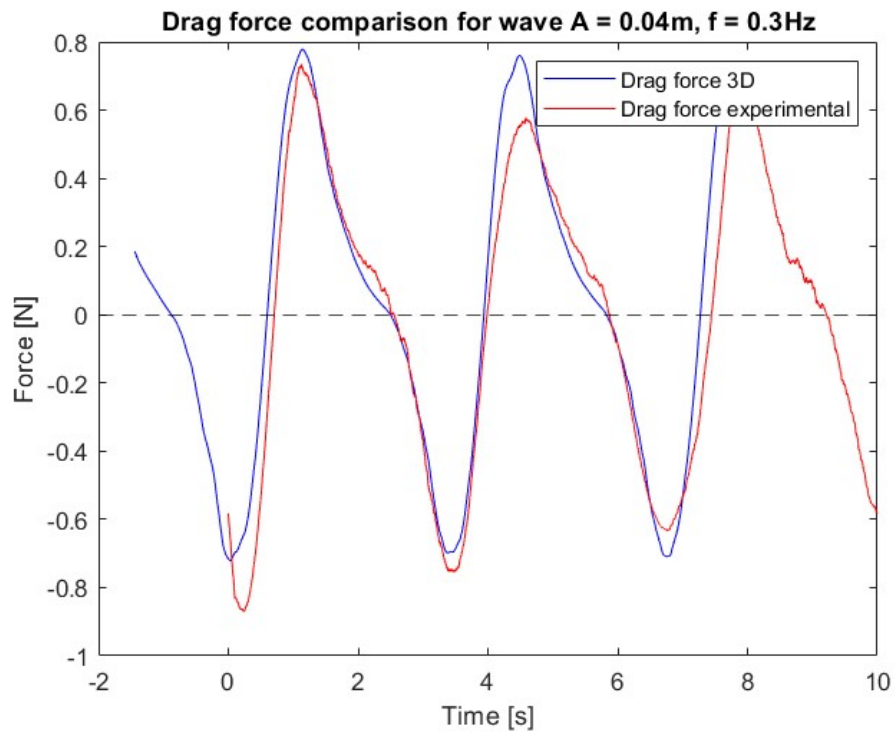
Figure 61: Simulated and experimentally recorded drag force data for case 1
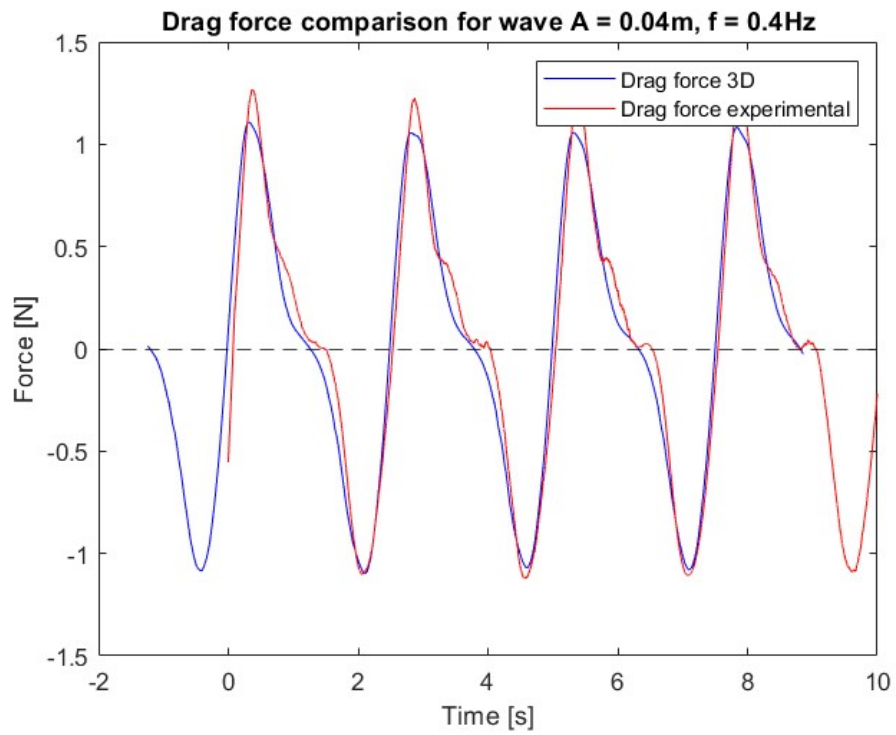
Figure 62: Simulated and experimentally recorded drag force data for case 2
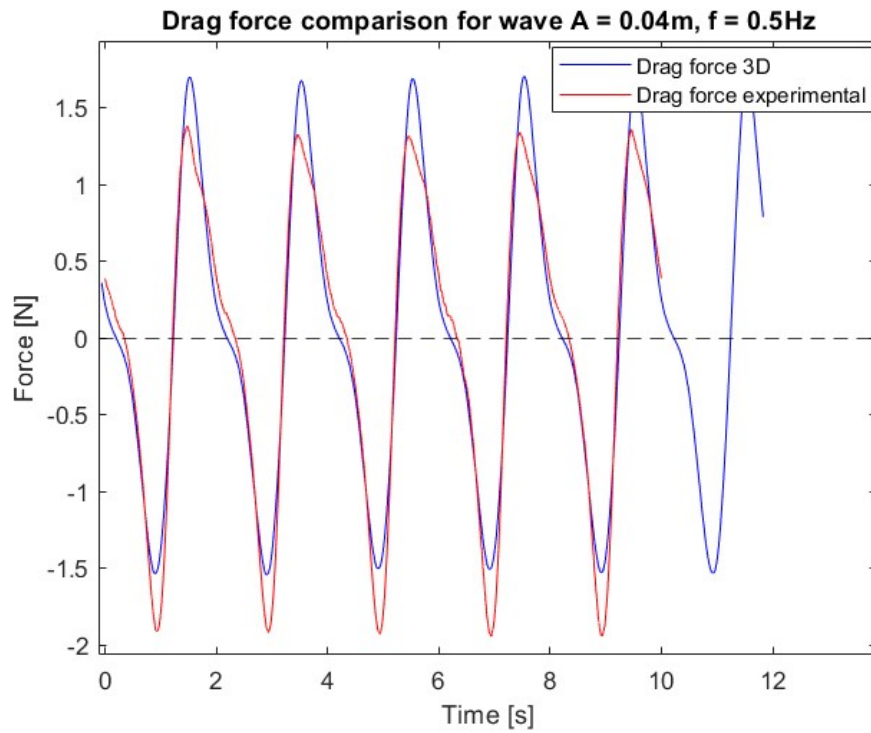
Figure 63: Simulated and experimentally recorded drag force data for case 3
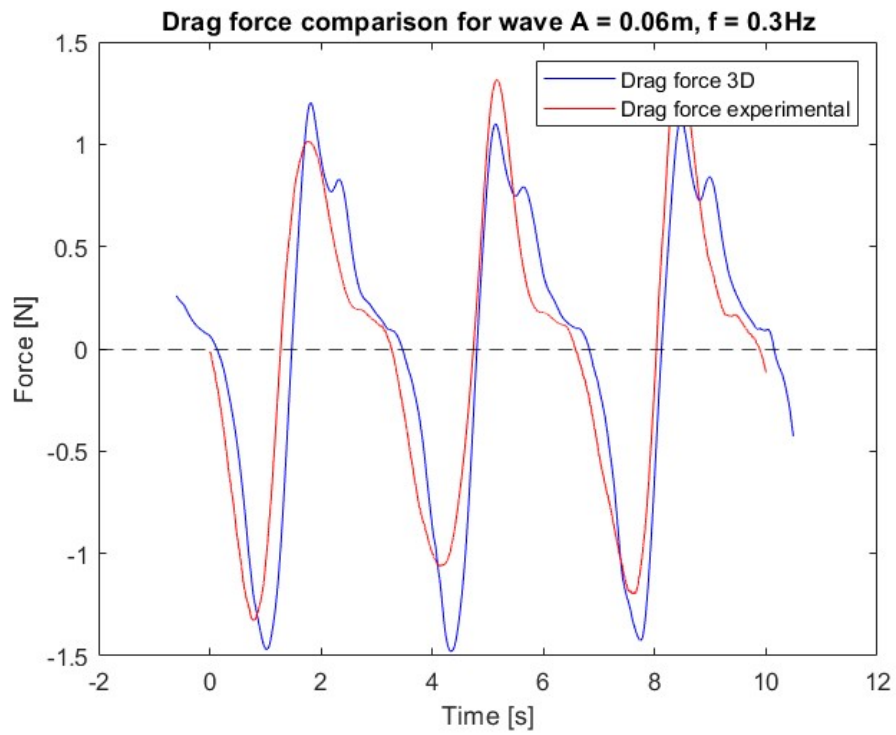
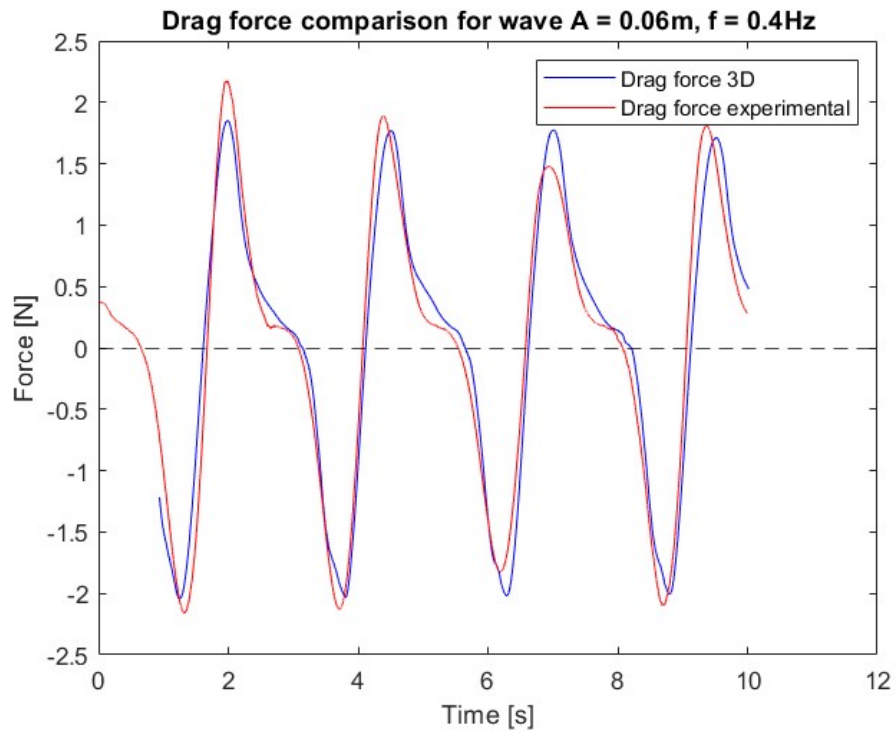Figure 64: Simulated and experimentally recorded drag force data for case 4

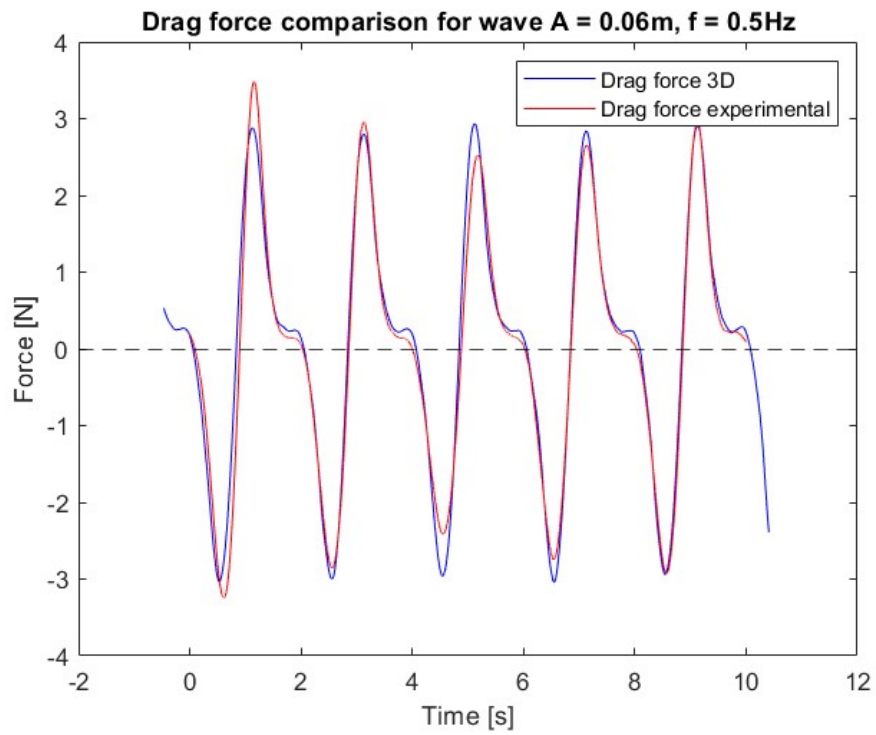Figure 65: Simulated and experimentally recorded drag force data for case 5

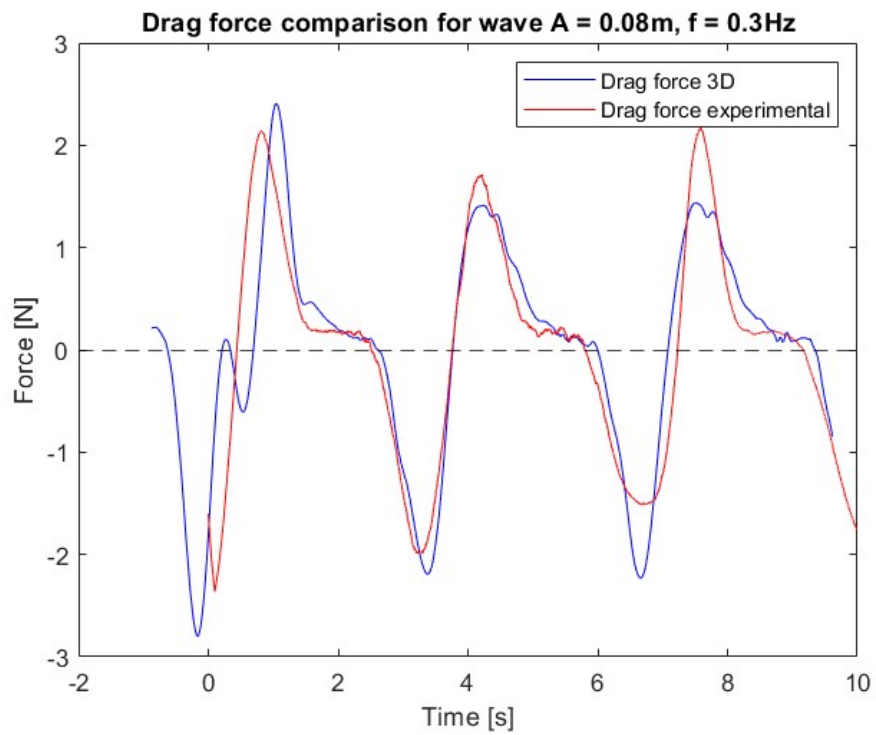Figure 66: Simulated and experimentally recorded drag force data for case 6

Figure 67: Simulated and experimentally recorded drag force data for case 7
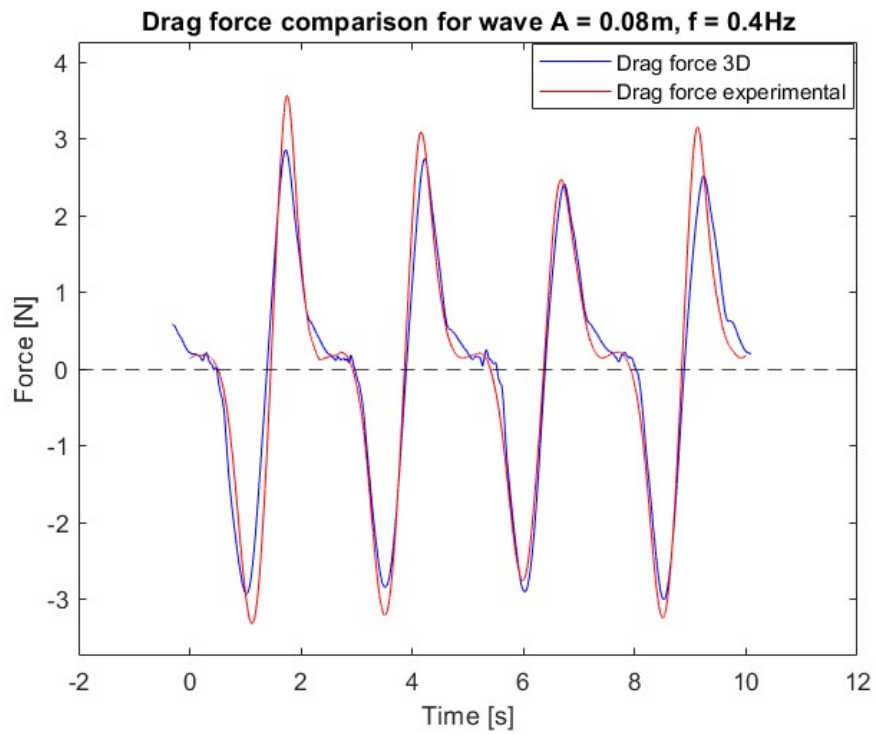
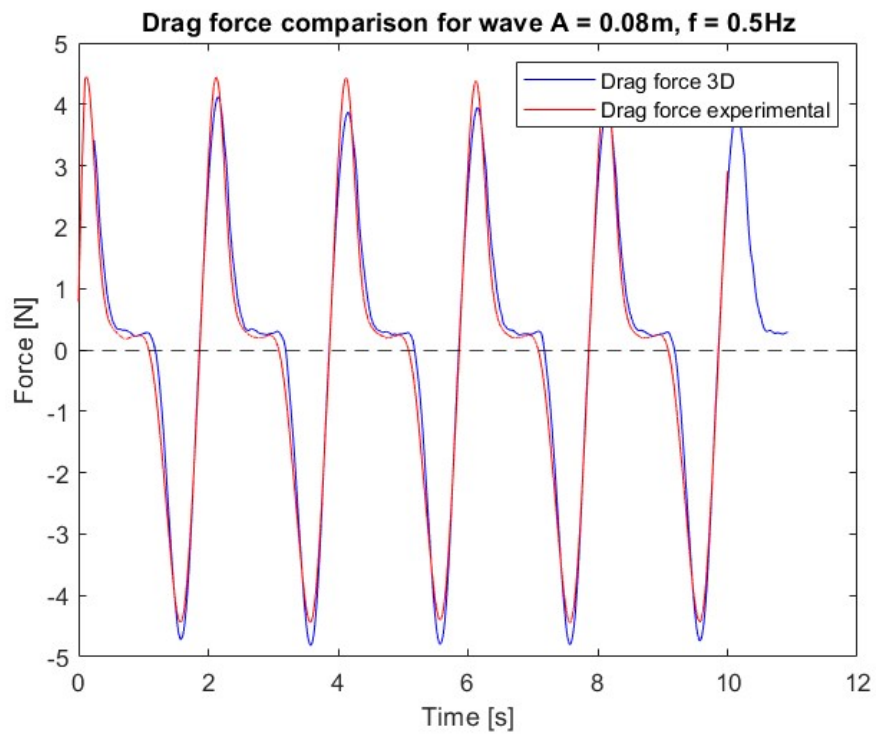Figure 68: Simulated and experimentally recorded drag force data for case 8

Figure 69: Simulated and experimentally recorded drag force data for case 9

Further, the lift force comparison plots are shown in Figure 70 to Figure .
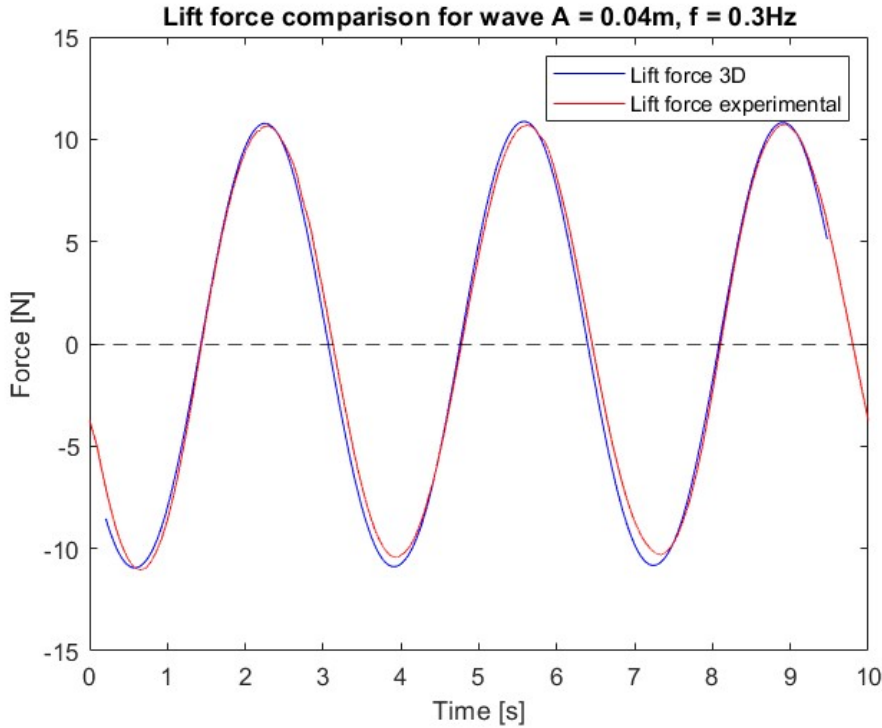

Figure 70: Simulated and experimentally recorded lift force data for case 1

Figure 71: Simulated and experimentally recorded lift force data for case 2

Figure 72: Simulated and experimentally recorded lift force data for case 3

Figure 73: Simulated and experimentally recorded lift force data for case 4

Figure 74: Simulated and experimentally recorded lift force data for case 5
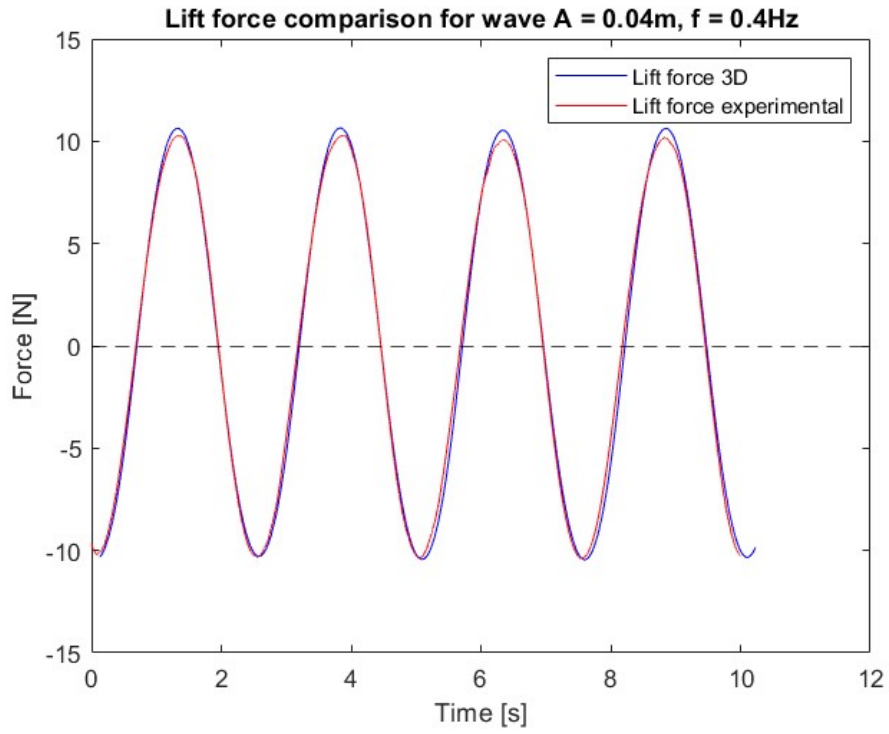
81

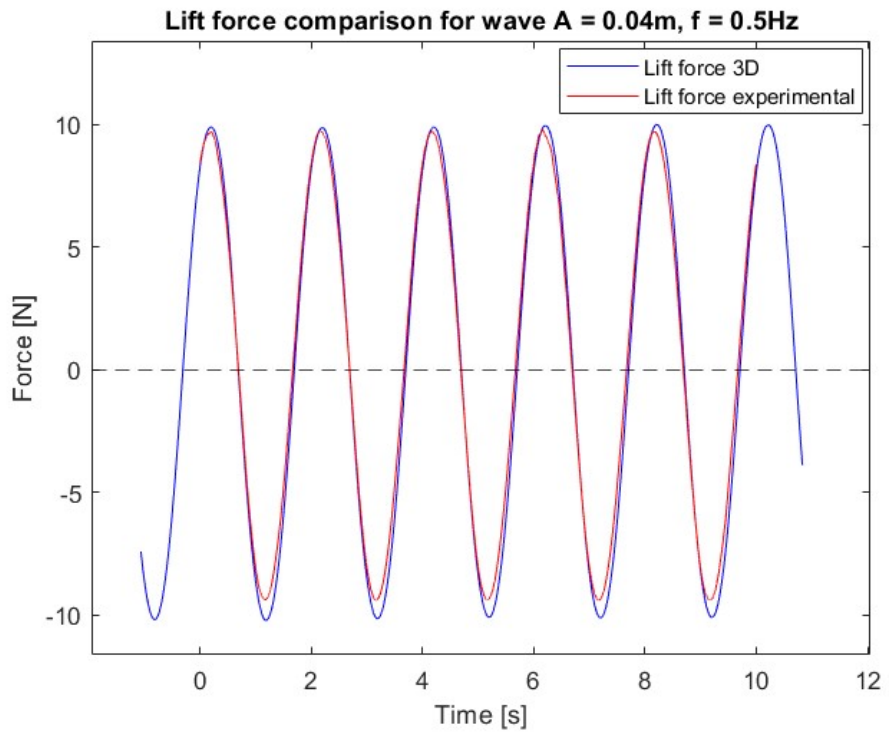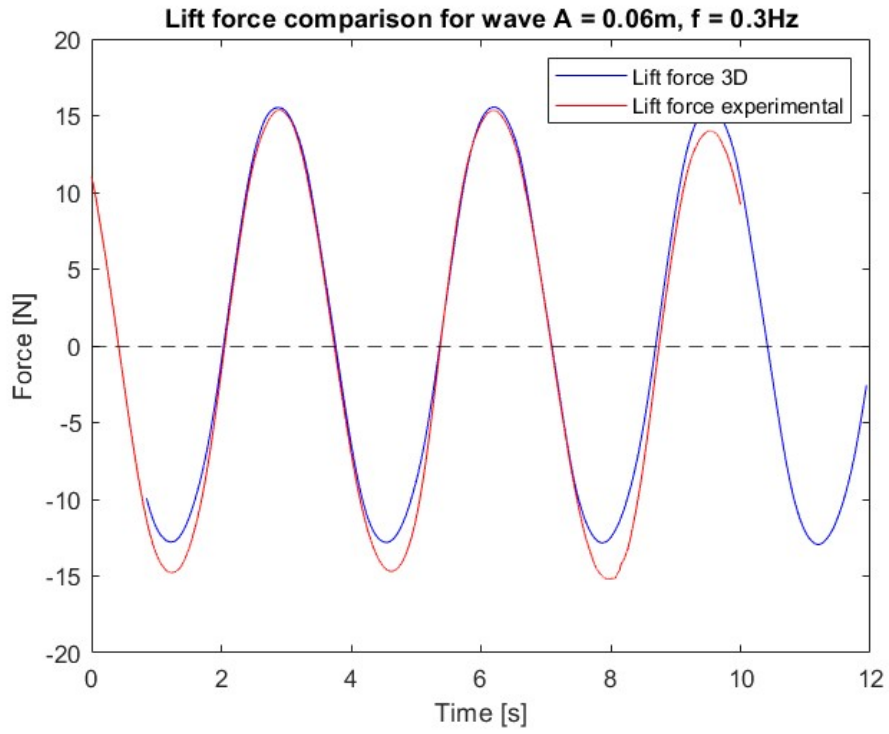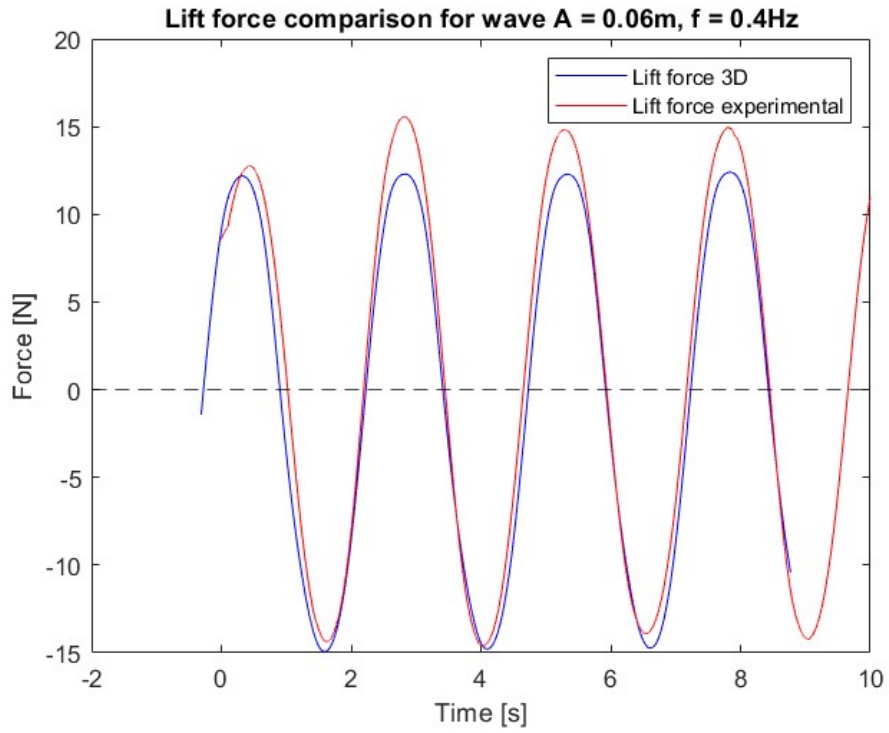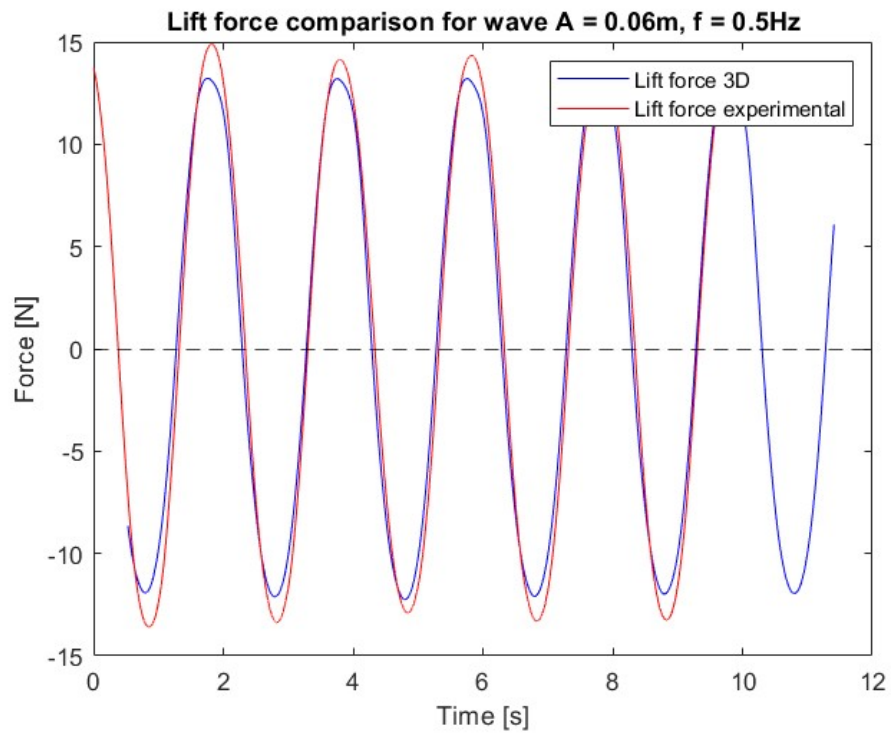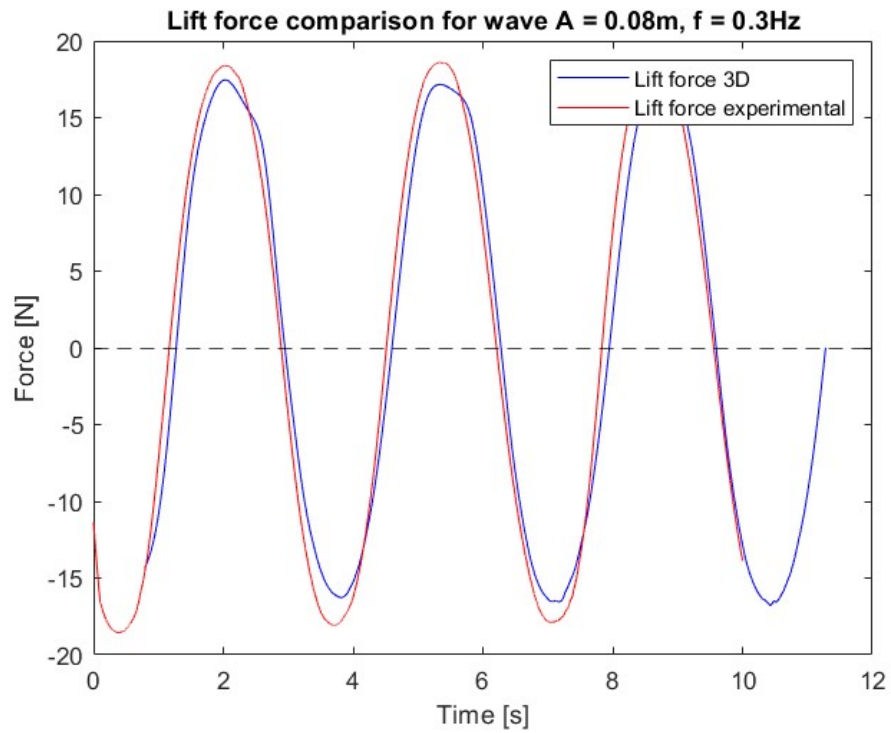Figure 75: Simulated and experimentally recorded lift force data for case 6

Figure 76: Simulated and experimentally recorded lift force data for case 7
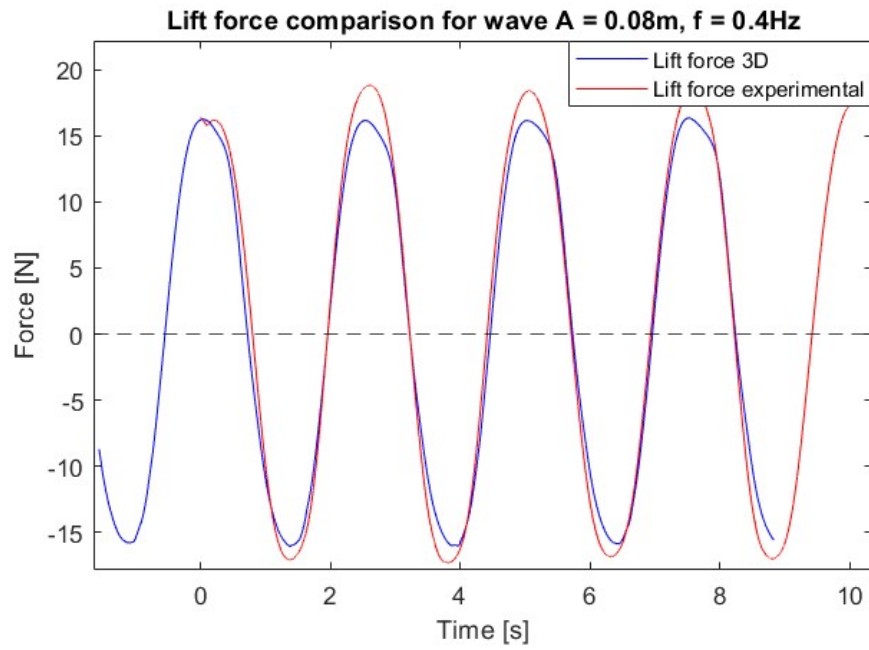
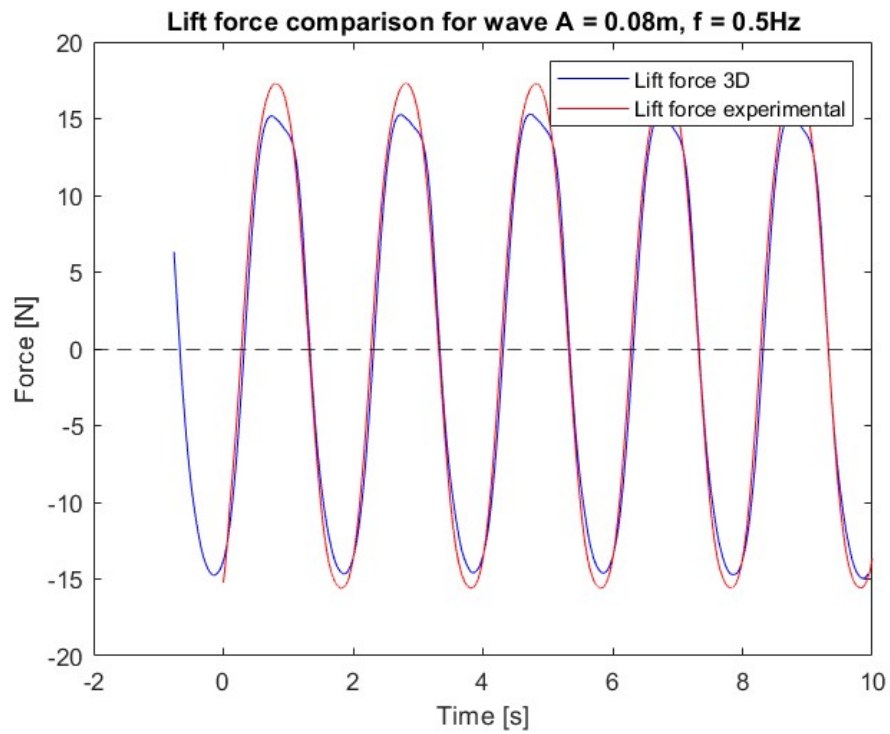Figure 77: Simulated and experimentally recorded lift force data for case 8

Figure 78: Simulated and experimentally recorded lift force data for case 9

The average of maximum and minimum drag force from 3D and experimental tests are shown

for each case in Table 29. The maximum forces are calculated by reading the force values of every crest and trough for 3D and experimental data for each case and taking the average force value of said wave crests and troughs.

Table 29: Maximum drag force for each case

Case	3D simulation [max/min]	Experimental results [max/min]
1	0.8 N/-0.7 N	0.7 N/-0.7
2	1.1 N/-1.1 N	1.0 N/-1.1 N
3	1.7 N/-1.6 N	1.5 N/-1.5 N
4	1.2 N/-1.3 N	1.2 N/-1.2 N
5	1.9 N/-1.9 N	1.9 N/-2.1 N
6	3.0 N/-3.0 N	3.0 N/-2.8 N
7	1.9 N/-1.7 N	2.0 N/-1.8 N
8	3.0 N/-3.0 N	3.1 N/-3.1 N
9	4.1 N/-4.6 N	4.6 N/-4.3 N

The figures comparing the drag forces and the maximum output forces table shows that the 3D simulations yields accurate predictions of the drag force on the sphere, when compared to the experimental data.

The maximum and minimum lift force from 3D simulations and experimental tests are shown for each case in Table 30. As with the drag force, the lift force values are calculated by taking the average value of the crest and troughs of the forces.

Table 30: Maximum lift force for each case

Case	3D simulation [max/min]	Experimental results [max/min]
1	10.8 N/-10.9 N	10.7 N/-10.4 N
2	10.5 N/-10.6 N	10.2 N/-10.2 N
3	10.2 N/-9.8 N	10.0 N/-9.6 N
4	14.7 N/-13.8 N	14.9 N/-14.9 N
5	13.3 N/-13.9 N	14.6 N/-14.3 N
6	12.9 N/-12.4 N	14.2 N/-13.3 N
7	18.5 N/-15.0 N	18.5 N/-18.0 N
8	16.8 N/-15.5 N	18.5 N/-17.0 N
9	15.0 N/-15.1 N	17.1 N/-15.9 N

For the first 4 cases, the numerically calculated lift forces are very close to the recorded experimental lift forces. For the later cases, the 3D simulations seem to slightly underestimate the lift forces, with the difference increasing with higher frequencies. A larger wave height also seem to correspond with a larger underestimation of the lift forces.

The data also shows that an increase in wave amplitude corresponds to an increase in both drag and lift force, when frequency is kept constant. As a larger wave height means that more mass is swept across the sphere per wave, an increase in forces are expected. For increasing frequencies, with a constant wave height, the data shows that the drag force is increasing with increasing frequency, while the lift force decreases. This is the case for all wave heights. As a sample of 3 waves is not significant to show a trend, four more cases are simulated for this analysis. Two extra frequencies, f = 0.6 Hz and f = 0.7 Hz at a wave height of 0.12 m are added, and two extra wave heights of 0.20 m and 0.24 m are added with a frequency of 0.5 Hz. These cases are shown in Table 31.

Table 31: Extra 3D simulated wave cases for analyzing increasing frequencies and wave heights

Case	Frequency [Hz]	Wave height [m]	Maximum drag force [N]	Maximum lift force [N]
10	0.5	0.04	0.7	5.2
11	0.5	0.20	5.6	15.9
12	0.5	0.24	6.2	18.3
13	0.6	0.12	4.7	11.4
14	0.7	0.12	5.4	10.1

To further investigate these relations, constant frequency and constant wave height plots are shown in Figure 79 for drag force at constant frequency, Figure 80 for lift force at constant frequency, Figure 81 for drag force at constant wave height and Figure 82 for lift force at constant wave height.
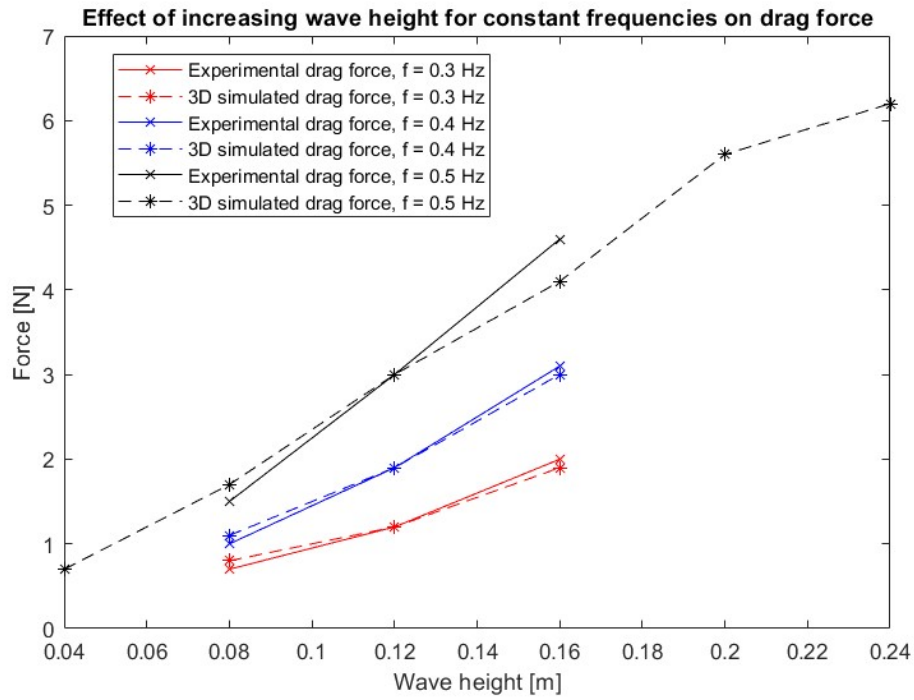
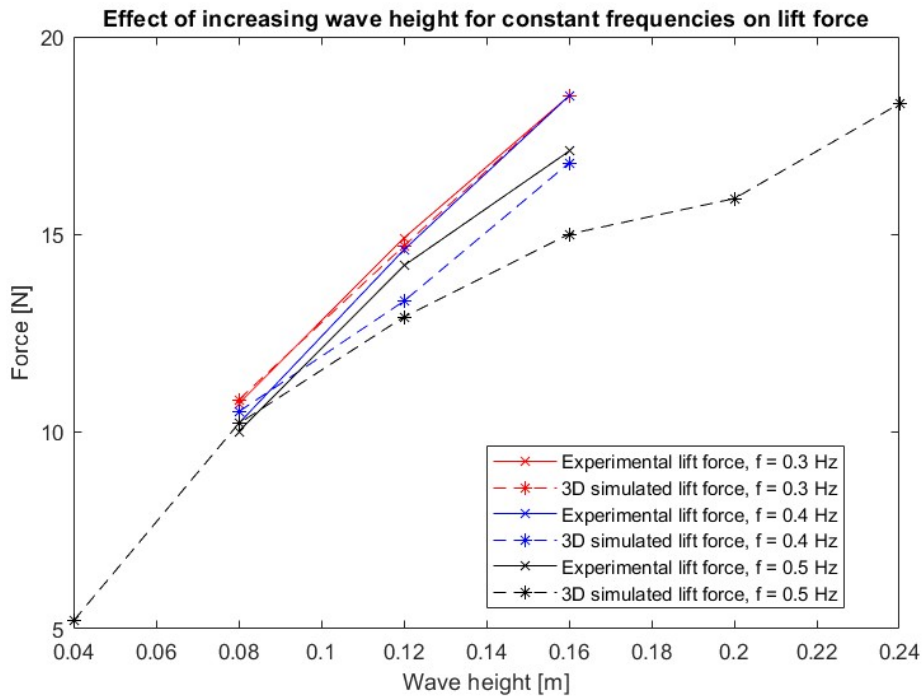Figure 79: Increasing wave height and constant frequency for drag forces

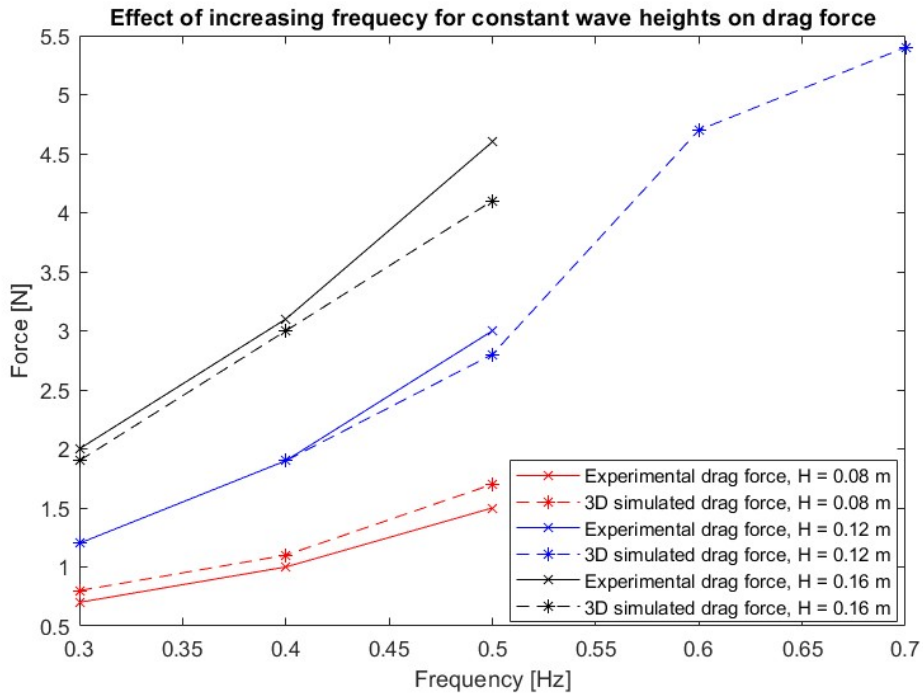Figure 80: Increasing wave height and constant frequency for lift forces

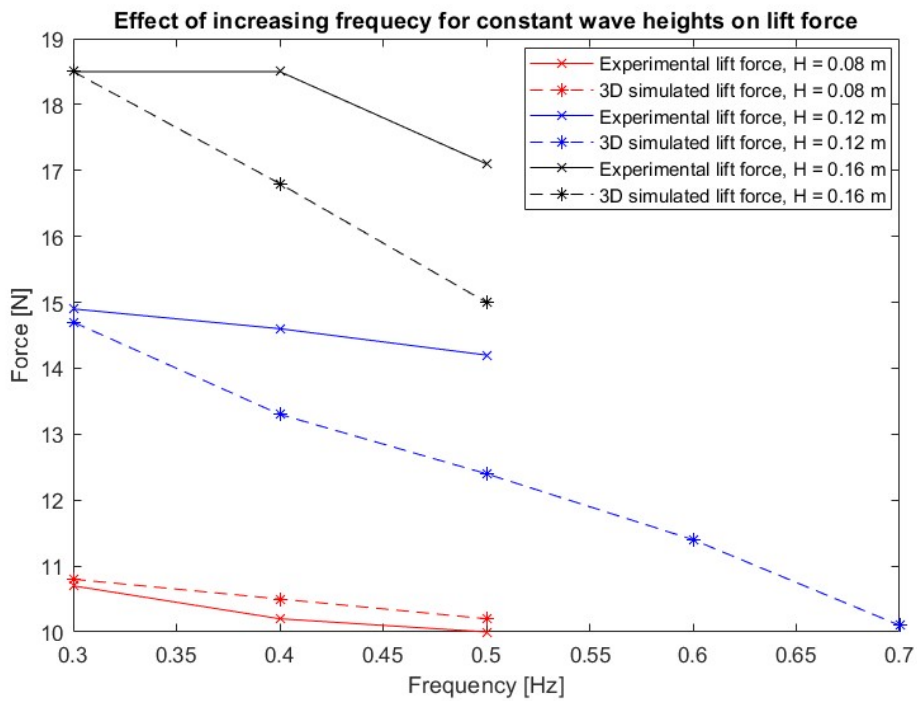Figure 81: Increasing frequency and constant wave height for drag forces

Figure 82: Increasing frequency and constant wave height for lift forces

From these charts, the observed trends seem to continue. Increasing the wave height seems

to increase both the drag and lift forces, while increasing the frequency seems to lead to an increase in drag forces and a decrease in lift force, also when adding two more cases for constant frequency and 2 more cases for constant wave height. From this sample size, it is not possible to determine whether this relation is linear, exponential or follows another pattern. To be able to determine a trend, more wave cases would need to be tested.

From these charts it is also evident that when looking at increasing wave heights, the simulated and experimentally recorded drag force seems to stay close to each other for f = 0.3 Hz and f = 0.4 Hz, while a small difference is seen at f = 0.5 Hz. For lift force, the data shows that the experimental and numerical data differ a bit more with increasing wave height, for the two lower frequencies, while for f = 0.5, the difference is larger, about 2 N.

When looking at increasing frequencies, the drag force chart shows that an increase in frequency yields a larger distance between the numerical and experimental data. This effect is larger with increasing wave heights. As for the lift force, the same trend is observed, but the difference in forces deviates at an earlier wave height, and the larger division between numerical and experimental data starts at f = 0.4 Hz, for H = 0.12 m and H = 0.16 m. For H = 0.08 m, the data seems to follow each other closely for all frequencies.

6.4 Energy calculations

This subsection will cover the available energy in the different wave cases, the energy related to the simulated loads, and the energy related to the experimentally measured loads.

6.4.1 Theoretically calculated available energy in the waves

The available energy in the waves are calculated using the total energy formulation given in Equation 25. The variables in the equation are density ρ, which is assumed to be constant at $997 \ kg/m^3$, the gravitational acceleration g, assumed to be $9.81 \ m/s^2$, the wave amplitude ζ_A, which varies between cases and the wavelength λ, which also varies from case to case. The calculations are presented in Table 32.

Table 32: Available wave energy for the different cases

Case	Wave amplitude [m]	Wavelength [m]	Energy [J]
1	0.04	14.01	7.82
2	0.04	9.15	7.82
3	0.04	6.17	7.82
4	0.06	14.01	17.6
5	0.06	9.15	17.6
6	0.06	6.17	17.6
7	0.08	14.01	31.2
8	0.08	9.15	31.2
9	0.08	6.17	31.2

6.4.2 Energy from numerical data

To analyse the energy potential from the numerical data the integral of the volume fraction at the sphere is extracted from the simulations, as well as the drag and lift coefficients, in addition to the drag and lift forces. Using these parameters, the flow velocity as a function of time can be calculated using Equation 18. Further, this can be input into Equation 27, along with the force values for one wave, to calculate the energy.

6.4.3 Energy from experimental data

6.4.4 Comparing theoretical energy calculations with numerical and experimental energy calculations

7   Conclusion

This research has investigated the wave energy converter potential for a spherical object.

7.1   Further work

For further work, there are a few parameters that would be interesting to see researched further. Replacing the regular waves with an irregular sea state like a JONSWAP or Pierson Moskowitz spectrum in simulations and in MarinLab on the same shaped structure, could drive this research further. This would contribute to refine the research to a more realistic scenario. One could also repeat this type of research for other shaped objects, as this would contribute to optimize wave energy converter designs when moving towards a prototype study.

On the experimental front, there are a few possibilities for further work as well. As discussed in subsection 5.7, the load cell setup has a coupling effect when set up as in this thesis. A study of different load cell setups, and optimizing the entire experimental setup would make the laboratory testing more reliable, strengthening further development. Jacob Andersen and Morten Bech Kramer [25] have conducted a research into different setups, where a system of six pretensioned wires with one degree of freedom force transducers was found to be the most accurate for a fixed sphere, more than a six degree of freedom load cell setup mounted at the top of the sphere.

Another proposition for a research project is investigating different mooring options. This study could be done numerically using computed hydrodynamics software, i.e. SESAM from DNV, and/or experimentally in MarinLab or in a similar hydrodynamic test facility.

References

[1] Global energy review: Co2 emissions in 2021. Technical report, IEA paris, 2022.

[2] T-Z. Ang, M. Salem, M. Kamarol, H.S. Das, M.A. Nazari, and N. Prabaharan. A comprehensive study of renewable energy sources: Classifications, challenges and suggestions. *Energy Strategy Reviews*, 43:100939, 2022.

[3] B. Drew, A.R. Plummer, and M.N. Sahinkaya. A review of wave energy converter technology. *Proceedings of the Institution of Mechanical Engineers, Part A: Journal of Power and Energy*, 223(8):887–902, 2009.

[4] A.B.S. Bahaj. Generating electricity from the oceans. *Renewable and Sustainable Energy Reviews*, 2011.

[5] A. Clément, P. McCullen, A. Falcão, A. Fiorentino, F. Gardner, K. Hammarlund, G. Lemonis, T. Lewis, K. Nielsen, S. Petroncini, M-T. Pontes, P. Schild, B-O. Sjöström, H.C. Sørensen, and T. Thorpe. Wave energy in europe: current status and perspectives. *Renewable and Sustainable Energy Reviews*, 6(5):405–431, 2002.

[6] T.W. Thorpe et al. A brief review of wave energy. 1999.

[7] R. Pelc and R.M. Fujita. Renewable energy from the ocean. *Marine Policy*, 26(6):471–479, 2002.

[8] S. Foteinis. Wave energy converters in low energy seas: Current state and opportunities. *Renewable and Sustainable Energy Reviews*, 162:112448, 2022.

[9] D.C. Wilcox. *Turbulence Modelling for CFD, Third Edition*. DCW Industries, Inc., 2006.

[10] F.R. Menter. Zonal two equation k-ω turbulence models for aerodynamic flows. *AIAA Paper 93-2906*, 1993.

[11] J.E. Welch, F.H. Harlow, J.P. Shannon, and B.J. Daly. The mac method-a computing technique for solving viscous, incompressible, transient fluid-flow problems involving free surfaces.

[12] C.W. Hirt and B.D. Nichols. Volume of fluid (vof) method for the dynamics of free boundaries. *Journal of Computational Physics*, 39(1):201–225, 1981.

[13] ©ANSYS, Inc. *ANSYS User Manual Release 12.0*, 2009.

[14] Shyam2791 - own work.
https://commons.wikimedia.org/w/index.php?curid=22702507.

[15] J. Králik. Cfd simulation of air flow over an object with gable roof, revised with y+ approach. 2016.

[16] G. Russo L. Pareschi. *Implicit–Explicit Runge–Kutta schemes for stiff systems of differential equations*, volume 3, pages 269–288. 01 2001.

[17] B. Pettersen. *Marin Teknikk 3 Hydrodynamikk*. Akademika, 2022.

[18] Department of Mechanical and Marine Engineering. Marinlab. Technical report, Høgskulen på Vestlandet.

[19] Applied Measurements Ltd. Load cells and force sensors, 2023.

[20] Michigan Scientific Corporation. What is a strain gauge?, 2023.

[21] E-design Ltd. Wave gauges, 2023.

[22] MathWorks. Matlab, 2023.

[23] *ITTC - Recommended procedures and guidelines 7.6-02-09*, 2002. Work instructions, Calibration of load cells.

[24] M. Paulsen. Videreutvikling av eksperimentell metode for måling av hydrodynamiske krefter på en foilseksjon, 2022.

[25] J. Andersen and M.B. Kramer. Wave excitation tests on a fixed sphere: Comparison of physical wave basin setups. In *Proceedings of the European Wave and Tidal Energy Conference*, volume 15, 2023.

Appendix

Appendix A: CAD drawings

Put your figures or text here...

Appendix B: MATLAB script

Put your figures or text here...

Appendix C: Calibration data points